



MOSAIC: A Satellite Constellation to Enable Groundbreaking Mars Climate System Science and Prepare for Human Exploration

Robert J. Lillis¹ , David Mitchell¹ , Luca Montabone² , Nicholas Heavens² , Tanya Harrison³, Cassie Stuurman⁴, Scott Guzewich⁵ , Scott England⁶ , Paul Withers⁷ , Mike Chaffin⁸ , Shannon Curry¹ , Chi Ao⁴ , Steven Matousek⁴ , Nathan Barba⁴, Ryan Woolley⁴ , Isaac Smith⁹ , Gordon R. Osinski¹⁰ , Armin Kleinböhl⁴, Leslie Tamppari⁴ , Michael Mischna⁴ , David Kass⁴ , Michael Smith⁵, Michael Wolff² , Melinda Kahre¹¹, Aymeric Spiga¹² , François Forget¹² , Bruce Cantor¹³, Justin Deighan⁸ , Amanda Brecht¹¹ , Stephen Bougher¹⁴ , Christopher M. Fowler¹ , David Andrews¹⁵ , Martin Patzold¹⁶, Kerstin Peter¹⁶ , Silvia Tellmann¹⁶, Mark Lester¹⁷ , Beatriz Sánchez-Cano¹⁷ , Janet Luhmann¹ , François Leblanc¹⁸ , Jasper Halekas¹⁹ , David Brain⁸ , Xiaohua Fang⁸ , Jared Espley⁵ , Hermann Opgenoorth²⁰ , Oleg Vaisberg²¹ , David Hinson²² , Sami Asmar⁴ , Joshua Vander Hook⁴ , Ozgur Karatekin²³ , Aroh Barjatya²⁴ , and Abhishek Tripathi¹

¹ Space Sciences Laboratory, University of California, Berkeley, CA 94720, USA; rlillis@berkeley.edu

² Space Sciences Institute, Boulder, CO 80301, USA

³ Planet Federal Inc., Washington DC 20005, USA

⁴ Jet Propulsion Laboratory, California Institute of Technology, Pasadena, CA 91109, USA

⁵ NASA Goddard Space Flight Ctr., Greenbelt, MD 20771, USA

⁶ Virginia Tech University, Blacksburg, VA 24061, USA

⁷ Boston University, Boston, MA 02215, USA

⁸ Laboratory for Atmospheric and Space Physics, University of Colorado, Boulder, CO 80301, USA

⁹ York University, Toronto, Ontario M3J 1P3, Canada

¹⁰ University of Western Ontario, London, ON N6A 5B7, Canada

¹¹ NASA Ames Research Ctr., Mountain View, CA 94035, USA

¹² Laboratoire de Météorologie Dynamique, IPSL, Paris, France

¹³ Malin Space Science Systems, San Diego, CA 92121, USA

¹⁴ University of Michigan, Ann Arbor, MI 48109, USA

¹⁵ Swedish Institute of Space Physics, Uppsala, Sweden

¹⁶ Rheinisches Institut für Umweltforschung, Abt. Planetenforschung, Cologne, Germany

¹⁷ School of Physics and Astronomy, University of Leicester, UK

¹⁸ Laboratoire Atmosphères, Observations Spatiales, IPSL, Paris, France

¹⁹ University of Iowa, Iowa City, IA 52242, USA

²⁰ University of Umea, Sweden

²¹ Space Research Institute, Moscow, Russia

²² SETI Institute, Mountain View, CA 94043, USA

²³ Royal Belgian Observatory, Uccle, Belgium

²⁴ Embry Riddle Aeronautical University, Daytona Beach, FL 32114, USA

Received 2021 February 2; revised 2021 May 5; accepted 2021 May 5; published 2021 October 12

Abstract

The Martian climate system has been revealed to rival the complexity of Earth's. Over the last 20 yr, a fragmented and incomplete picture has emerged of its structure and variability; we remain largely ignorant of many of the physical processes driving matter and energy flow between and within Mars' diverse climate domains. Mars Orbiters for Surface, Atmosphere, and Ionosphere Connections (MOSAIC) is a constellation of ten platforms focused on understanding these climate connections, with orbits and instruments tailored to observe the Martian climate system from three complementary perspectives. First, low-circular near-polar Sun-synchronous orbits (a large mothership and three smallsats spaced in local time) enable vertical profiling of wind, aerosols, water, and temperature, as well as mapping of surface and subsurface ice. Second, elliptical orbits sampling all of Mars' plasma regions enable multipoint measurements necessary to understand mass/energy transport and ion-driven escape, also enabling, with the polar orbiters, dense radio occultation coverage. Last, longitudinally spaced areostationary orbits enable synoptic views of the lower atmosphere necessary to understand global and mesoscale dynamics, global views of the hydrogen and oxygen exospheres, and upstream measurements of space weather conditions. MOSAIC will characterize climate system variability diurnally and seasonally, on meso-, regional, and global scales, targeting the shallow subsurface all the way out to the solar wind, making many first-of-their-kind measurements. Importantly, these measurements will also prepare for human exploration and habitation of Mars by providing water resource prospecting, operational forecasting of dust and radiation hazards, and ionospheric communication/positioning disruptions.



Original content from this work may be used under the terms of the [Creative Commons Attribution 4.0 licence](https://creativecommons.org/licenses/by/4.0/). Any further distribution of this work must maintain attribution to the author(s) and the title of the work, journal citation and DOI.

Unified Astronomy Thesaurus concepts: Mars (1007); Planetary atmospheres (1244); Surface ices (2117); Planetary ionospheres (2185); Planetary magnetospheres (997); Thermosphere (1694); Upper atmosphere (1748); Space weather (2037); Planetary climates (2184); Space vehicle instruments (1548); Space plasmas (1544); Mesosphere (1030)

1. Background and Motivation

1.1. The MOSAIC Concept Study

This article is based in large part on the MOSAIC Planetary Mission Concept Study, funded by NASA headquarters to provide input to the Planetary Science and Astrobiology Decadal Survey 2023–2032. This study was carried out from 2019 October until 2020 August by a team of more than 100 scientists and engineers from 23 institutions. It consisted of three overlapping phases. First, a multidisciplinary team of 47 scientists (PI: Rob Lillis, UC Berkeley) was arranged into seven working groups and a steering committee. Over several months, we formulated the Goals, Objectives, and Investigations comprising the high-level MOSAIC concept, before defining (a) detailed measurement requirements and (b) scientific instrumentation designed to make the required measurements from a variety of orbital perspectives.

Second, a Study Team (Study Lead: Steve Matousek) at the NASA Jet Propulsion Lab (JPL) worked closely with the Science Team to (a) define architectural “building blocks” with which to construct possible mission concepts, (b) explore the technical and scientific trade space encompassing the boundaries of such concepts, and (c) work with the rapid-iteration design groups known as Team-X and Team-Xc (for small satellites) to formulate specific point designs that met the MOSAIC science requirements while achieving technical closure. These designs were subject to cost and schedule analysis.

Third, a 437-page report (Lillis et al. 2020) was drafted, consisting of the scientific and human exploration motivation for MOSAIC, the high-level mission concept, a technical overview, and discussion of schedule constraints and mission lifecycle costs, in addition to several detailed appendices. This report was submitted to NASA and the National Academies of Science, Engineering, and Medicine on 2020 August 7.

The remainder of Section 1 provides the background and motivation underpinning the MOSAIC concept, both scientific and relating to preparing for human exploration. Section 2 describes MOSAIC’s science traceability from Goals to Objectives to Investigations and Measurements. Section 3 describes the MOSAIC Mission Concept, i.e., the spacecraft and mission design architecture necessary to complete the investigations. Section 4 briefly describes the Investigations with tables for their measurement requirements. Section 5 describes practical aspects of MOSAIC and possible paths forward for the concept, including its inherent flexibility and modularity, possible contributions from international and/or commercial partners, management structure suggestions, possible descopes, and cost projections under different costing assumptions. Section 6 provides summary, acknowledgments, and conclusions. Following this are appendices covering the following topics: science team structure and process, detailed descriptions of the measurement requirements and instruments needed to make the measurements, plus summaries of the instrument and measurement requirements, and the cover of the technical report submitted to NASA HQ.

1.2. Martian Climate: From the Ancient Past to Our Near-future

Long considered an inspiring or baleful presence in the Earth’s night sky, Mars’ geological record preserves something that mostly has been obliterated from Earth and Venus: the story of the first billion years on a rocky planet with an atmosphere. It is the story of transition from a molten ball to a solid surface, reshaped by water and winds as much as lava. It is the story of a planet at least episodically warm and damp enough to have been able to support life on its surface. And it is a story we want to read in person. The 2018 NASA Strategic Plan (NASA 2018) calls out the Moon and Mars as the only specific destinations for deep space exploration by human beings.

Prior to sending humans, we need to do our due diligence to support in-person activities on Mars. The Strategic Plan also says that research and technology is necessary to “enable human missions to the surface of Mars.” Many strategic knowledge gaps have been identified that could endanger human missions to Mars (Beaty et al. 2012). Central among these are those related to the weather (particularly dust storms), the radiation environment, and the use of Mars’ water for human life support.

We have studied the Martian environment enough to know what we do not know, but not enough to understand its climate processes or keep astronauts safe in orbit or on its surface. The last two decades have seen a significant increase in the quantity and variety of observations characterizing the thermal structure and basic composition of the Martian atmosphere, from the surface to the exosphere. The incomplete picture that has emerged forms the basis for understanding the physical processes that control the current Martian climate, with information from the general circulation (Forget et al. 1999; Bougher et al. 2015), the role of clouds (Colaprete et al. 2003; Madeleine et al. 2012; Clancy et al. 2017) and photochemistry (Barabash et al. 2007; Gonzalez-Galindo et al. 2013; Chaffin et al. 2017), the development of dust storms (Cantor et al. 2001; Strausberg et al. 2005; Clancy et al. 2010; Elrod et al. 2020; Battalio & Wang 2021), and the channels and rates of atmospheric escape (Edberg et al. 2010; Clarke et al. 2014; Dong et al. 2015; Cravens et al. 2016; Curry et al. 2016; Dubinin et al. 2017; Lillis et al. 2017; Chaffin et al. 2018).

A qualitative diagram is shown in Figure 1 of our current understanding of the key physical processes that drive matter and energy flow within and between the various climate reservoirs. However, we are still largely ignorant of the relative magnitude of, or feedbacks between, these processes. To successfully unravel Mars’ present-day interacting climate processes and shed light on past processes, three major questions must be addressed. The following three subsections 1.3–1.5 cover these questions, the scientific background to them, and the necessary measurements to comprehensively address them. Section 1.6 explains how these same measurements address important strategic knowledge gaps that must be filled to enable the safe human exploration of Mars.

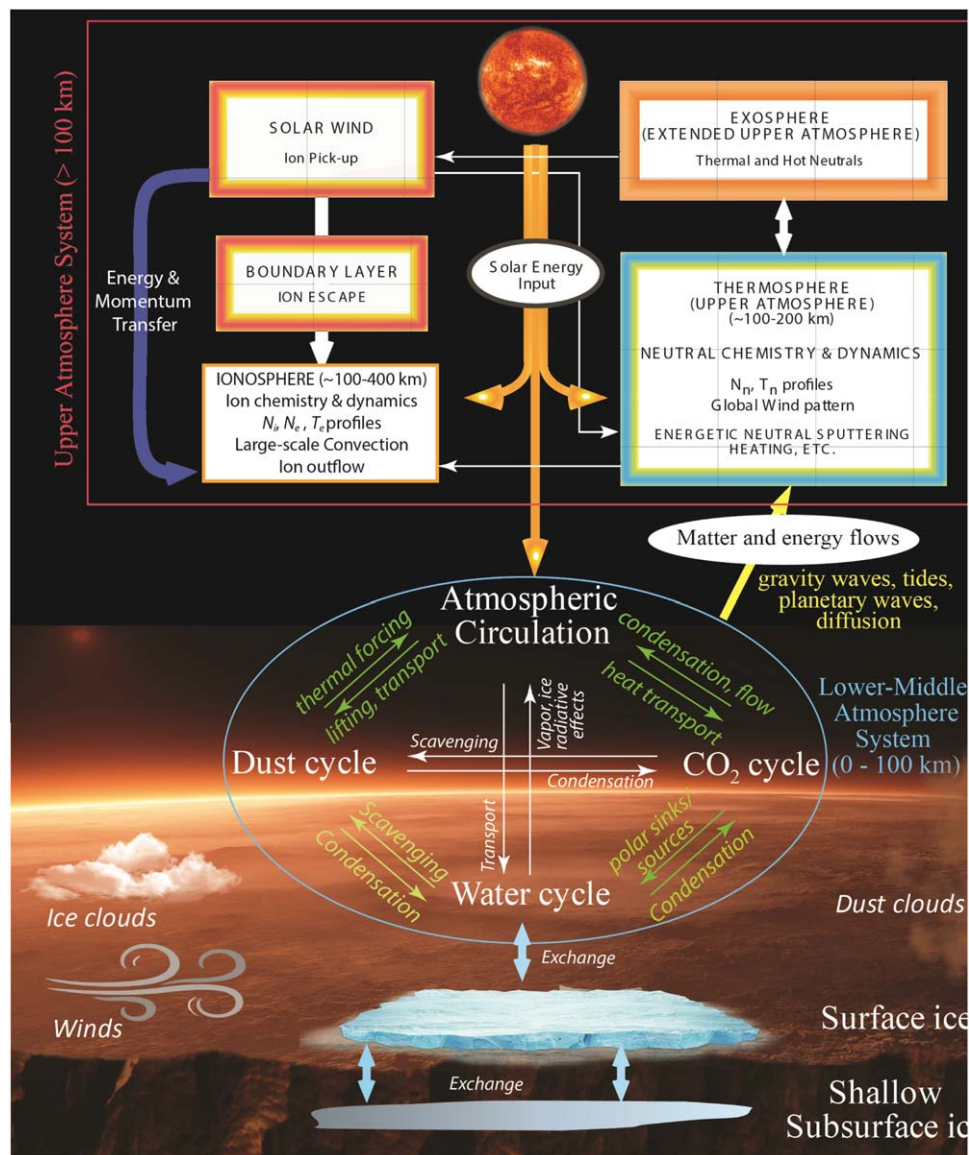


Figure 1. Schematic of some expected connections between the various Martian climate domains, which MOSAIC will systematically explore.

1.3. How Do Volatiles Move between the Subsurface, Surface, and Atmosphere?

Most water on Mars persists as surface and subsurface ice in the polar regions and mid-latitudes, concentrated at $\approx 35^\circ$ N/S (Mellon et al. 2004). The polar caps consist of a “residual” component made up of layered water ice (and in the southern residual cap, carbon dioxide ice) and dust that persists throughout the course of the Martian year, and a “seasonal” carbon dioxide and water ice frost component that freezes out of the atmosphere onto the surface in late fall and persists into spring (Benson & James 2005). The season-dependent temperature gradients between the ice-covered and ice-free ground along the cap edges result in significant weather activity, such as polar spiral storms and frontal storms (e.g., Malin et al. 2008; Wang & Fisher 2009). While the seasonal component of the northern polar cap is highly repeatable in its spatial distribution each year, reaching $\sim 50^\circ$ N at its maximum extent (e.g., Bass et al. 2000), the seasonal southern polar cap is much more variable (Jakosky &

Haberle 1990; Piqueux et al. 2015). Figure 2 shows examples of present-day water ice on Mars.

These changes have been meticulously tracked with the Mars Orbiter Camera aboard Mars Global Surveyor and the Mars Color Imager and Context Camera aboard Mars Reconnaissance Orbiter (Calvin et al. 2015), giving us over 10 Mars years of continuous records of the dynamism of the polar caps. However, the mechanisms driving the variability of the southern polar cap are poorly understood, and our knowledge of the relationship between surface and subsurface ice distribution across the planet is limited based on the current available data.

Subsurface ice has been observed and/or inferred based on several independent lines of evidence, including neutron spectrometry (Boynton et al. 2002; Feldman et al. 2007), ground-penetrating radar (GPR; Bramson et al. 2015; Stuurman et al. 2016), in situ observation (Rennó et al. 2009), and present-day excavation by impacts (Byrne et al. 2009; Dundas & Byrne 2010). Factors influencing the cryosphere depth include surface albedo, mean annual surface temperature, the

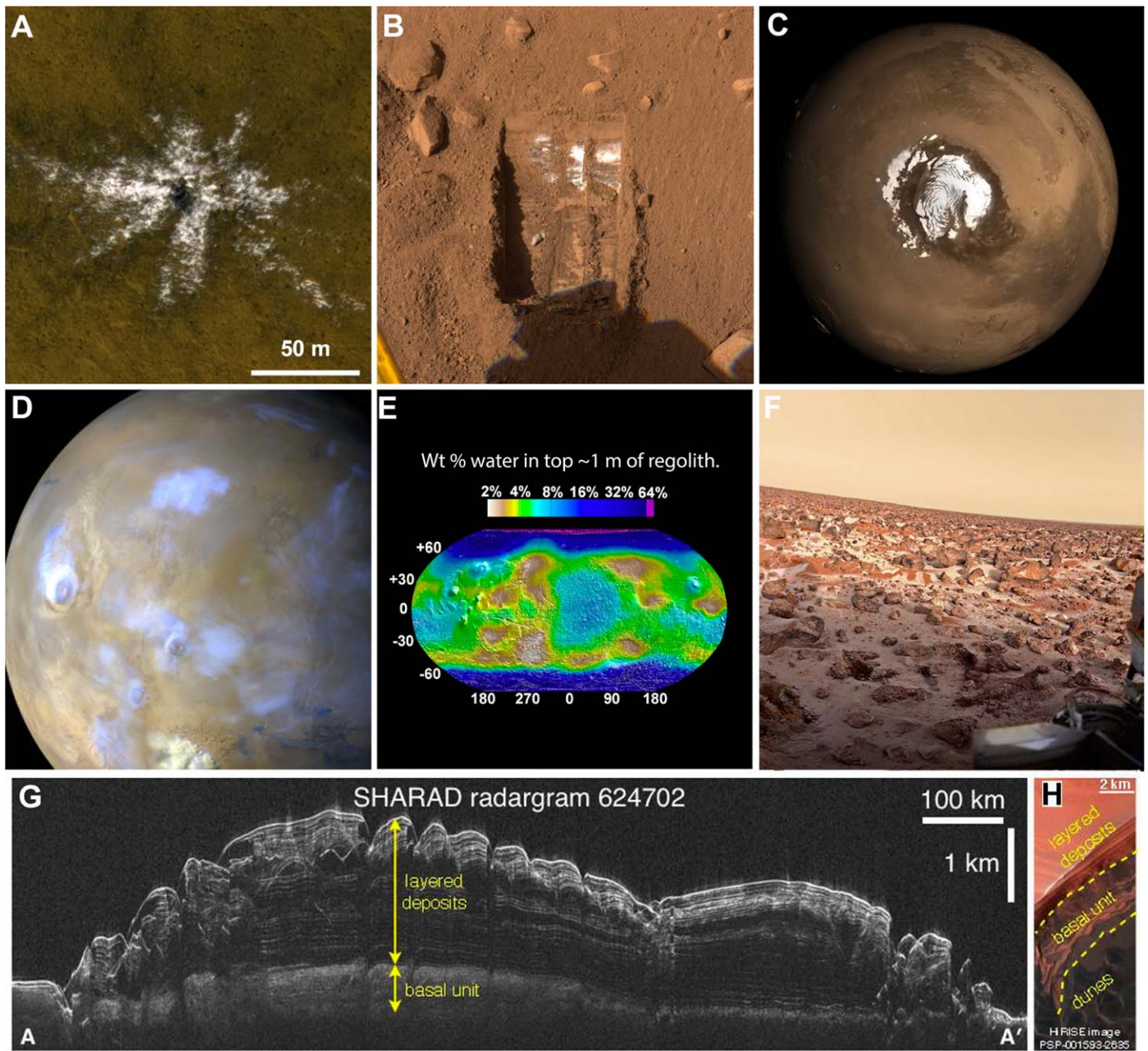


Figure 2. Examples of present-day water ice on Mars. (A) Ice-excavating impact crater imaged by HiRISE. Credit: NASA/JPL-Caltech/UA. (B) Ice exposed in a trench dug by the Phoenix lander. Credit: NASA/JPL-Caltech/UA/Texas A&M. (C) The north polar cap of Mars visualized in springtime. Credit: NASA/JPL-Caltech/MSSS/GSFC. (D) Water ice clouds (blue) imaged by MARCI. Credit: NASA/JPL-Caltech/MSSS. (E) Mars Odyssey GRS map of hydrogen abundance as a proxy for near-surface water ice content. Credit: NASA JPL/Caltech. (F) Early morning water ice frost on Mars imaged by the Viking 2 lander. Credit: NASA/JPL-Caltech/Ted Stryk. (G) SHARAD radargram of the northern polar layered deposits. Credit: NASA/JPL-Caltech/Uni. of Rome/SwRI. (H) HiRISE view of the layers within the northern cap for context. Credit: NASA/JPL-Caltech/UA.

thermal and diffusive properties of the crust as a function of depth, and Mars' internal heat flow ($\sim 8\text{--}25\text{ mW m}^{-2}$) (Solomon & Head 1990; Plaut et al. 2007; Phillips et al. 2008). Local variations in these factors can result in differences in desiccation depths ranging from several meters to over a kilometer (e.g., Clifford 1993).

Heterogeneity in subsurface ice has been mapped at coarse resolution and deeper scales using past GPR instruments Mars Advanced Radar for Subsurface and Ionosphere Sounding (MARSIS) on Mars Express and Shallow Radar (SHARAD) on the Mars Reconnaissance Orbiter (Bramson et al. 2015; Brothers et al. 2015; Stuurman et al. 2016;

Petersen et al. 2018). These instruments, however, cannot map subsurface water ice heterogeneity shallower than 15 m or at horizontal resolutions finer than 10–15 km. As a result, we can observe areas that have bulk amounts of deep relict ice but not areas that are shallow enough to be affected by present-day exchange with the atmosphere. Additionally, while SHARAD has been highly effective at mapping the polar regions and detecting subsurface geologic interfaces below icy deposits in the mid-latitudes, it has performed less effectively at mapping older, rockier, higher-loss (i.e., more attenuating) geologic materials (Stillman & Grimm 2011). Consequently, the picture we have of the Martian subsurface

using our current suite of instruments is highly heterogeneous and incomplete—especially in the shallow subsurface.

In addition to mapping the distribution and quantity of subsurface water ice, the global average atmospheric water vapor is a key factor in determining the extent of stable ground ice on Mars. Modeling has found that diffusion from the atmosphere as the sole source of water can support a ground ice layer within the top few meters (Mellon & Jakosky 1993). Shallow ground ice (>10 cm depth) may persist for as long as >21 million years (Bramson et al. 2017). Recent models suggest diffusive loss of subsurface ice to the atmosphere may be low (Weiss & Head 2017), but spatially and temporally extensive observations linking subsurface and surface ice, as well as their interaction with the atmosphere, do not exist. Mapping meter-scale vertical profiles of subsurface ice distribution and searching for temporal changes will allow us to better understand how volatiles currently move between the subsurface, surface, and atmosphere. This has important consequences for the evolution of Mars’ cryosphere and climate.

1.4. How Does the Martian Lower Middle Atmosphere Respond on Meso- and Global Scales to the Diurnal and Seasonal Cycles of Insolation?

Our present understanding of Mars’ weather is shaped by three aerosols: dust, H₂O ice, and CO₂ ice. Each has important radiative effects (and thermodynamic effects for the ices) throughout the lower and middle atmosphere (0–100 km) at meso- ($\sim 10^2$ km), synoptic ($\sim 10^3$ km), and planetary ($\sim 10^4$ km) scales; connections to climate cycle over geological timescales; and links to extreme and potentially hazardous weather systems. Dust, H₂O ice, and CO₂ ice clouds are the most obvious manifestations of Mars’ weather: they shape and are shaped by atmospheric circulations that have been mostly invisible to past and current observations.

From measurements of the temperature structure (Conrath et al. 2000; McCleese et al. 2010), simulations (Haberle et al. 1993; Forget et al. 1999; Conrath et al. 2000; Rafkin et al. 2002; Hollingsworth & Kahre 2010), visible images of dust storms, and scattered surface measurements (Newman et al. 2017), we can infer the existence of jet streams, extratropical cyclones/fronts, orographic spiral circulations, crater circulations (primarily driven by the density gradients along steep crater slopes), and mesoscale convective systems. In addition, physical modeling of present-day Martian climate dynamics has improved in its ability to represent water and dust cycling over the last decade (e.g., Navarro et al. 2014; Newman & Richardson 2015; Wang et al. 2018; Bertrand et al. 2020; Neary et al. 2020). However, these model improvements were driven by the need to reproduce new types of spacecraft observations (particularly expanded vertical profiling of temperature, dust, and water as vapor and ice). Indeed, modeling the circulation and/or dust and water fluxes throughout the seasonal cycle—including during large dust storms—relies on prescribed dust and/or water distributions. Models are not yet sophisticated enough to explicitly simulate these distributions physically, partly because simulated winds are not accurate. As a consequence, using these models to infer the current circulation without a proper validation with direct wind data poses significant challenges. At the same time, using these models to investigate past climates with different orbital parameters is even more challenging. Therefore, measurements

of winds in the lower and middle atmosphere, along with higher spatial and temporal vertical profiling of the aerosol distribution, are necessary to validate these model inferences, understand the movement of water and dust around the planet, evaluate present-day Mars meteorological hazards, and understand their analogies to Earth meteorology.

Martian dust aerosols chiefly absorb short-wavelength solar radiation. Lifting (“emission” in terrestrial terminology), transport, and sedimentation (“deposition”) of dust are thought to influence the variability of the lower atmospheric circulation on diurnal, seasonal, and interannual timescales (Newman et al. 2002; Lewis & Barker 2005; Montabone et al. 2005; Wilson et al. 2008a; Guzewich et al. 2014, 2016). Snapshot visual imagery, infrared sounding targeting climate questions, and the Mars Orbiter Laser Altimeter (Heavens 2017) have exposed the tremendous diversity and potential menace of dust storms. Dust storms are capable of significant expansion in a few hours and of generating deep convective clouds with altitudes of at least 80 km (Clancy et al. 2010; Heavens et al. 2015, 2018). However, dust storms come in many shapes and sizes that, at a minimum, would present visibility hazards to future human explorers. Some resemble rain and snow-producing weather systems on Earth, while others have no obvious Earth analogs (Kahn 1984; Kulowski et al. 2017).

Although we now know that the peak dust concentration of a dust storm can span two orders of magnitude, we know little about their thermal or aerosol structure at the horizontal, vertical, and temporal length scales resolved by Earth weather forecast models; and we know nothing about the wind field within these systems. Very recent observations from orbit have pointed out large diurnal variability in atmospheric dust content during regional and global dust events, motivating monitoring throughout the diurnal cycle to understand the connection between dust and circulation at this timescale (Kleinböhl et al. 2020; Montabone et al. 2020; Wu et al. 2020).

The meteorological significance of Mars’ water ice clouds is also underexplored. Water ice clouds absorb and emit infrared radiation, but mainly reflect in the visible. This affects the behavior of Mars’ thermal tides (Wilson et al. 2007, 2008b; Steele et al. 2014; Wilson & Guzewich 2014; Kahre et al. 2015; Mulholland et al. 2016). As the tops of thick water ice clouds cool at night, they can become unstable and be an important agent of convective mixing in the lower atmosphere (Spiga et al. 2017), and consequently may cause ice-laden currents of air to descend to the surface. These downdrafts could pose potential hazards to helicopters and other aircraft. This phenomenon is only known from individual observations at the 200 km scale, far above the length scale of snow squalls or downbursts on Earth.

Winter polar nights can be so cold that CO₂, the principal atmospheric constituent, condenses into precipitating ice clouds in tandem with direct deposition of CO₂ ice onto the polar cap (Colaprete & Toon 2002; Hayne et al. 2012, 2014). Some of these clouds are convective, driven by the latent heating of CO₂ itself, producing potentially violent squalls that litter the polar cap with fresh, poorly emissive CO₂ snowfall. Condensation and sublimation of clouds affect the thermodynamic budget of the cap, while re-emission of infrared radiation by high clouds affects its radiative balance. Snowfall and dust deposition affect the cap’s radiative balance even in the sunlit months by modifying its albedo and emissivity (Hayne et al. 2012, 2014). Latent heat released during the polar nights by CO₂

MY 24 ; Ls~220° ; Sol-of-Year 448

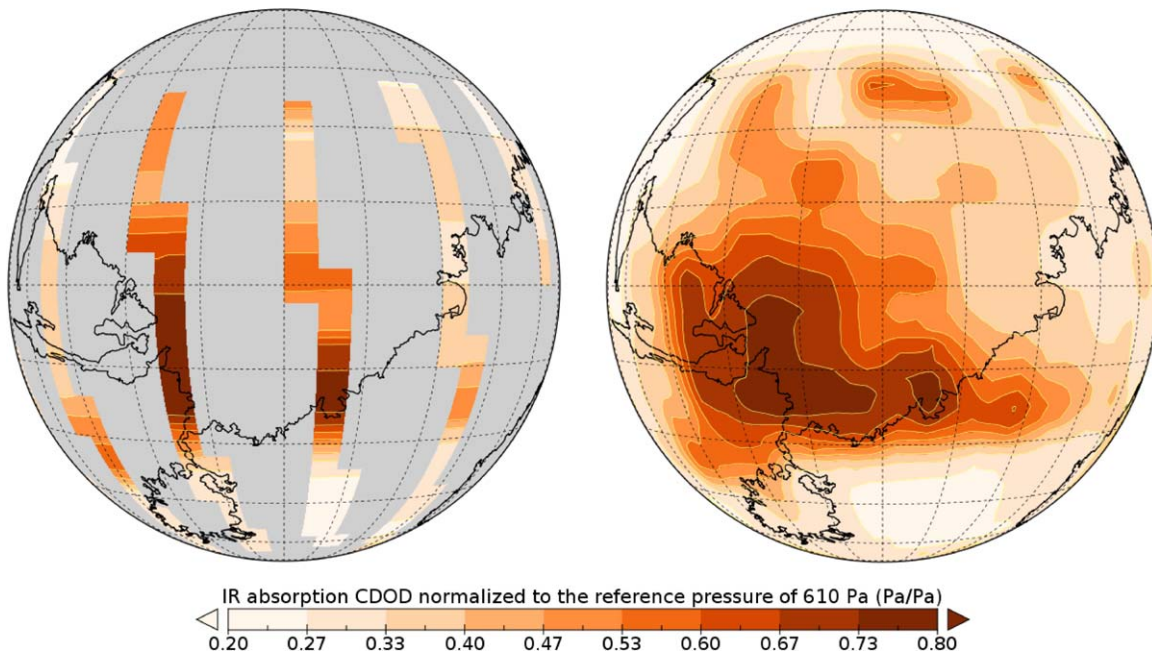


Figure 3. The left panel shows a regional dust storm as seen by a single Sun-synchronous polar orbiter, while the right panel represents a synthetic view of the same storm from areostationary orbit. Both panels use vertical perspective projections with a center distance of 6.03 Mars radii. IR opacity data are from MGS/TES. Gray areas imply missing data. The storm in the right panel is reconstructed following the methodology detailed in Montabone et al. (2015).

condensation is thought to maintain the very unstable shape of the Martian polar vortices (Toigo et al. 2017). However, all current information we have about vortex dynamics comes from indirect data gathered by numerical simulations, with no direct observation to validate against.

Because of Mars' relatively short radiative relaxation timescale compared with that of Earth (~ 1 day versus ~ 1 month), the diurnal cycle of insolation shapes Martian weather more than on Earth (Read et al. 2015). This diurnal meteorological variability argues for observations spanning the diurnal cycle. However, to date, most measurements have been fixed in local time, or have spanned different local times but at different locations over many sols, leaving major questions unanswered. As an example, Figure 3 demonstrates how difficult it is to understand the dynamics of a dust storm if observed by one single polar orbiter compared with full-disk (synthetic) observations by an areostationary satellite. A dust storm during its expansion phase can grow a factor of 10–20 in area in a week (Cantor 2007), such that a single polar orbiter is only able to observe pieces of it asynchronously. Only a reconstruction of the general characteristics of a storm, carefully made using a week's worth of polar data, can provide a satisfying—albeit approximate—picture of how the dust storm really developed.

Moreover, fixed local time measurements and limited understanding of weather systems that mobilize and transport dust have presented a challenge for data assimilation in Mars general circulation models (Lee et al. 2011; Zhao et al. 2015; Navarro et al. 2017). Data assimilation is a set of formal statistical techniques widely used in Earth weather forecast modeling that use observations to constrain model behavior and better resolve the true state of the atmosphere at a particular time. In addition to improving weather prediction, data assimilation can be used to trace the past trajectory of air masses, and thus could help discover the sources of mysterious

trace gases like methane. However, improvements in both model physics parameterizations and quantity/quality of the assimilated observations will be necessary to achieve these aims.

Determining the dynamics and variability of Mars' meso- to global-scale circulations requires continuous, simultaneous, and global observations of Martian aerosols, temperature, and winds throughout the lower and middle atmosphere with respect to longitude, latitude, altitude, local time, and season.

1.5. How Does Coupling with the Lower Atmosphere Combine with the Influence of Space Weather to Control the Upper Atmospheric System and Drive Atmospheric Escape?

1.5.1. Mars' Upper Atmosphere

Mars' upper atmosphere can be broadly defined as the region where the space weather environment (solar extreme ultraviolet (EUV), solar wind, and solar storms) is an important driver of structure and dynamics. The thermosphere (Bougher et al. 2014) begins at the homopause (~ 100 – 120 km), above which neutral species have separate mass-dependent scale heights. It extends to the exobase (~ 200 km), above which collisions no longer dominate particle motion. Above the exobase is the tenuous exosphere, consisting mostly of atomic species (some fraction of them escaping) and extending out to many Mars radii. Embedded within the thermosphere and exosphere is the charged and conducting ionosphere, mostly the result of solar EUV photoionization of neutrals. The ionosphere and the planet's patchwork of crustal magnetic fields (Acuña et al. 2001) together form a complex obstacle to the solar wind, resulting in induced magnetic fields, electric fields, and highly variable plasma flows. These interconnected regions form the “upper atmosphere system,” i.e., the reservoirs from which—and the channels through which—atmospheric escape has

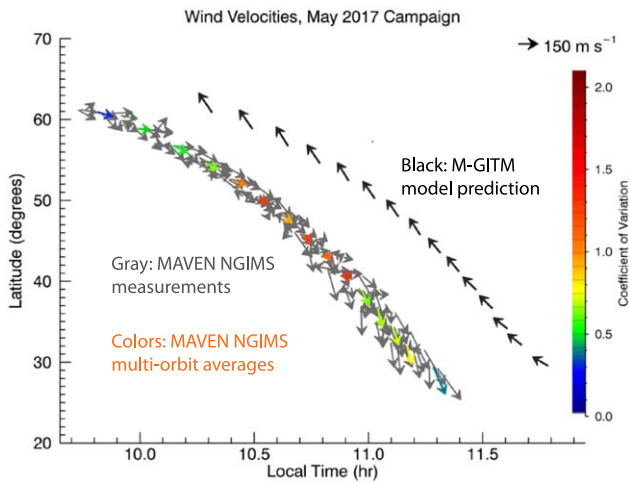


Figure 4. Dynamics in Mars’ thermosphere are poorly understood. Very sparse in situ MAVEN wind data is highly variable, often disagreeing completely with leading models. Figure shows measured and modeled thermospheric winds (140–240 km altitude). The coefficient of variation provides a dimensionless scalar measure of the orbit-to-orbit variability of the winds in both direction and magnitude. Details are contained in Roeten et al. (2019), wherefrom figure is reproduced with permission. Comprehensive remote wind measurements are needed.

dramatically reshaped the climate throughout Martian history (Jakosky et al. 2018).

1.5.2. Thermosphere Dynamics

The basic composition and structure of the thermosphere has been observed (e.g., Mahaffy et al. 2015), to show seasonal and solar cycle variations that roughly match global models after significant averaging (Jain et al. 2015; Bougher et al. 2017). The dynamics of the thermosphere are dominated by atmospheric waves, ranging from small-scale gravity waves (Yiğit et al. 2015) to global tides (England et al. 2016; Liu et al. 2017). These waves impact the dynamics, energetics, and composition of this region, all of which influence atmospheric escape. The character of these waves appears to change as they propagate upward from the homopause through the thermosphere (Yiğit et al. 2015), but how these waves drive dynamics and deposit energy at high altitudes remains unknown.

The limited set of in situ wind measurements by MAVEN-NGIMS (Mahaffy et al. 2014) from ~140 to 240 km (Benna et al. 2019; Roeten et al. 2019) has begun to reveal wind patterns, but the observed variations of 100–200 m s⁻¹ over ~4 hr (as large as the mean winds themselves) cannot be explained by current atmospheric models (see Figure 4). Such winds, as well as density variations caused by waves, can affect aerobraking and the entry, descent, and landing (EDL) of spacecraft. The generation, propagation, and dissipation of atmospheric waves between the surface and the thermosphere remain unknown and require systematic, simultaneous measurements of winds and density structures over a broad range of altitudes.

1.5.3. Lower–Upper Atmosphere Connections

Evidence now suggests that the lower and upper atmospheres of Mars are more closely connected than previously realized. First, the exospheric atomic hydrogen (H) density and associated escape rate varies by a factor of 10–20 with season (Chaffin et al. 2014; Clarke et al. 2014; Bhattacharyya et al. 2015), with the

highest densities and rates near perihelion. Meanwhile, the middle atmospheric water abundance, which responds strongly to dust events (Fedorova et al. 2018; Vandaele et al. 2019), is correlated with this H escape (Heavens et al. 2018), with models suggesting that this water could be the main factor driving the escape (Chaffin et al. 2017; Shaposhnikov et al. 2019; Neary et al. 2020), as shown in Figure 5.

Despite this, more information is needed to distinguish between proposed mechanisms, e.g., upslope winds (Rafkin 2012), fast-moving dust clouds (Spiga et al. 2013), or sophisticated dust-ice microphysics (Navarro et al. 2014). Adding to these complexities is the multidimensional nature of the climate system, which can exhibit different transport mechanisms and patterns at different altitudes, latitudes, longitudes, local times, and seasons.

Second, dust activity in the lower atmosphere appears to be connected to significant depletion of atomic oxygen (O) in the thermosphere (Elrod et al. 2019). Atomic O mediates the conversion of the primary ionospheric ion CO₂⁺ into the dominant ion O₂⁺, which dissociatively recombines (O₂⁺ + e⁻ → O + O + E_{kinetic}) to produce a hot O exosphere, the dominant source of escaping O today (Lillis et al. 2017). Synoptic tracking of lower atmospheric dust loading, middle atmospheric water abundance, upper atmospheric H and O response, and the temperature structure at all altitudes across multiple dust events is required to decipher the processes by which the lower atmosphere drives the upper atmosphere and escape.

1.5.4. Ionosphere Structure and Dynamics

Mars’ ionosphere is a complex ionized region primarily produced by solar EUV, but also influenced significantly by several other factors: crustal and induced magnetic fields, solar X-rays, cosmic rays, atmospheric waves, and ambipolar electric fields (Figure 6, from Sánchez-Cano 2019). Below 200 km altitude, the collision rate is high enough to maintain photochemical equilibrium. Here, the dayside ionosphere broadly agrees with theory (Benna et al. 2015; Vogt et al. 2017), with densities higher and temperatures lower where plasma is trapped within “miniature magnetospheres” over strongly magnetized crust (Andrews et al. 2015; Flynn et al. 2017). The nightside ionosphere is complex and governed by transport from the dayside and ionization by precipitating electrons (Girazian et al. 2017a, 2017b; Adams et al. 2018; Lillis et al. 2018).

Above the photochemical region is the highly variable “upper ionosphere,” where plasma transport dominates and most ion escape originates. Ions in this region are heated by plasma waves from in the solar wind (Fowler et al. 2017, 2018a, 2018b; Collinson et al. 2018) and accelerated by electric fields (Xu et al. 2018; Akbari et al. 2019) and magnetic tension forces. The interplanetary magnetic field (IMF) drapes around the planet, driving a strong hemispheric asymmetry in the ionosphere and the motion of escaping ions (Dubinin et al. 2018). These ionospheric dynamics can also disrupt communication and navigation on Mars (see next section).

Any single spacecraft cannot be in two places at once, which is the minimum needed to characterize the real-time response of the ionosphere to variable forcing by the solar wind. This has introduced significant, unquantifiable uncertainty in studies to date. Further, in situ observations have been limited to widely separated swaths (one per orbit, every ~4.5 hr), yielding

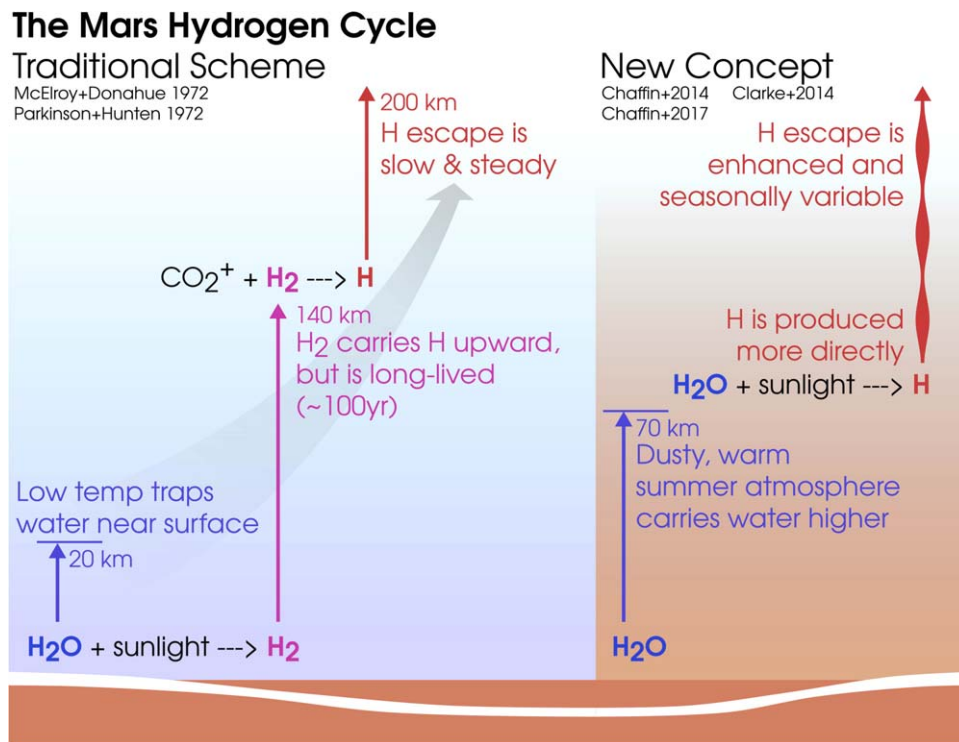


Figure 5. Mars’ upper atmosphere responds strongly to lower atmospheric dust forcing. H concentrations and escape rates increase while O decreases, and the global circulation is affected by even regional storms. That is to say, Mars’ evolution is closely coupled to climate, but the mechanisms that govern this coupling remain a mystery due to the lack of global-scale coordinated observations of the lower and upper atmosphere.

insufficient coverage to determine the large-scale or short-or-medium-timescale response of the ionosphere to dynamic events. To reveal how the ionosphere responds to space weather, this weather and the response of global distribution of ionospheric plasma must be measured at least hourly.

1.5.5. New Perspectives on Mars’ Magnetosphere

Mars has a unique “hybrid” magnetosphere because it shares properties of both unmagnetized planets (e.g., Venus) and magnetized planets (e.g., Earth and Jupiter), as shown in Figure 7. Multipoint plasma missions have revolutionized understanding of the terrestrial magnetosphere over the last 20–25 yr (Paschmann & Daly 1998; Gustafsson et al. 2001; Angelopoulos et al. 2008; Lanzerotti 2013; Fuselier et al. 2016). Similarly, coordinated two-point measurements would transform our understanding of Martian plasma dynamics, including ion escape (Paschmann & Daly 1998). For example, time-separated measurements across the same plasma boundary or within the same volume allow us to determine how the boundary moves/changes or how conditions within that volume change. Spatially separated simultaneous measurements made within a plasma region unambiguously reveal how conditions vary over a range of spatial scales. Simultaneous measurements of the upstream solar wind and plasma conditions in the Martian magnetosphere allow us to observe its response to solar wind disturbances in near real time (Ma et al. 2014). Leveraging the success of terrestrial multipoint plasma missions, simultaneous measurements from multiple platforms are needed to reveal the dynamic response of the magnetosphere to the highly variable space weather environment. Lessons learned here will have applicability to understanding

plasma dynamics and atmospheric loss from similarly unmagnetized terrestrial planets such as Venus or exoplanets.

1.6. What Will Human Explorers Need?

Crewed missions to Mars, including those sent to establish a sustained human presence, will require explorers to foresee and mitigate hazards, identify and utilize resources, track their location, and communicate with Earth. Water—essential for both life support and propellant synthesis—is available as ice at mid-latitudes and the poles. Human missions will likely depend on this ice, so sites with ice shallow enough (e.g., 0–20 m) to be easily accessible must be characterized. The Human Precursor Strategy Analysis Group (P-SAG; Beaty et al. 2012) prioritized identifying shallow ice and its depth variation (Activities D1–5 and D1–6).

Dust climatology observations (B1–1) and validation of Mars atmospheric models (A2–1) are currently too limited to confidently design human missions to the planet. P-SAG prioritized observations of temperature, wind, and aerosols, at all local times and with 10 km horizontal resolution, as well as comprehensive observations of dust activity (A1–1, A1–2, and A1–3).

Charged particle radiation can penetrate spacesuits and habitats to cause cancer and even radiation sickness among human crews in Mars orbit (Moyers et al. 2006). Despite past measurements (Zeitlin et al. 2004), we have not characterized the energetic particle radiation environment over a full solar cycle and Mars’ range of heliocentric distances (1.38–1.62 au). Such characterization is important to forecast expected crew radiation dose in Mars orbit.

A robust communication and positioning infrastructure capable of accurate location, high data volume, and short

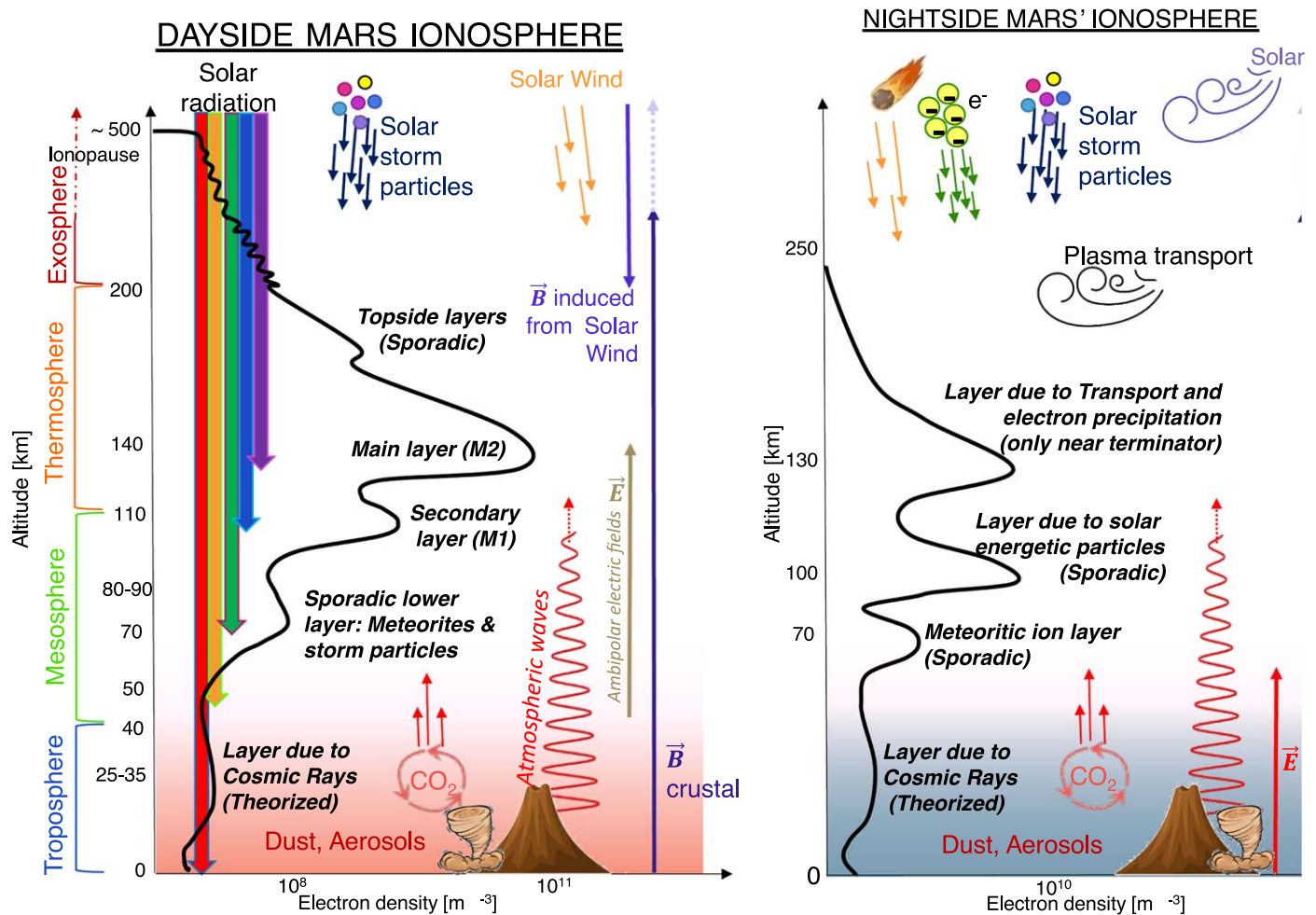


Figure 6. Mars' ionosphere (density in black) is embedded mostly within the upper atmosphere and is influenced by a number of planetary and space weather factors. Regular global measurements of the ionosphere and space weather environment are necessary to understand the processes driving its variability, which disrupts communications and global positioning (Mendillo et al. 2004). Reproduced from Sánchez-Cano (2019).

latency between surface assets, orbiters, and Earth should be in place to ensure effective decision-making when we have a human presence on Mars. Satellite platforms, sent to make measurements in anticipation of human missions, serve as a convenient and logical testbed for elements of a robust communication infrastructure. One feature of this infrastructure will be reliable radio transmission, which we expect will be an important element of communications at Mars and then to Earth. Mars' ionospheric variability must be characterized to determine its likely effect on positioning and communication (Mendillo et al. 2004; Sánchez-Cano et al. 2019). In addition, we must determine the most efficient ways orbiters and surface assets can coordinate to maintain near-continuous contact with Earth. Vetting promising new technology such as deep space optical communications (DSOC) and delay-tolerant networking (DTN) on a human precursor mission provides opportunity for risk mitigation.

2. Mosaic Science Traceability

The Mars Orbiters for Surface-Atmosphere-Ionosphere Connections (MOSAIC) mission is a strategic constellation of ten spacecraft that addresses the high-priority science and exploration questions described in the sections above. MOSAIC has two main goals: Goal I is to “Understand Mars’

present-day climate processes and their interconnections, from the subsurface to the solar wind,” and Goal II is to “Identify hazards, characterize resources, and demonstrate technologies to enable the Human Exploration of Mars.” These Goals are addressed through the achievement of several Scientific Objectives and Human Exploration Objectives that, in turn, are fulfilled by different combinations of eight Investigations.

Investigation number roughly increases with altitude. Investigation 1 will map the three-dimensional distribution of ice from the surface down to the shallow subsurface (10 m). Investigation 2 is to measure atmospheric structure, specifically the altitude distribution of pressure, winds, aerosols, water vapor, ozone, and temperatures in the lower and middle atmosphere (<80 km). Investigation 3 is to characterize the complete diurnal and geographic behavior of the lower-middle atmosphere, and short-timescale evolution of Martian dust and ice clouds as the atmosphere responds to changing insolation. Investigation 4 is to measure the global 3D composition, structure, and winds in Mars' thermosphere (90–200 km) and how they vary. Investigation 5 is to measure the density and temperature structure of the Martian ionosphere (90–400 km) and how they vary. Investigation 6 is to characterize the 3D structure and variability of densities and escape rates within the hydrogen and oxygen exospheres.

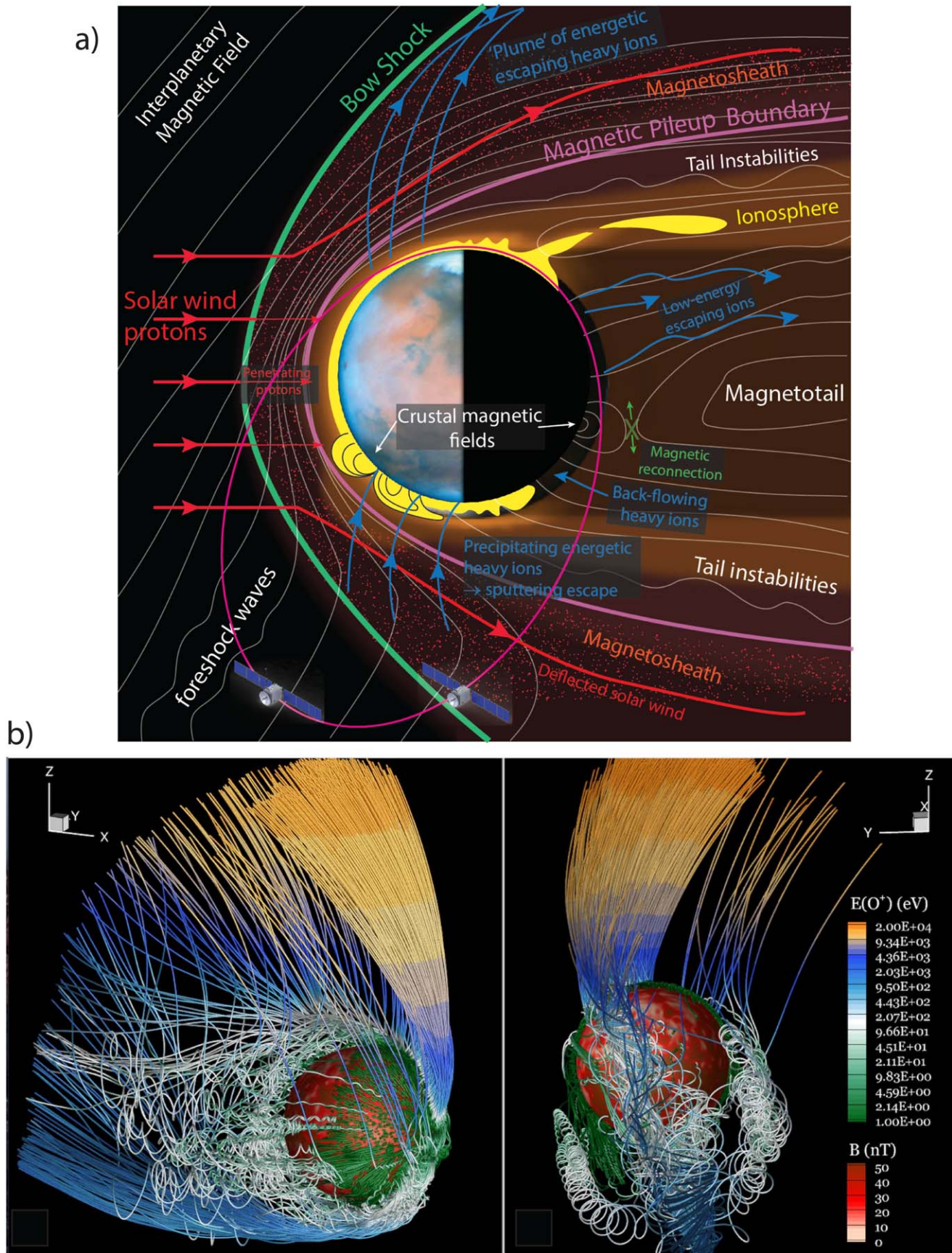


Figure 7. (a) Multipoint plasma measurements are needed to understand mass and energy flows throughout Mars' uniquely rich and interconnected hybrid magnetosphere. (b) Simulation of the acceleration of planetary ions by the solar wind interaction with Mars. Planetary ions are shown in colors that indicate ion kinetic energy, from green (up to a few 10s of eV) to orange (>10 keV), using the model results of Fang et al. (2008). Magnetic field strength is shown in shades of red on a constant altitude surface. Coordinates are Mars solar orbital.

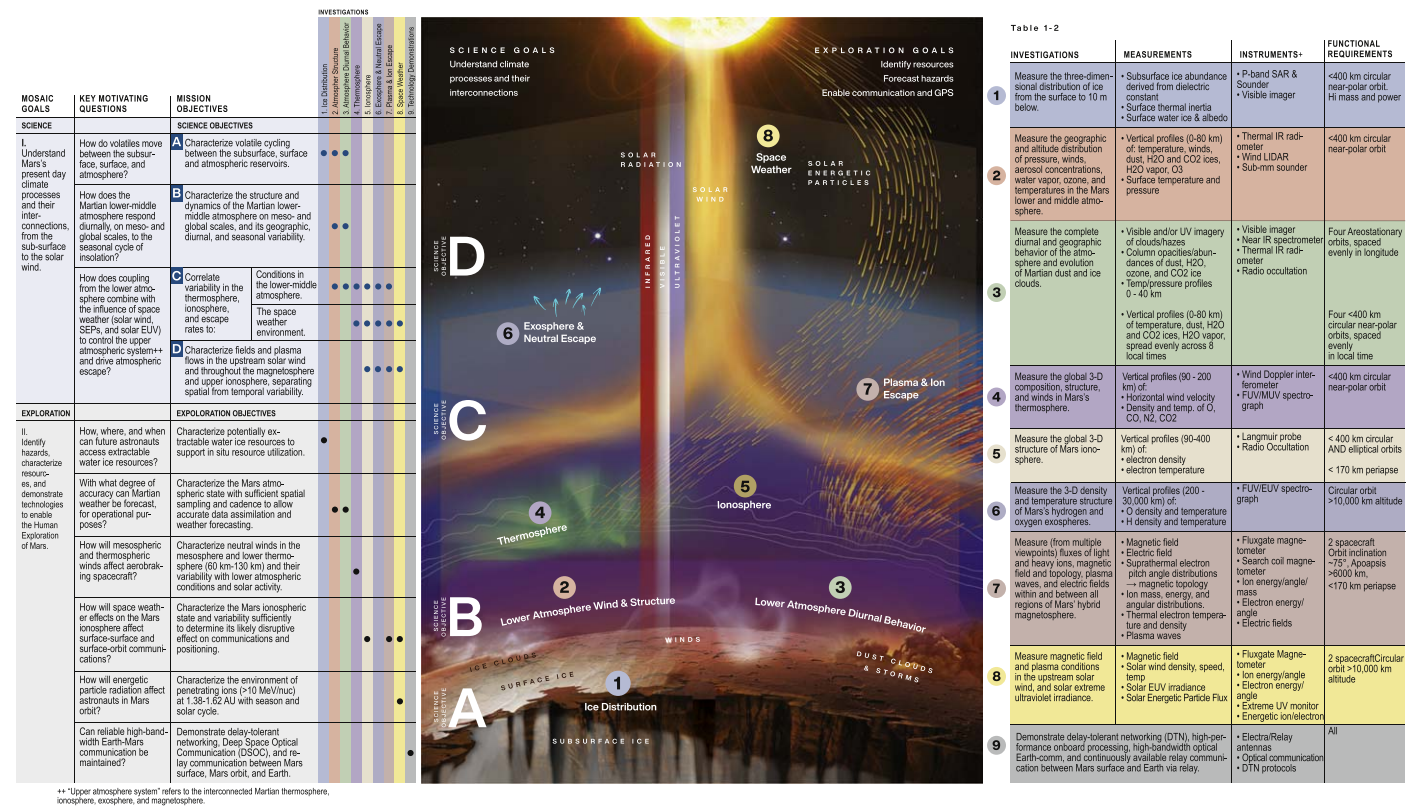


Figure 8. MOSAIC Traceability. From left to right: Goals and Key Motivating Questions trace to Objectives, Investigations, Measurements, Instruments, and mission functional requirements.

Investigation 7 is to make multipoint measurements of the Martian plasma environment, in particular ion escape and precipitation rates and magnetic field geometry and topology. Last, Investigation 8 is to characterize upstream solar influences on the Martian atmosphere: EUV irradiance, solar wind density and velocity, energetic particles, and the strength and direction of the interplanetary magnetic field.

Figure 8 contains MOSAIC's science traceability. The left side traces Goals to Investigations, while the right side traces Investigations to specific required measurements, relevant instruments to make those measurements, along with related mission functional requirements (e.g., the specific orbital perspective required for a given measurement). Section 4 and Appendices A.2–A.7 describe in detail the measurement requirements for each Investigation and prospective instruments that can meet those requirements.

In order to demonstrate the value of the MOSAIC investigations with respect to the current state of knowledge in the field, Figure 9 shows an assessment of the scientific usefulness (colors), compared to the current state of knowledge (letters), of each of the proposed measurements, with regard to understanding the interconnections of the Martian climate system. As can be seen, significant and sometimes large gaps in understanding still exist, with several important quantities having never been systematically measured before (e.g., shallow subsurface ice, winds in the lower and upper atmospheres, spatiotemporal dust dynamics, global structure of the ionosphere, spatiotemporal plasma dynamics, and real-time response to heliospheric disturbances).

MOSAIC's unprecedented investigations will both enable the safe human exploration of Mars and revolutionize our understanding of the processes by which matter and energy move within and between the reservoirs of the Martian climate

system, driving current climate and past climate evolution. The following section describes the mission architecture required to complete the MOSAIC Investigations.

3. Mission Concept

In order to complete the investigations detailed in the previous section, the MOSAIC mission concept consists of 10 individual orbiting spacecraft hosting 49 individual instruments. The ten spacecraft are to be delivered in three different types of orbits: near-polar Sun-synchronous, inclined elliptical, and areostationary. The individual spacecraft are based on six unique “platforms.” A platform refers to a modular spacecraft design that can support similar payloads and orbit types. Figures 10 and 11 show the six MOSAIC platforms: Mothership, Polar, Elliptical, Areostationary (abbreviated hereafter as Areo) Carrier, Areo SmallSat A, and Areo SmallSat B, and their associated science instrument payloads, color-coded by the investigations addressed by those instruments. The ten-satellite constellation consists of a single Mothership, three Polar small satellites, two Elliptical spacecraft, a single Areo Carrier, a single Areo A SmallSat, and two Areo B SmallSats. Figure 11 provides technical specifications of the spacecraft. Standard science operations would begin when all spacecraft are in their required science orbits. The baseline Science Mission would last two Martian years (slightly <4 Earth years) in order to characterize the Mars climate system in all seasons and investigate interannual variability to a limited degree.

3.1. The MOSAIC Platforms

The Mothership platform, in its low-altitude (~300 km) circular near-polar Sun-synchronous orbit, is primarily

Charcterizing the effect of ↓ on →:			Ice	Lower Atmosphere structure					Thermo- sphere	Iono- sphere		Exosp here	Magn etosp here	Space weather drivers								
MOSAIC will enable, w.r.t. current/planned observations:		Characterized alone?	Shallow Subsurface	Surface	Temp, pressure	Dust	H2O (g) /condensates	Wind/dynamics	Temp, pressure	Composition	Wind/dynamics	Temp, density	Composition	Dynamics	Structure	Dynamics/ Neutral escape	E, B Fields	Flows & ion escape	Solar wind	IMF	Solar EUV	Energetic Particles
Groundbreaking improvement																						
Significant Improvement																						
Incremental Improvement																						
Ice	Shallow subsurface	B		B	P	P	B		First systematic observations of shallow subsurface material properties										Areostationary observations			
	surface	I	B		B	B	I	P														
Lower Atmos- phere	Temp, pressure	I	B	I		I	I	B	B	B	P	P	B	P	B	B	P	P			First systematic lower atmosphere wind measurements	
	Dust	I	P	B	I		B	P	B	B	P	B	B	P	B	B	P	P				
	H ₂ O/condensates	B	P	B	I	I		P	B	P	P	B	B	P	B	B	P	P				
	Wind/dynamics	P		P	P	P	P		P	P	P	P	P	P	P	P	P	P				
Thermo- sphere	Temp, pressure	I		MAVEN measurements exist						I	P	I	I	P	I	I	B	B			High-res observations of aerosols and water vapor	
	Composition	I							I		P	I	I	P	I	I	B	B				
	Wind/dynamics	P							P	P		P	P	P	P	P	P	P				
Iono- sphere	Temp, density	I									P		B	B	B	B	B	B			First systematic thermosphere wind measurements	
	Composition	I									P	I		B	B	B	B	B				
	Dynamics	B							B		P	B	B		B	B	B	B				
Exosphere	Structure	I									I	I	B		B	B	B					
	Dynamics/Neutral Escape	B									B	B	P	P			B	B				
Magnetos- phere	E, B fields	I									B	B	P	B	B	B	B	B				
	Flows & ion escape	I									B	B	P	B	B	B	B	B				
Space weather drivers	Solar wind	M									B	B	P	B	B	B	B	B	B			
	IMF	M									B	B	P	B	B	B	B	B	B			
	Solar EUV	M									I	I	P	I	I	P	I	B	B	B		
	Energetic Particles	M					P				B	B	P	B	B	P						

Figure 9. Pre- and (expected) post-MOSAIC understanding of Mars atmospheric system connections. Letters represent current understanding of the effect of the row quantity on the column quantity, from P (poor understanding) to M (relatively mature). Colors represent expected improvement in understanding enabled by MOSAIC: incremental (orange), significant (yellow), and groundbreaking (green). Green boxes containing B and P represent the greatest promised improvements. Note: characterization of spatial and temporal variability is implied for each of these variables. Text boxes explain why MOSAIC will (or will not in some cases) improve understanding of connections. “Characterized alone” means not measured simultaneously with respect to other variables.

responsible for mapping the shallow subsurface ice distribution using a *P*-band (250–500 MHz) synthetic aperture radar (SAR), as well as performing vertical profiling of several key atmospheric quantities in the lower atmosphere, middle atmosphere, and thermosphere. Lower-middle atmosphere quantities to be measured include dust, ice, water vapor, and temperature using an IR radiometer, and (for the first time) wind vectors using a combination of lidar and submillimeter sounders. It will simultaneously measure structure and

composition of the thermosphere using an imaging ultraviolet spectrograph, as well as (also for the first time) two-component horizontal winds using a Michelson interferometer. The spacecraft is a large solar electric powered bus with accommodation for a 6 m *P*-band radar antenna, large flexible solar arrays, and an articulated 3 m high-gain antenna for science data return. The Mothership is responsible for carrying and providing dedicated telecommunications relay for the Polar and Elliptical platforms. Figure 12 shows the

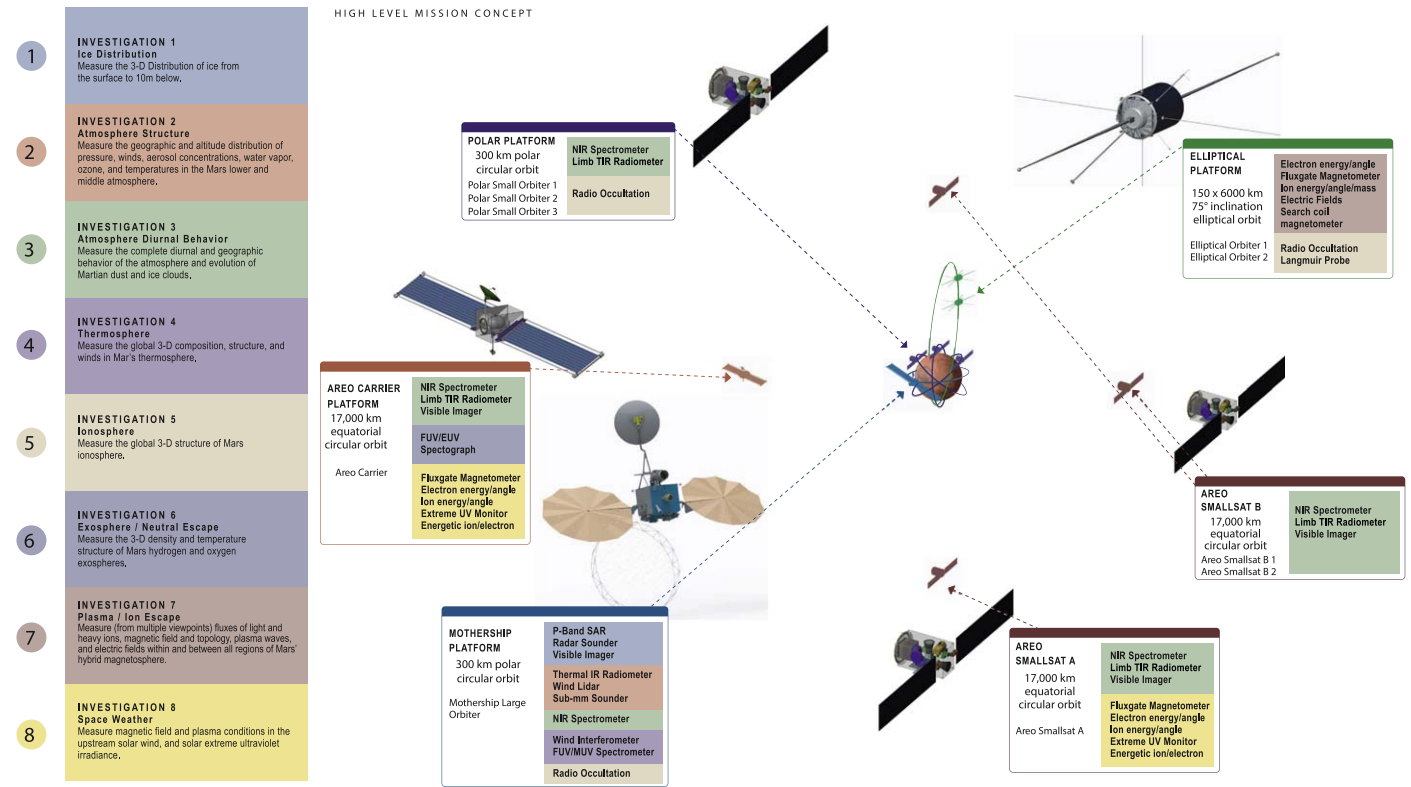


Figure 10. MOSAIC platforms and associated instruments, color-coded by investigation (same color label as Figure 8).



Figure 11. MOSAIC spacecraft characteristics. + Refer to Figure 9 for full instrument list. ++ Only Areo Smallsat Platform “B” shown. Refer to Figure 9 for Areo Smallsat Platform “A” instrument list. Color icons show relative size scale.

telecommunication architecture for the MOSAIC constellation. The Mothership will act a relay link between the Polar and Elliptical platforms, and will store and forward data

using an X-band direct-to-Earth (DTE) link. Each of the Areostationary platforms will have independent DTE telecommunication capability.

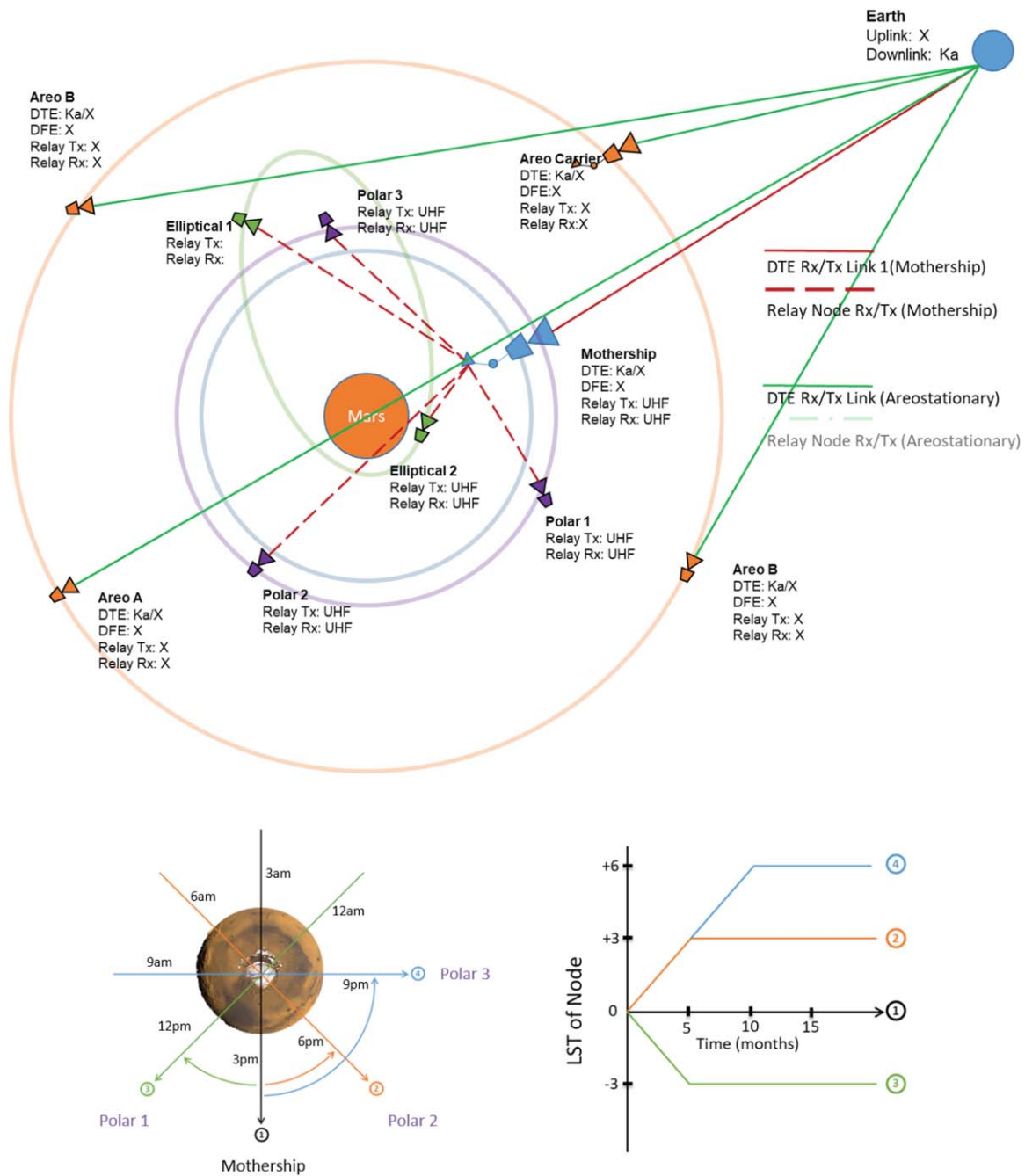


Figure 12. (Top) MOSAIC communications architecture. Orange represents the areostationary elements. The purple circle represents the polar orbiters. The green oval represents the elliptical orbiters, while the gray circle represents the mothership. (Bottom Left) Local time separation of polar-orbiting smallsats. (Bottom Right) Time required to reach local times of final science orbits.

The Polar platform orbiters' primary objective is to obtain simultaneous vertical atmospheric profiles of dust, ice, water vapor, and temperature using three <100 kg spacecraft with 300 km circular near-polar Sun-synchronous orbits with ascending nodes spaced along with the mothership at 3 hr intervals in local solar time (see Figure 12) (Kleinböhl et al. 2018). They will also host antennas for performing radio occultations (Figure 17) with the Elliptical spacecraft, described below.

The two Elliptical-orbit spacecraft occupy the same $150 \text{ km} \times 6000 \text{ km} \times 75^\circ$, $\sim 4.5 \text{ hr}$ precessing orbit. They will make in situ plasma measurements in all of Mars' key plasma regions: the magnetosheath, magnetic pileup region, ionosphere, and

double-lobed magnetotail. J2 gravity perturbations to the orbit and Mars' changing tilt with respect to the solar wind provide a wide range of geometries from which to study the dynamic interaction of the solar wind with Mars' upper atmosphere. One spacecraft will follow the other in a "pearls on a string" formation with temporal separations that will vary between 5 and 30 minutes. As well as measuring energy and angle distributions of ions and electrons and both the morphology and topology of Mars' magnetic fields, they will also measure (for the first time) the DC electric fields that drive both aurora and ion escape at Mars, requiring a spinning platform with long booms that extend from the faces and sides of the cylindrical spacecraft bus.

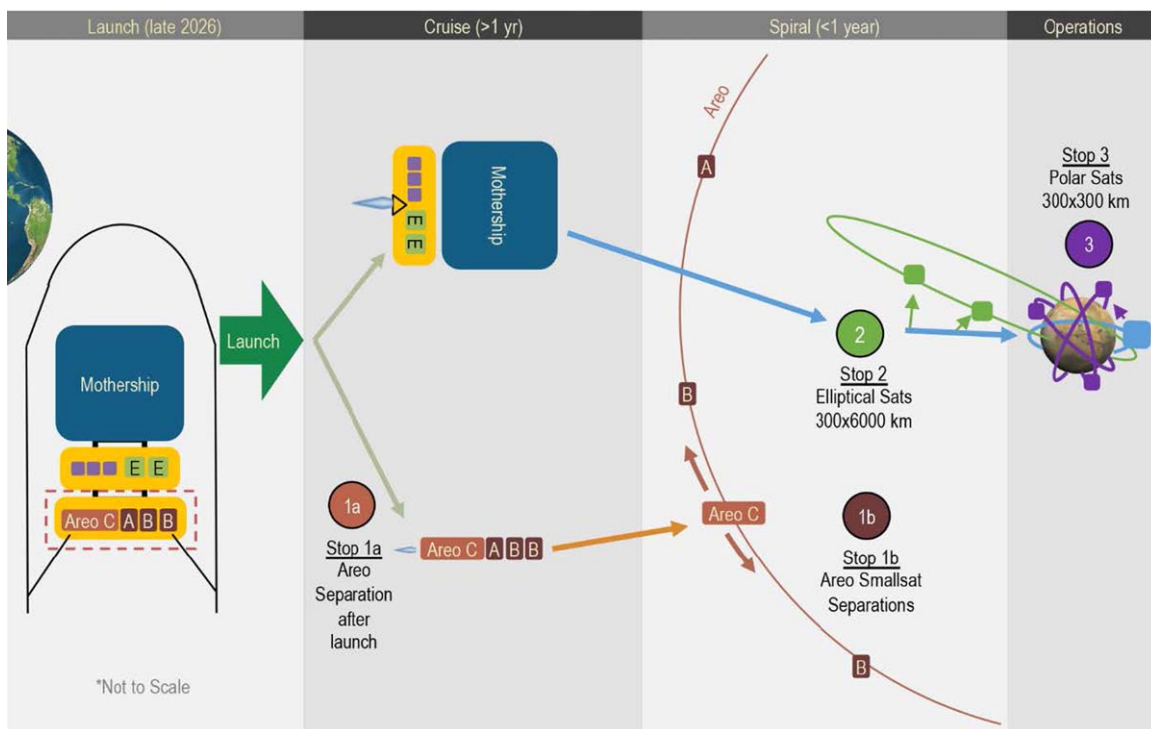


Figure 13. MOSAIC constellation delivery concept.

Finally, the four Areostationary platforms, namely Areo Carrier and Areo SmallSats A and B, are in $\sim 17,000$ km circular equatorial orbits similar to geostationary orbits at Earth. They will be placed 90° apart in longitude. These orbits enable two complementary types of observations. First, their fixed vantage points over the equator allow continuous monitoring of lower atmosphere dust opacity, clouds, and temperature profiles up to 50 km with all four spacecraft, providing coverage of the entire planet up to 70° north and south latitude, with longitudes underneath each satellite visible up to 80° north and south. Second, Areo Carrier and Areo A will be placed 180° apart in longitude, ensuring that at least one is always in the upstream solar wind. These will host space weather instrumentation, monitoring solar wind conditions, the interplanetary magnetic field, and energetic particle storms that constitute a radiation hazard to astronauts in orbit.

3.2. Constellation Delivery and Mission Design

The number of scientific objectives, instruments, platforms, and mission requirements of the MOSAIC concept lead naturally to a large trade space in terms of launch, cruise, and transition to science orbits. However, the requirement to make measurements simultaneously among the constellation drives a mission design that allows for contemporaneous arrival. Fortunately, it was found that the full constellation could be launched from a single affordable, dedicated, medium-class launch vehicle.

At the extremes, each mission element could either be delivered by one master propulsion module, or each could have its own propulsion, making its way from launch to final destination. Between those extremes, there are several combinations of elements with larger propulsive capabilities delivering those with smaller or no propulsion.

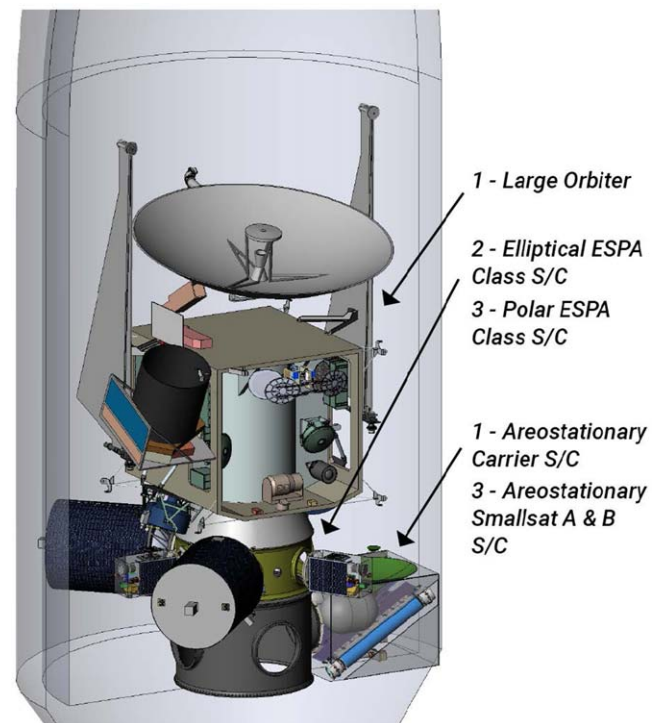


Figure 14. MOSAIC constellation stacked within a standard 5 m launch vehicle fairing.

Figure 13 illustrates one potential method to deliver the full baseline MOSAIC constellation on a single launch. The full stack mass is such that it could be launched on a Falcon Heavy Recoverable or equivalent. In its launch configuration, the mothership would sit atop two ESPA rings, as shown in Figure 14. The Areo Carrier and Areo SmallSats A/B satellites

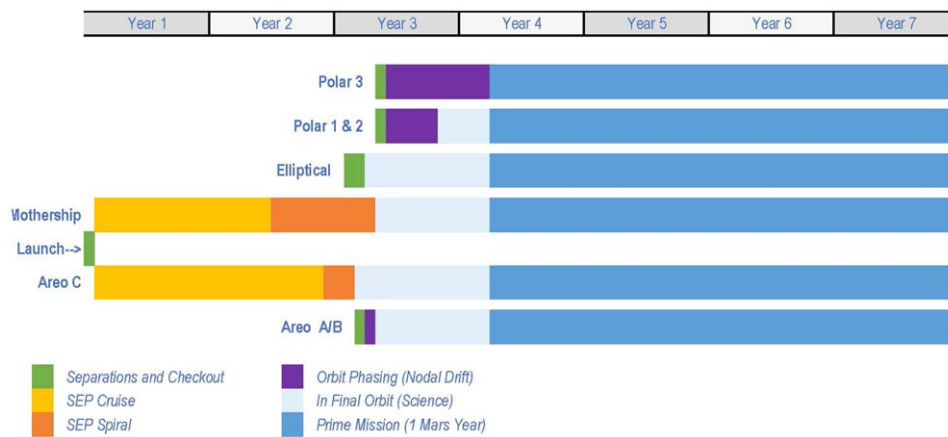


Figure 15. Example timeline for the MOSAIC constellation.

attach to the lower ring whereas the upper ring carries the elliptical and polar satellites on five ports.

Shortly after launch to a low-energy escape trajectory, the delivery sequence is as follows:

1. The Areo Carrier, along with the Areo SmallSat A/B platforms, separates (Stop 1a in Figure 13) from the lower ESPA ring (which remains attached to the launch vehicle upper stage).
2. The SEP system in the Areo Carrier element propels all four elements to rendezvous with Mars and spiral down to areostationary orbit.
3. The Areo SmallSat A and B elements then separate (Stop 1b) and utilize small propulsive maneuvers to drift to equidistantly spaced locations around the ring.
4. The Mothership uses SEP to carry the permanently attached upper ESPA ring accommodating the Polar and Elliptical smallsats during cruise.
5. After cruise and spiral-down to a $300 \times 6000 \text{ km} \times 93^\circ$ orbit, the Elliptical satellites separate (Stop 2) and use their onboard propulsion to change their inclination to 75° and lower periapsis to 150 km.

The Mothership continues its spiral to a 300 km, 3 p.m. LST Sun-synchronous orbit, at which point the Polar satellites separate (Stop 3) and change their inclination slightly. This allows them to drift to new ascending nodes (and LSTs), where they return to the Sun-synchronous inclination.

Scientific investigations may commence as soon as operational configuration and range allow. That is to say that some measurements may be taken during the spiral and/or drifting phases where desirable. Some elements will arrive at their respective science orbits up to many months before others. Each element may begin full operations when ready, but the baseline mission (two Mars years) commences when all elements are fully in place, allowing for co-temporal measurements and investigations needed to meet the scientific objectives.

3.3. Mission Timeline

Due to the nature of SEP-enabled low-thrust Earth–Mars transfers, launch dates are not rigidly confined to the standard 26-month ballistic transfer cycle used in most past Mars missions. Launches may occur at almost any time, but the optimal arrival time still roughly follows a 2 yr cycle. This

means that a launch slip of one year would likely result in a 2 yr delay in the arrival at the science orbit.

Figure 15 shows the phases and durations associated with a reference trajectory to Mars. Shortly after launch, the Mothership (carrying the Polar and Elliptical satellites) and the combined Areo platform group separate, using their respective SEP engines to thrust toward Mars. Many factors influence the duration of the cruise and spiral stages of each spacecraft, such as launch year, mass, power level, thruster choice, and trajectory optimization. The cruise phase lasts 16–24 months and is usually longer for areostationary platforms, mostly due to the length of the spiral-down phase to areostationary orbit. This allows both spacecraft clusters to arrive in their final orbits around the same time—approximately two years after launch.

The Elliptical and Polar spacecraft are deployed toward the end of the Mothership’s spiral phase. In the case of the Polar satellites, the only cost-effective way to shift their orbital planes is by taking advantage of the natural nodal drift induced by Mars’ gravity. This means that a 90° shift for one of the satellites could take up to 10 months (Figure 12). While this drift is occurring (the large purple bar in Figure 15), all of the satellites can continue to perform nominal science operations. Once all of the elements are in their final orbits (about three years after launch), the baseline mission begins and lasts for at least two Mars years.

4. MOSAIC Investigations: Measurements and Instruments

Each of the MOSAIC investigations is comprised of one or more sets of measurements, with associated requirements (e.g., cadence, resolution, accuracy, etc.). As part of the MOSAIC Science Definition effort, each measurement was assigned the following attributes (not all are applicable to all measurements):

1. The Measurement’s link to MOSAIC objectives.
2. Physical Parameter (PP) of the Mars climate system to be measured or estimated.
 - (a) PP name (e.g., dust opacity, temperature, ion flux, etc.).
 - (b) PP units (e.g., Kelvin).
 - (c) Expected PP range, i.e., minimum and maximum values.
 - (d) Coordinate system (e.g., IAU Mars, Mars–Solar–Orbital, etc.).

Table 1
Required Measurements for Investigation 1: Surface and Subsurface Ice

Measurement #	Instrument Type	Measured Quantity	Vertical Range	Horizontal Resolution	Frequency/Wavelength Range
ICE-1	Radar (<i>P</i> -band Polarimetric SAR)	Surface ice distribution over time	0 m	30 m	350–450 MHz
ICE-2a	Radar (<i>P</i> -band Polarimetric SAR)	Near-surface water content	0–3 m subsurface depth	30 m	350–450 MHz
ICE-2b	Radar (<i>P</i> -band Sounder)	Near-surface water content	1–15 m subsurface depth	1 km	350–450 MHz
ICE-3	Wide-angle imager (VIS)	Surface ice distribution over time	N/A	1 km	0.34–0.75 μm , 1.1–1.6 μm

- (e) Required range and resolution in altitude, latitude, and longitude with respect to which the parameter must be determined.
- (f) Required cadence with which the parameter must be determined.
- (g) Required seasonal resolution (how many times per season must it be measured?).
- 3. Observational Quantity (OQ) to be directly measured. For remote measurements where the PP must be derived/retrieved, the OQ is typically measured brightness or radiance at a specific wavelength or over a specific band of wavelength in the ultraviolet, visible, or infrared. For in situ instruments, e.g., magnetometers and particle analyzers, this is identical to the physical parameter.
 - (a) OQ name (e.g., intensity of radar power, thermal IR radiance, etc.).
 - (b) OQ units (e.g., Rayleighs).
 - (c) OQ dynamic range.
 - (d) Precision.
 - (e) Signal-to-noise ratio (S/N).
 - (f) Measurement cadence.
 - (g) Angular Field-of-View (FOV): range and resolution in both polar (θ) and azimuth (ϕ) angles.
 - (h) Required range and resolution of energy/wavelength/frequency of quantity being measured (e.g., particle energy, photon wavelength, radar frequency, etc.).
 - (i) Mass range (for instruments that measure particle mass).

These attributes are listed for each required measurement in Appendix A.2. The MOSAIC science team then identified instruments capable of making the measurements, carrying out a review to determine instrument performance metrics from (where possible) multiple potential providers and to compare with measurement requirements. For instruments likely to meet requirements, instrument TRL was assessed using standard NASA definitions. In cases where TRL was lower than 6, the time and cost were estimated to bring the instrument up to TRL 6. Instrument resources (power, mass, volume, data rate) were estimated for all potential flight instruments.

In this way, for each measurement, a prioritized list was compiled of one or more instruments that can meet each science requirement. Important instrument attributes were collected and tabulated:

1. Description and name.
2. Required platform.
3. Physical Parameter and Observable Quantity measured.
4. TRL (if <6, time and cost estimates to bring to TRL 5 and 6).
5. Field-of-view.
6. Mass.
7. Power.
8. Volume.
9. Accommodation Requirements, including thermal.
10. Measurement Range of wavelength/frequency/energy/field.
11. Resolution/number of channels.
12. Bits per sample.
13. Sample rate.
14. Threshold and Baseline data rate.
15. Phase A-D cost (\$FY20).
16. Potential providers.

In the following subsections, each investigation is briefly described in text and a table summarizing the required measurements is provided. Note that the column headings in these tables are neither exhaustive nor consistent across investigations, due to brevity and the need to focus on the important attributes of each measurement. For interested readers, detailed descriptions of each measurement requirement, as well as the instruments necessary for that investigation, are found in Appendices A.2–A.7.

Appendices A.8 and A.9 contain a comprehensive table of every measurement requirement and descriptions of the instruments required to make those measurements and their current heritage and TRL.

4.1. Investigation 1: Ice

“Determine the three-dimensional distribution of ice from the surface to 10 m below and its seasonal variability.”

Investigation 1 aims to greatly enhance our understanding of shallow subsurface ice on Mars (0–10 m depth) where this ice is exchanging with the atmosphere in the present day. Additionally, ice at these shallow depths is also the most easily accessible for future human exploration missions. GPR provides the best method to probe the subsurface globally, providing information on both water content and geologic composition. While this information is available at depths of tens to hundreds of meters from the Mars Express Mars Advanced Radar for Subsurface and Ionosphere Sounding (MARSIS) (Picardi et al. 2005; Seu et al. 2007) and Mars Reconnaissance Orbiter Shallow Radar (SHARAD), the

Table 2
Required Measurements for Investigation 2: Atmospheric Structure

Measurement	Measured Quantity	Vertical Range	Local Time	Precision	Horizontal Resolution	Vertical Resolution	Suggested Instrument
ATM-1	Temperature (K)	0–40 km	All	1 K near surface; 10 K near 40 km	60 km	<2 km	Radio science instrumentation (X-band)
ATM-2	Pressure (Pa)	0–40 km	All	2 Pa near surface, 0.6 Pa near 40 km	60 km	<2 km	Radio science instrumentation (X-band)
ATM-3	Temperature (K)	0–80 km	2–3 AM/PM	1 K	200 km	5–10 km	Thermal IR radiometer + submm spectrometer
ATM-4	Pressure (Pa)	0–80 km	2–3 AM/PM	5%	200 km	5–10 km	Thermal IR radiometer + submm spectrometer
ATM-5	Zonal and meridional wind speed (m s^{-1})	0–80 km	2–3 AM/PM	5 m s^{-1}	200 km	$\leq 10 \text{ km}$	Submm sounder + wind LIDAR
ATM-6	Dust opacity (km^{-1})	0–80 km	2–3 AM/PM	up to 1%	200 km	<5 km	Thermal IR radiometer + wind LIDAR
ATM-7	Water ice opacity (km^{-1})	0–80 km	2–3 AM/PM	up to 1%	200 km	<5 km	Thermal IR radiometer + wind LIDAR
ATM-8	Carbon dioxide ice opacity (km^{-1})	0–80 km	2–3 AM/PM	up to 1%	200 km	<5 km	Thermal IR radiometer + wind LIDAR
ATM-9	Water vapor mixing ratio (ppmv)	0–80 km	2–3 AM/PM	10 ppmv	200 km	5–10 km	Thermal IR radiometer + submm spectrometer
ATM-10	Temperature (K)	Surface	2–3 AM/PM	1 K	N/A	1 km	Thermal IR radiometer + submm spectrometer
ATM-11	Pressure (Pa)	Surface	2–3 PM	5%	N/A	2 km	NIR spectrometer

vertical resolution of these GPR instruments is insufficient to reveal the finer-scale structures of the upper 10 m. Radar can also provide information on surface geologic composition, particularly when paired with an optical imager with which to correlate measurements. A wide-angle optical imager will also allow for observations of the seasonal changes in surface ice extent (i.e., frost) and water ice clouds, carrying on the longstanding record of observations from the Mars Global Surveyor wide-angle Mars Orbiter Camera (MOC WA) and the Mars Reconnaissance Orbiter Mars Color Imager (MRO MARCI). All of these measurements together will help us understand how ice is interacting between the subsurface, surface, and atmosphere in the present day, as well as aid in the selection of future human landing sites where in situ resource utilization would be most achievable. Table 1 contains measurement requirements for Investigation 1.

4.2. Investigations 2 and 3: Lower-middle Climatology and Meteorology

“Measure the geographic and altitude distribution of pressure, winds, aerosol concentrations, water vapor, ozone, and temperature in the Mars lower and middle atmosphere (Investigation 2), and measure the complete diurnal, seasonal, and geographic behavior of the atmosphere and evolution of Martian dust and ice clouds (Investigation 3).”

MOSAIC would extend the climatology of atmospheric structure and dust storm activity at the detail provided by MRO to the duration necessary to support human exploration (>10 Mars Years). In addition, MOSAIC would provide critical and mostly unknown additional detail to this climatology in order to study the atmospheric circulation and movement of dust, water, and CO₂ through the Mars

system. These novel measurements would be of winds, aerosol profiles at mesoscale model resolution, and the full daytime cycle of dust storm activity and water ice clouds (including during the night). In addition, the robustness of MOSAIC lower-middle atmospheric measurements will be safeguarded by using complementary measurement techniques with variable sensitivity to aerosol opacity to enable sensing in the aphelion cloud belt, polar hood, and under dust storm conditions. In particular, synoptic temperature profiles and column-integrated measurements of dust, ice, and water vapor made by the areostationary platforms will be cross-calibrated with limb-measured altitude profiles of these quantities made from low circular near-polar orbits by the mothership and polar small satellites, ensuring a high and unprecedented level of confidence in the robustness of the data products. In most cases, the specific precision and dynamic range requirements are based on past climatological data sets. If otherwise, this is noted.

Investigations 2 and 3 are focused on climatology and meteorology, respectively. Investigation 2 is focused on extending and improving Mars climatology and can be accomplished by the mothership alone. Investigation 3, with its improved local time coverage and synoptic measurements, will enable Martian weather to be comprehensively characterized for the first time. At threshold, Investigation 3 requires three areostationary satellites to synoptically monitor weather systems, but the baseline mission, including the polar-orbiting smallsats, provides diurnal evolution of vertical profiles of aerosols and water vapor as well as important ground-truthing of the synoptic (areostationary) measurements at multiple local times. Tables 2 and 3 contain measurement requirements for Investigations 2 and 3, respectively.

Table 3
Required Measurements for Investigation 3: Atmospheric Diurnal Behavior

Measurement	Measured Quantity	Vertical Range	Local Time	Precision	Horizontal Resolution	Vertical Resolution	Suggested Instrument
DIU-1	Dust and ice cloud horizontal extent (km)	N/A	Daytime	N/A	<6 km	N/A	Visible camera
DIU-2	Dust and ice cloud duration (hr)	N/A	Daytime	N/A	<5 km	N/A	Visible camera
DIU-3	Temperature (K)	0-40 km	All	1 K	10 km	10 km	Thermal IR radiometer
DIU-4	Dust column opacity	N/A	All	<20%	<60 km	N/A	Thermal IR radiometer
DIU-5	Water ice column opacity	N/A	All	<20%	<60 km	N/A	Thermal IR radiometer
DIU-6	Carbon dioxide ice opacity	N/A	All	<20%	<60 km	N/A	Thermal IR radiometer
DIU-7	Surface pressure (Pa)	N/A	Daytime	5–10 Pa	<60 km	N/A	NIR spectrometer
DIU-8	Water vapor column (pr. μm)	N/A	All	<20%	<60 km	N/A	Thermal IR radiometer
DIU-9	Temperature (K)	0–80 km	As many as possible	1 K	<120 km	5 km	Thermal IR radiometer
DIU-10	Dust opacity (km^{-1})	0–80 km	As many as possible	Up to 1%	<120 km	<5 km	Thermal IR radiometer
DIU-11	Water ice opacity (km^{-1})	0–80 km	As many as possible	up to 1%	<120 km	<5 km	Thermal IR radiometer
DIU-12	Carbon dioxide ice opacity (km^{-1})	0–80 km	As many as possible	up to 1%	<120 km	<5 km	Thermal IR radiometer
DIU-13	Water vapor mixing ratio (ppmv)	0–80 km	As many as possible	10 ppmv	<120 km	5 km	Thermal IR radiometer
DIU-14	Temperature (K)	Surface	As many as possible	1 K	<1.2 km	N/A	Thermal IR radiometer
DIU-15	Zonal and meridional wind speed at cloud top + cloud structure and evolution	N/A	Daytime	10 m s^{-1}	<6 km	N/A	Visible imager
DIU-16	Pressure (Pa)	Surface	As many as possible in daytime	5%	N/A	2 km	NIR spectrometer

4.3. Investigation 4: Thermosphere

“Measure the global 3D composition, structure, and winds in Mars’ thermosphere, and its variability with season and solar activity.”

In line with MOSAIC Obj. I.C and II.C, Investigation 4 is focused on measuring the 3D structure of the thermospheric density, composition, temperature, and winds at Mars. This provides critical parameters to understand how the thermosphere is connected to the lower atmosphere (e.g., coupling via wave motions, changes in composition), as well as the ionosphere and exosphere (principally via changes in density and composition). In addition, this provides critically needed information on the thermospheric wind field, which remains a very poorly constrained parameter in models of this region. The global structure of the thermosphere is captured in four measurement requirements. All must be made from one of two instruments on a near-polar low-altitude (~ 300 km) circular orbiting platform to provide the geographic and local

time coverage requirements. Table 4 contains measurement requirements for Investigation 4.

4.4. Investigation 5: Ionosphere

“Measure the global 3D structure of Mars’ ionosphere, and its variability with season and solar activity.”

Investigation 5 is focused on measuring the spatial and temporal distribution of plasma in the ionosphere. This provides critical information to understand how the ionosphere is coupled with the lower/middle atmosphere, the thermosphere/exosphere within which it is embedded, and the space weather environment. In addition, this provides critically needed information on the potential of the ionosphere to disrupt radio navigation, positioning, and communications systems. The global structure of the ionosphere is captured in three measurement requirements (IONO-1, IONO-2, and IONO-3). Requirements IONO-1 and IONO-3 will be satisfied with spacecraft-spacecraft radio occultations. Requirement IONO-2

Table 4
Required Measurements for Investigation 4: Thermosphere

Measurement	Measured Quantity	Vertical Range	Local Time	Precision	Horizontal Resolution	Vertical Resolution	Suggested Instrument
THER-1	Neutral density of O, CO ₂ , NO	120–200 km	4 AM–8 PM (O, CO ₂) 10 PM–4 AM (NO)	25%	15°	5 km	MUV/FUV Spectrograph
THER-2	Temperature	80–150 km	4 AM–8 PM	10%	15°	2.5–5 km	MUV/FUV Spectrograph
THER-3	Horizontal winds	60–150 km	4 AM–8 PM	20 m s ^{−1}	15°	5 km	Doppler Interferometer

Table 5
Required Measurements for Investigation 5: Ionosphere

Measurement	Measured Quantity	Range	Vertical Range	Vertical resolution	Precision	Horizontal Resolution	Suggested Instrument
IONO-1	Electron density (remote)	0–10 ⁶ cm ^{−3}	80–200 km	5 km	2 × 10 ³ cm ^{−3}	10°	Spacecraft–spacecraft radio occultation
IONO-2	Electron density (in situ)	0–10 ⁵ cm ^{−3}	150–800 km	5 km	2 × 10 ² cm ^{−3}	15°	Langmuir probe
IONO-3	Electron density irregularities	>5 × 10 ² cm ^{−3}	100–200 km	>1 km	2 × 10 ² cm ^{−3}	N/A	Langmuir probe

Table 6
Measurement Requirements for Investigation 6: the Hydrogen and Oxygen Corona

Observable Quantity	Hydrogen Brightness	Oxygen Brightness
Wavelength	121.6 nm (Lyman α), 102.6 nm (Lyman β)	130.4 nm
Brightness	S/N 10 @ 250 R (121.6 nm) in <10 minutes S/N 3 @ 10 R (102.6 nm) in <10 minutes	S/N 3 @ 0.1 R in <10 minutes
Altitude Range	Disk center to 6 Mars radii	Disk center to 6 Mars radii
Cadence	Profiles or images at least weekly throughout the Mars year	Profiles or images at least weekly throughout the Mars year

Note. Observing these wavelengths with the required precision will enable retrieval of H and O densities and escape rates, allowing MOSAIC to tie loss rate variations to other changes in the Mars atmosphere system.

will be satisfied by in situ instruments on each elliptical spacecraft. Table 5 contains measurement requirements for Investigation 5.

4.5. Investigation 6: Exosphere and Neutral Escape

“Measure the 3D density and temperature structure of Mars’ hydrogen and oxygen exospheres.”

Variations in the Martian lower atmosphere and in the near-Mars space environment cause variations in the loss rate of hydrogen and oxygen from Mars to space. Past missions have measured these rates and placed some constraints on their variability with drivers, but MOSAIC’s monitoring of the atmospheric state along with new measurements of the exosphere will enable a more comprehensive understanding of Martian volatile loss than has thus far been possible. Simultaneous measurements of dust, middle atmospheric water, and upper atmospheric hydrogen will enable MOSAIC to determine the channels of Martian water loss to space today and enable confident extrapolation of contemporary loss processes into the distant past.

By measuring O loss as well as H, MOSAIC will place constraints on the redox evolution of the atmosphere, and enable a more complete understanding of the oxidation history of the planet. Table 6 contains measurement requirements for Investigation 6.

4.6. Investigation 7 and 8: Magnetosphere, Ion Escape, and Space Weather

Investigation 7 is focused on measuring the interaction of the solar wind with the electrodynamic obstacle consisting of Mars’ ionosphere and intense but localized crustal magnetic fields, which can dominate the magnetic environment (forming miniature magnetospheres) up to hundreds of kilometers above the surface. This interaction can accelerate planetary ions to escape velocity through a variety of mechanisms, and has been estimated to account for ~10% of the total oxygen loss (Jakosky et al. 2018). A simulation of ion escape is shown in Figure 7. The magnetosphere is highly variable because the crustal fields rotate with the planet and the upstream solar wind

Table 7
Measurement Requirements for Investigation 7

Measurement Number	Measured Quantity	Dynamic Range	Resolution	Energy or Frequency Range Resol.		Suggested Instrument
MAGN-1	Magnetic Field	1–3000 nT	0.3 nT or 10%	N/A	N/A	Fluxgate Mag.
MAGN-2, 3, 4	Electron Flux ²	10^4 – 10^{10}	10%	~1 eV to 10 keV	20% (dE/E , FWHM)	Electron Spectrometer
MAGN-5, 6, 7	Ion Flux ²	10^7 – 10^{10} ($dt = 16$ s) 10^4 – 10^8 ($dt = 10$ minutes)	10%	~1 eV to 20 keV	25% (dE/E , FWHM)	Ion Mass Spectrometer
MAGN-8	Ion Mass	1–44 amu	m/dm > 2	~1 eV to 20 keV	25% (dE/E , FWHM)	Ion Mass Spectrometer
MAGN-12	Electric Field	–300 to +300 mV m ^{–1} (DC) –100 to +100 mV m ^{–1} (AC)	1 mV m ^{–1} or 10%	DC–300kHz	N/A	Electric Field Experiment
MAGN-13	Electric Field Waves	10^{-4} – 10^2 mV m ^{–1} /√Hz	10^{-4} mV m ^{–1} /√Hz at 10 Hz	DC–300 kHz	N/A	Electric Field Experiment
MAGN-14	Magnetic Field Waves	10^{-4} –1 nT/√Hz	10^{-4} nT/√Hz at 10 Hz	1 Hz–4 kHz	N/A	Search Coil Magnetometer

Note. (1) Magnetosphere measurement requirements 9–11 are designed for upstream solar wind ions. They are identical to Space Weather measurement requirements 3–5 (see below) and so are not included here. During the MOSAIC mission design phase, solar wind measurements were moved to the Aereo platforms, so magnetosphere requirements 9–11 are no longer necessary for the elliptical platform. (2) Flux units are eV/(cm² s ster eV), which is proportional to count rate. (3) Measurement cadence is 16 s for EUV, ions, and electrons, 64 Hz for the magnetic field, 2 Hz for the electric field, and 100 Hz for electric and magnetic field time series (with onboard processing to measure higher-frequency waves and burst mode to control telemetry volume).

Table 8
Measurement Requirements for Investigation 8: Space Weather

Measurement Number	Measured Quantity	Dynamic Range	Resolution	Energy or Frequency Range Resol.		Suggested Instrument
SPA-1	Solar EUV	10^{-6} to 3×10^{-2} W m ^{–2} nm ^{–1}	15% (dI/I)	10–20 nm, 17–22 nm, 121–122 nm	N/A	Solar EUV monitor
SPA-2	Magnetic Field	~1–3000 nT	0.3 nT or 10%	N/A	N/A	Fluxgate Magnetometer
SPA-3, 4, 5	Ion Flux ¹	10^7 – 10^{10}	10%	~50 eV–10 keV	15% (dE/E , FWHM)	Ion Spectrometer
SPA-6, 7, 8	Electron Flux ¹	10^4 – 10^{10}	10%	~1 eV–10 keV	20% (dE/E , FWHM)	Electron Spectrometer
SPA-9, 10, 11	SEP Flux ¹	10 – 10^6	10%	50 keV–5 MeV (ions) 50 keV–1 MeV (elec.)	50% (dE/E , FWHM)	Solar Energetic Particle Detector

Note. Flux units are eV/(cm² s ster eV), which is proportional to count rate. Measurement cadence is 16 s for EUV, ions, and electrons, 64 Hz for the magnetic field, and 20 minutes for solar energetic particles.

conditions vary on a range of timescales. Investigation 7 is designed to determine the flow of energy and plasma throughout the magnetosphere by measuring from multiple viewpoints the fluxes of light and heavy ions, magnetic field and topology, plasma waves, and electric fields. Measurement requirements draw significantly on experience from previous Mars missions, most recently Mars Express and MAVEN. Thus, the ranges and variability timescales of most measured quantities are known, which allows us to draw on established instrument designs. Low-frequency (<16 Hz) plasma waves have been measured at Mars; however, a rich variety of wave phenomena are expected to occur at higher frequencies, based on analogy with Earth. MOSAIC

includes an electric field investigation and a search coil magnetometer to measure the full range of plasma wave modes. The wire booms of the electric field investigation require a spinning spacecraft, which drives the design of the Elliptical platforms, which are based on the THEMIS Mission (Harvey et al. 2008). The precessing elliptical orbit samples all local times, longitudes, and latitudes over the course of the primary mission. Resolving the ambiguity between variations in time and space requires at least two identically instrumented spacecraft, which has not yet been achieved at Mars.

Investigation 8 determines the driving solar wind conditions (including solar storms) and solar extreme ultraviolet irradiance.

		Baseline	Threshold	Partial	Marginal	None				
Mission Status	Missions & Instruments	Investigations:	1. Ice distribution	2. Atmosphere structure	3. Atm. Diurnal behavior	4. Thermosphere	5. Ionosphere	6. Exosphere, neutral escape	7. Plasma & ion escape	8. Space weather
Operational	Mars Reconnaissance Orbiter MCS & SHARAD (2006-									
	MAVEN PFP & IUVS (2014-									
	Trace Gas Orbiter NOMAD (2017-									
	Emirates Mars Mission EXI, EMUS, & EMIRS (2021-									
	China Tianwen-1 ion analyzer & magnetometer (2021-									
In Development	NASA ESCAPEDE (2026-									
	JAXA-ESA MMX MacrOmega, MSA (2025-2028)									
Concepts	Ice Mapper									
	COMPASS									

Figure 16. Potential contributions or backups to the MOSAIC constellation’s measurements from operational and planned scientific Mars missions. NOTE: measurements must be made simultaneously with MOSAIC.

Measuring the upstream solar wind conditions is achieved by placing a small plasma and fields instrument suite on two of the Areostationary platforms. At the areostationary altitude of $\sim 17,000$ km, this guarantees that at least one of these spacecraft will be in the upstream solar wind at all times. Since these platforms are three-axis stabilized, we use MAVEN-heritage designs for the particle instruments. Tables 7 and 8 contain measurement requirements for Investigation 7 and 8, respectively.

5. Practicalities and Paths Forward

The MOSAIC concept is indeed ambitious, yet little of lasting value is achieved without ambition. If we are to comprehend the global Martian climate system well enough to (a) understand the processes that drive its interconnections at a range of timescales and horizontal and vertical spatial scales and (b) keep human explorers safe, a substantial investment and commitment will be required. For both purposes, continuous, simultaneous, and global observations are indispensable, and can only be achieved by multiple platforms positioned in different orbits (i.e., a satellite constellation). This is an analogous requirement to monitoring the evolution of a hurricane on Earth, although the spatial scale of Mars’ meteorological phenomena can even reach planetary scale in case of extreme dust events. We would never rely on a satellite overpass every few days to understand a hurricane’s development, so why should a dust storm lifting center be any different? Put simply, a satellite constellation is critical to both extend our knowledge of Martian climate and to begin to truly understand Martian weather.

However, despite its ambitious scale, MOSAIC is a highly flexible and modular concept, both programmatically and scientifically. It is a commitment that does not have to be borne by a single funding agency (or division therein) or country, nor do all measurements necessarily have to be (a) made by as-yet unfunded missions or (b) collected synchronously (see Section 5.1). The following subsections discuss this flexibility and modularity, as well as potential management structures and the expected costs of combinations of those modular MOSAIC components, under reasonable assumptions.

5.1. Use of Existing and/or Planned Assets for Mosaic Measurements

Measurements of the Martian climate system made by instruments on other missions can certainly be of use, primarily in the form of providing context and/or preparation for MOSAIC’s measurements. However, if such measurements were to be made simultaneously with MOSAIC’s, they could help to fulfill pieces of MOSAIC’s investigations, to varying degrees, as shown in Figure 16.

MOSAIC is intended to continue, as well as improve, the sophistication of the climatological records of the lower and upper atmospheric state provided by currently operating spacecraft like Mars Odyssey, Mars Express, MRO, MAVEN, and ExoMars TGO. In some cases, MOSAIC would fly improved versions of instruments flown on existing missions, e.g., MCS on MRO. However, MOSAIC, in addition to making measurements from many more complementary vantage points, would reach Mars after the projected lifetimes of all of these spacecraft. The utility of these long-running spacecraft to MOSAIC lies mostly in generating (1) a preceding climatic record that MOSAIC will continue and (2) a knowledge base in raw data processing and data analysis that can be leveraged to speed the publication of data products and science results from MOSAIC data.

In addition, two orbiters are due to begin their science missions at the time of writing in early 2021. Each of these missions, if still operational at the time of MOSAIC’s arrival, could form either part of, or backups for, the MOSAIC constellation. The UAE Space Agency’s Emirates Mars Mission’s (EMM) “Al Amal” (Hope) orbiter arrived at Mars in 2021 February (Amiri et al. 2021). Its large, moderately elliptical, low-inclination orbit will allow frequent full-disk images of Mars in the thermal infrared, visible, and ultraviolet, allowing the diurnal behavior of Mars’ atmosphere to be characterized every 10 days, though without altitude information (except for temperature with coarse altitude resolution). While a significant advance with respect to the current state of knowledge, this would not replace MOSAIC’s continuous viewpoint from a minimum of three areostationary platforms. However, EMM’s Emirates Mars Ultraviolet Spectrograph (EMUS) is sufficiently similar in both design, perspective, and conops as to be an adequate

replacement for the FUV spectrograph (on the Areo Carrier platform) proposed for MOSAIC.

China's Tianwen-1 orbiter (Zou et al. 2021) carries a magnetometer and ion analyzer. Its orbit ($12,000 \text{ km} \times 265 \text{ km}$) will spend a significant amount of time outside the Martian bow shock, providing useful—though far from complete—space weather coverage.

Two more relevant Mars missions are in development. First, the ESCAPE mission (Lillis et al. 2019) would make the same type of multipoint coordinated plasma measurements of the MOSAIC elliptical orbiters, from 2026 onward. However, because ESCAPE's twin spacecraft do not spin, they cannot see the complete 4pi field of view and cannot measure electric fields (which require long wire antennae kept in place by spin). Second, the JAXA Mars Moon Explorer (MMX) mission will be in Mars orbit near the position of Phobos for three years from 2025 until 2028 (Kuramoto et al.). Though it was designed to study Mars' larger moon Phobos, during that time its Mass Spectrum Analyzer will measure the mass, energy, and direction of suprathermal ions, complementing the MOSAIC Elliptical orbiters' measurements of ion escape from Mars. Further, its MacrOmega near-infrared imaging spectrometer will study emissions from the lower atmosphere of Mars. However, MMX will not get closer than 6000 km from Mars—and hence, while complementary, its measurements will not substitute for MOSAIC measurements in any way.

Finally, there are various existing concepts for mapping subsurface ice at Mars. The COMPASS Discovery proposal (Byrne et al. 2020) and NASA's Ice Mapper concept (Watzin & Haltigin 2020) could both achieve most if not all of the goals of seasonal and interannual mapping of subsurface ice content. Importantly, these ice measurements would not necessarily need to be made simultaneously with the rest of MOSAIC's required measurements, as long as a full Martian year was observed, due to the much longer timescales associated with ice transport compared with atmospheric variability. Note that neither of these concepts has been selected for funding to date. Note also that both use an *L*-band radar that may not be as appropriate as the MOSAIC *P*-band radar and sounder, from the perspective of surface backscatter. Also, COMPASS would address many of the objectives of Investigation 2 (atmospheric structure) with its deployment of a thermal IR limb sounder, a submm limb sounder, and a wide-angle camera.

In summary, it is important to point out that, with the exception of the EMM EMUS instrument, none of these planned measurements fully replicate any of MOSAIC's required continuous simultaneous measurements, and should be seen as complementary observations and backup options with varying degrees of usefulness.

5.2. International Contributions

One key aspect of MOSAIC's flexibility and modularity is that it features six different platform types, which consist of one to three identical spacecraft with identical payloads. The need for multiple types of identical spacecraft and instruments can facilitate international cooperation in a mission of this size, allowing cost, risk, and credit to be shared among multiple space agencies.

Following a long tradition of cost sharing between space agencies on high-value science missions, we suggest two different ways in which the cost of making these important measurements may be spread more widely among the various

stakeholders. The first is the traditional route of contributed instruments from international or commercial partners on NASA-funded spacecraft buses. To ensure consistency of data and to leverage economies of scale, the same partner would contribute all required copies of a given instrument. An example here could be magnetometers contributed from the Danish Technical University (DTU) or the Technical University of Braunschweig (TUBS).

The second route would be for the partner to be responsible for all copies of a given type of platform, including design, build, test, payload integration, and operation. For example, the partner organization (e.g., ESA or JAXA) could provide all three of the low-circular polar orbiting SmallSats, though not necessarily its entire payload.

Compatibility testing would have to be conducted with other elements of the constellation if relay or radio occultation capability was required (as it would be in the SmallSat example). This second route implies that the overall coordination of the mission should be assigned to a single entity. The Mars Sample Return mission could constitute a valuable model for this type of cooperation.

The growth of commercial firms focusing on SmallSats has been an opportunity to spread involvement in space activities beyond traditional players in the Global North. We would like to highlight here the proposed visible imager for the areostationary platform, the South African Gecko Imager, as an example of an opportunity for space agencies in the Global North to collaborate with commercial entities, space agencies, and academic researchers in the Global South in planetary exploration and outreach.

5.3. Human Exploration and Commercial Contributions

Given that all but one of the eight investigations have relevance to MOSAIC's Goal II (Prepare for Human Exploration of Mars), it is reasonable to speculate that a significant portion of the MOSAIC constellation may be funded, or indeed provided by, entities actively engaged in preparation for human missions to Mars in the coming 10–20 yr. This would include NASA's Human Exploration and Operations Mission Directorate (HEOMD) and its international space agency partners, which have followed several lines of research and development into necessary technologies such as dust mitigation, in situ resource utilization, radiation shielding, life support, etc. This could also reasonably include commercial entities such as SpaceX and/or Blue Origin, who are interested in helping to establish reliable transportation to Mars for the purpose of establishing outposts and eventually cities there. In particular, these entities may be interested in helping to fund the areostationary parts of the constellation, which may be more appropriate for positioning and continuous communication with any longitude on the Martian surface.

5.4. Scientific and Programmatic Management

Most of the fuller incarnations of MOSAIC (see Section 5.6) are beyond the cost cap of PI-led missions, and so a directed-mission scientific structure is likely to be used, where authority is held by a project manager and not a scientist. Research has shown that, on such projects, particularly large flagship missions when each instrument's team has distinct, mostly nonoverlapping science goals and is separately responsible to

NASA, the science team does not always work well collaboratively (Vertesi 2020).

To avoid some of these pitfalls, and to fully recognize that while MOSAIC is a modular constellation, its science is not, we recommend a robust interdisciplinary science group. Observing the surface to upper atmosphere impacts of dust storms, or magnetosphere to surface impacts of solar storms, will require science and engineering team collaboration across instruments and across platforms in ways that go far beyond joint observational campaigns between operating missions at Mars today. A more free-flowing model of collaboration will be necessary, where representatives from different platforms and instruments are in regular contact. MOSAIC's focus on the weather suggests the new collaborative model could be partly anchored by a daily weather briefing, a common event in weather forecasting centers, departments of meteorology, at meteorological conferences, and during meteorological field campaigns (Birkenheuer 1987; Fabry et al. 1995; CIRA 2011). These briefings would help focus scientific effort on combining multiple perspectives to study weather systems and events rather than make climatological analyses of long individual instrumental data sets collected in the more or less distant past (e.g., Heavens et al. 2020). Experience from the space weather community suggests such briefings can be an important part of training forecasters in new forecasting domains (Steenburgh et al. 2014), perhaps presenting an opportunity to begin training weather and space weather forecasters to support human exploration activities. International collaboration might necessitate such a briefing being asynchronous.

Finally, to avoid some of the “turf issues” that have plagued previous planetary science missions, we would make two further recommendations. First, we recommend appointing a single lead scientist with final authority to make decisions in trades between the desires of different instrument teams in all scientific matters, and who therefore would not need to spend their time mediating the interests and personalities of each instrument team or lead, as is the case with many project scientists of large missions, who do not have such authority. Second, data from a given instrument would not be owned by that instrument team and would be required to be published at a regular cadence (e.g., once per month) after an appropriate initial data calibration and instrument check-out interval (e.g., six months).

5.5. Descope Options

While a true leap in our understanding of the interconnected Mars climate system requires the full MOSAIC constellation, there exist meaningful descope options that can perform subsets of the MOSAIC investigations, fully or partially, with associated decreased requirements on the number of spacecraft, payload mass and power, and cost. Indeed, another aspect of MOSAIC's modularity/flexibility concerns the degree to which its objectives can be met if some measurements are made asynchronously, incompletely, or not at all.

First, concerning asynchronicity, MOSAIC's mapping and seasonal monitoring of surface/subsurface ice would carry most of their scientific and exploration value, even if they were conducted in a different Mars year than the rest of the measurements, as long as the same ranges of Martian solar longitude (Ls) were covered by both sets of measurements. This is because we do not expect the subsurface ice (unlike the atmosphere) to vary significantly on subseasonal timescales

(although we could be surprised). Thus, our first considered descope concerns a situation where a different mission performs the surface and subsurface ice mapping. Indeed, NASA is actively considering such a mission, called Ice Mapper (Watzin & Haltigin 2020).

Second, concerning incomplete measurements, while simultaneous achievement of MOSAIC's four primary science objectives is required to comprehensively address its top-level science goal of understanding climate interconnections from the subsurface to the solar wind, there is still significant scientific value in partial fulfillment of the objectives, and particularly in completely fulfilling subsets of objectives. The remainder of our considered descope options involve progressively fewer spacecraft and/or instruments, with concomitant losses in scientific capability. Table 9 summarizes these descope options, which we discuss below. Note that no descope option contains more instruments or spacecraft than any option above it.

After the Ice Mapper case, “Descope 1” sacrifices Investigation 4 (Thermosphere) by eliminating both the Doppler Interferometer and FUV/MUV spectrograph, in addition to one of the lower atmospheric wind instruments (we assume losing the Wind LIDAR because it is significantly heavier than the submillimeter sounder), preserving valuable lower-middle atmosphere wind information and the remainder of the constellation.

“Descope Lite” has the same mini-mothership as Descope 1, but reduces the numbers of satellites and the rest of the constellation down to their thresholds. In particular, polar smallsats are reduced from three to two, thereby providing (along with the mini-mothership) atmospheric structure at only six local times instead of eight, with a resultant degradation in diurnal sampling. Elliptical plasma satellites are reduced from two to one, and the space weather package is included on only one of the areostationary satellites, preserving the ability to characterize real-time responses to space weather ~70% of the time, but losing the ability to characterize <4 hr time variability in ion escape or magnetospheric conditions in general. Finally, areostationary satellites are reduced from four to three, resulting in moderate but acceptable gaps in spatial coverage of the lower atmosphere. Importantly, this option still preserves all Investigations except 1 (ice) and 4 (thermosphere), though at a threshold level.

“Threshold Plus” is significantly simpler, eliminating the polar smallsats and elliptical plasma satellites completely, plus the EUV/FUV spectrograph and any relay capability for surface assets. This results in complete loss of Investigations 5 (ionosphere), 6 (exosphere and neutral escape) and 7 (magnetosphere), and partial loss of Investigation 3 (lower atmosphere diurnal behavior). It does nonetheless preserve (a) the unprecedented ability to characterize lower-middle atmosphere wind through the submillimeter sounder, (b) the global/diurnal perspective (though without vertical information except temperature) with 3 areostationary satellites, (c) the ability to “ground-truth” areostationary measurements of the atmosphere at two local times via the mini-mothership, and (d) the ability to monitor space weather.

“Threshold” represents the simplest version of MOSAIC that we would consider still worth implementing. It is simpler still, eliminating Investigation 8 (space weather) and any direct measurement of wind, a key part of Investigation 2 (lower atmosphere structure). It consists of (a) a very simple polar

Table 9
MOSAIC Descope Options

Platforms:	Mothership							Polar SmallSats	Elliptical SmallSats	Areostationary Satellites				Traditional Cost (Incl. Reserves.) FY25 \$M, 50% A-D, 25% E-F (30% A-D, 15% E-F)	Newspace Cost ^a (Incl. Reserves) FY25 \$M, 50% A-D, 25% E-F (30% A-D, 15% E-F)	Preserves	Loses
Instrument	P-band Radar	Wind LIDAR	Submm Sounder	Doppler Interferometer	FUV/MUV Spectrograph	TIR ^b radio-meter Visible Camera NIR Spectr.	Relay	Mini TIR Radiometer NIR Spectrometer	Radio Occultation —Includes Mothership	Magnetosphere Plasma Package	EUV/FUV Spectrograph	Space Weather Package	Mini TIR Radiometer viz. Camera NIR Spectr.				
Investigation	1	2	2	4	4	1,2		2, 3	3, 5	5, 7	6	8	3				
Baseline (in final report)	1	1	1	1	1	1	1	3	6	2	1	2	4	4,220 (3,719)	4,060 (3,581)	Full MOSAIC Capability	
Ice Mapper Case		1	1	1	1	1	1	3	6	2	1	2	4	3,436 (3,034)	3,277 (2,896)	Full top-to-bottom atmosphere sampling	Exchange of water with subsurface
Descope 1 (in final report)			1			1	1	3	6	2	1	2	4	3,073 (2,722)	2,910 (2,581)	Comprehensive lower atmosphere sampling	Above + Thermosphere + Winds except 10–80 km
Descope Lite			1			1 ^b	1	2	4	1	1	1	3	2,409 (2,212)	1,484 (1,364)	Adequate lower atmosphere sampling	Above + Full diurnal coverage + Ion escape short variability + Full space weather coverage
Threshold Plus			1			1 ^b						1	3	1,445 (1,332)	911 (841)	Global/diurnal perspective with winds and ground truth (i.e., side & top views of same atmosphere column)	Above + Boundary layer + Ionosphere + Magnetosphere + Exosphere & neutral escape
Threshold						1 ^b							3	1,023 (942)	620 (571)	Global/diurnal perspective plus ground truth	Above + Winds + Space Weather
Threshold Class D						1 ^b							3	561 (514)	376 (344) ^c	Global/diurnal perspective plus ground truth	Class B reliability

Notes.
^a Low end of triangular cost distribution from MOSAIC final report (Lillis et al. 2020).
^b TIR Radiometer could be AMCS (9 kg, 18 W) in higher cost cases or mini-MCS (3.5 kg, 8 W) in lower cost cases.
^c If SIMPLEX missions prove viable, Class D Tailored approach cost would likely be ~50% lower.

orbiting satellite with a visible camera, a small NIR spectrometer to collect surface pressure, and a small TIR spectrometer to measure atmospheric profiles of temperature, dust, ice, and water vapor, plus (b) three areostationary satellites with the same instruments (all looking nadir) to characterize surface pressure, coarse temperature profiles from the surface to 60 km, column dust and ice optical depth, and total column of water vapor. We consider this to still be scientifically useful because it will provide an unprecedented global/diurnal perspective of the Mars lower atmosphere, with crucial ground-truthing of areostationary measurement via the vertical profiles measured by the polar smallsat as mentioned in the previous paragraph.

5.6. Cost Analysis of Full and Descoped MOSAIC Architectures

All MOSAIC lifecycle cost estimates were performed by experienced cost estimators at JPL and benefit from many previous Mars Science orbiter studies as well as currently ongoing missions. Two different cost estimation methods were used: Traditional costing based on historical costs for Mars missions, and “Newspace” costing, accounting for recent significant cost decreases in reliable subsystems and launch vehicles due to the proliferation of smaller space companies and reusable launch vehicles. All instrument cost estimates were derived from the NASA Instrument Cost Model (NICM) based on objective inputs against cost estimation relationships of families of instrument types. Costs for the solar electric propulsion (SEP) system use analogy from the upcoming Psyche SEP system.

Only the Baseline and Descope 1 options were examined in detail for technical and financial feasibility by JPL’s Team-X and Team-Xc. Costs for the other Descope options (which were not independently investigated for technical feasibility) were estimated using regression and validated rules of thumb. The Baseline and Descope 1 options estimated the mothership with a Class A (flagship) and Class B designation, while both options assumed Class D (similar to the Small Explorers or “SMEX” class) single-string spacecraft. A separate estimate was made for each descoped option, with an additional “Class D only” cost estimate made for the Threshold mission, whereby all mission elements are single string. The result is more than an order-of-magnitude variation in cost estimates for MOSAIC, from \$376M for the Newspace estimate of the Class D Threshold mission with 30% reserves, up to \$4.2B for the Traditional estimate for the Baseline constellation with 50% reserves.

We contend that 50% reserves are unnecessary for MOSAIC. Although a 50% reserve estimate was required by NASA for this study, we believe that the high heritage and long cost history of Mars orbiters points to 30% reserves—or indeed less—as being more realistic. As a point of comparison, NASA’s last Mars orbiter (MAVEN) in 2013 was budgeted at \$671M (including 30% reserves) and cost \$583M, using just 13% of its allocated reserves (Dreier 2019). We believe this shows the low cost risk of Mars orbiter missions, due to their heritage.

As a final note on cost, NASA’s SIMPLEX program of low-cost planetary missions points to the possibility of costs significantly lower than even the \$376M estimate for the “Threshold Class D.” These missions are cost capped at \$55 million (excluding launch vehicle & DSN aperture costs)—and some, such as Janus (Scheeres et al. 2020) and ESCAPE

(Lillis et al. 2019), are going to deep space with two spacecraft. They are classified as “Class D Tailored” (SMD 2018), meaning that common off-the-shelf (COTS) parts are permitted and some aspects of typical NASA oversight are waived (e.g., fewer reviews, less documentation). Assuming that SIMPLEX missions prove viable (the first three are launching in a timeframe of 2022–24), then, under this Class D Tailored regime, the MOSAIC threshold would likely be in the ~\$150M range (not a JPL estimate).

Note that the cost information contained here is of a budgetary and planning nature and is intended for informational purposes only. It does not constitute a commitment on the part of JPL and/or Caltech.

6. Summary and Conclusions

In summary, the MOSAIC mission concept promises to revolutionize our understanding of the Mars climate system and of the physical processes that drive the connections within and between its major volatile reservoirs, from the shallow subsurface out to the solar wind. This improved understanding is motivated not only by scientific goals, but also is a necessary step in preparing to keep explorers safe as we plan for a sustained human presence on Mars. In addition, MOSAIC represents a major next step in planetary exploration, in at least three respects.

MOSAIC will be the first comprehensive examination of an extraterrestrial atmosphere, characterizing many atmospheric aspects for the first time, including surface–atmosphere interactions, boundary layer processes, wind structures, diurnal variability, mesoscale processes, and real-time response to space weather. In both the lower and upper atmospheres, MOSAIC will expand for the first time from the study of climatology to that of meteorology/weather. It will furthermore elucidate processes heretofore only hinted at, linking the lower and upper atmospheres and driving atmospheric escape and climate evolution.

Second, MOSAIC is the first in-depth study of a spacecraft constellation around another planet, helping to identify challenges in several key areas. These areas include (a) launch vehicle accommodation, (b) the timely delivery of the constellation of spacecraft to their respective science orbits, (c) operating and navigating the constellation safely, with up to four spacecraft in each of three different types of orbits, and (d) telecommunication architecture within the constellation to ensure adequate data volume is delivered back to Earth. Though this study did not allow sufficient time to explore the complete trade space of viable mission designs that meet measurement requirements, nor to mitigate all potential risks, the MOSAIC concept should serve as a starting point for future efforts to understand Martian weather and climate, prospect for water resources, and forecast hazards to future explorers.

Finally, MOSAIC will require collaboration and cooperation across multiple organizations, both scientifically and in terms of engineering and programmatics, as it is too ambitious to be funded entirely by any one division or directorate within NASA, with significant opportunities for cost sharing across space agencies and commercial entities. Indeed, its inherent flexibility and modularity is ideally suited to this kind of cooperation, with opportunities for interested parties to be responsible for multiple copies of an instrument and/or spacecraft platform type. We hope this concept can spur such multi-organization collaborations to begin in

earnest as the international framework for the human exploration of Mars is put in place over the coming decade.

We on the MOSAIC proposal team would like to thank the NASA Planetary Mission Concept Studies program for the opportunity to explore this ambitious and exciting idea, and to the Jet Propulsion Laboratory for their expertise and professionalism in developing this concept.

Work at the Jet Propulsion Laboratory, California Institute of Technology, is performed under contract with the National Aeronautics and Space Administration (80NM0018D0004).

We would also like to thank two anonymous reviewers for improving the content and clarity of the manuscript.

Appendix

A.1. Science Team Structure and Process

The MOSAIC science definition study took place from 2019 October until 2020 January and consisted of two main, connected efforts: (a) science measurement requirements definition and (b) instrument requirements definition. Due to the broad, multidisciplinary nature of the MOSAIC science purview, these efforts were conducted by seven different science working groups, as shown in Table 10.

These definition efforts mostly took place over email and biweekly teleconferences within each group, and by a Steering Committee consisting of the PI, Deputy PI, and group leads. The efforts culminated in a two-day Science Definition Team meeting at the UC Berkeley Space Sciences Laboratory on 2020 January 27–28, where the measurement and instrument requirements were discussed and solidified. These requirements were captured in the form of spreadsheets and quad charts that were provided to the study team at JPL for the conceptualization and point design efforts that followed.

A.2. Investigation 1 Requirements

A.2.1. Required Measurements: Subsurface and Surface Ice

ICE-1

Measurement ICE-1 requires using the surface polarimetric backscatter to determine surface geologic composition. The expected variation in polarimetric return spans the electrical properties of the target materials, from basaltic rock to clean water ice. The data products are a set of polarimetric SAR images containing information on returned power (in decibels) and phase for each polarimetric return (HH, HV, VH, and VV, with H and V standing for horizontal and vertical polarization, respectively). There are two measurement modes required: a high-rate mode for regions of interest (30°–60° latitude, at all longitudes, where potentially accessible near-surface ice has either been directly detected and/or inferred) at 30 m resolution, and a low-rate mode for other regions at 100 m resolution. The threshold measurement will be a seasonal low-rate mosaic from 30° poleward in each hemisphere. Beyond that, the baseline would include a full high-data-rate (higher-resolution) map mosaic twice per Mars year for the latitudes covered by the seasonal polar caps: 50° poleward at the beginning of spring and 80° poleward in mid-summer, to capture the maximum and minimum visible extent of each seasonal cap. High-rate nonpolar measurements at key areas of interest (e.g., the ice-bearing scalloped terrain of Utopia

Table 10
MOSAIC Science Definition Team, Divided into Working Groups

Principal Investigator	Robert Lillis	SSL, UC Berkeley
Deputy PI	David Mitchell	SSL, UC Berkeley
Subsurface & Surface Ice		
Lead	Tanya Harrison	Planet Federal Inc.
Co-lead	Cassie Stuurman	JPL
Members	Isaac Smith	PSI/University of York
	Gordon Osinski	U. Western Ontario
Lower & Middle Atmosphere		
Co-lead	Scott Guzewich	NASA GSFC
Co-lead	Luca Montabone	Space Science Institute
Members	Nick Heavens	Space Science Institute
	Armin Kleinbohl	JPL
	Leslie Tamppari	JPL
	David Kass	JPL
	Michael Mischna	JPL
	Michael Smith	NASA Goddard
	Michael Wolff	Space Science Institute
	Melinda Kahre	NASA Ames
	Aymeric Spiga	LMD, Paris
	François Forget	LMD, Paris
	Bruce Cantor	Malin Space Science Systems
Thermosphere		
Lead	Scott England	Virginia Tech
Members	Justin Deighan	LASP, University of Colorado
	Amanda Brecht	NASA Ames
	Steve Bougher	University of Michigan
Ionosphere		
Lead	Paul Withers	Boston University
Members	Robert Lillis	SSL, UC Berkeley
	Christopher Fowler	SSL, UC Berkeley
	David Andrews	IRF Uppsala, Sweden
	Martin Patzold	University of Koln
	Kerstin Peter	University of Koln
	Silvia Tellmann	University of Koln
	Mark Lester	University of Leicester
	Beatriz Sánchez-Cano	University of Leicester
Exosphere & Neutral Escape		
Lead	Michael Chaffin	LASP, University of Colorado
Co-lead	Justin Deighan	

Table 10
(Continued)

		LASP, University of Colorado
Magnetosphere, Ion Escape, and Space Weather		
Lead	Shannon Curry	SSL, UC Berkeley
Co-lead	David Mitchell	SSL, UC Berkeley
Members	Janet Luhmann	SSL, UC Berkeley
	Robert Lillis	SSL, UC Berkeley
	François Leblanc	LATMOS, Paris, France
	Jasper Halekas	University of Iowa
	David Brain	LASP, University of Colorado
	Xiaohua Fang	LASP, University of Colorado
	Jared Espley	NASA Goddard
	Hermann Opgenoorth	University of Umea, Sweden
	Oleg Vaisberg	IKI, Moscow, Russia
Radio Science		
Lead	Chi Ao	JPL
Members	Sami Asmar	JPL
	Josh Vander Hook	JPL
	David Hinson	SETI Institute
	Paul Withers	Boston University
	Ozgur Karatekin	Royal Observatory of Belgium

Planitia (Stuurman et al. 2016) would be acquired as needed. This measurement requirement is consistent with MOSAIC Obj. I.A.–II.A, and is essential for monitoring of surface changes due to volatile exchange with the atmosphere and for the characterization of potentially harvestable water ice resources for human exploration and ISRU.

ICE-2

Measurement ICE-2 requires detecting near-surface ice via measuring the subsurface moisture content and dielectric permittivity. There is an expected range in dielectric permittivity of ~ 1 –4 for Martian materials, depending on the geologic composition of the subsurface (Carter et al. 2009). The fully polarimetric SAR will measure the returned power in the channels HH, HV, VH, and VV (these denote the proportion of horizontal or vertical waves that are transmitted from the instrument versus received from the surface), which can then be used to calculate the bulk (i.e., not stratified) dielectric permittivity of the subsurface in the 0–3 m range. The horizontal resolution, cadence, and coverage requirements of the polarimetric SAR dielectric permittivity measurements are the same as ICE-1 in all cases, as it is simply a different data product from the same instrument.

The sounder will be used to determine the returned power (in decibels) of the subsurface in the 1–15 m range, as the

nearest-surface section will be obscured by surface scattering. This returned power can then be used to calculate the dielectric permittivity as a function of depth. The vertical resolution for the sounder measurements is 1.5 m in free space, corresponding to a 0.85 m resolution in clean water ice. The maximum expected signal-to-noise ratio for the raw data is 36.9 dB, but this decreases as the signal attenuates with depth. The threshold coverage requirement is a track density of 10 measurements per degree longitude between 30° and 60° latitude in both hemispheres over one Mars year. There is no minimum threshold coverage requirement equatorward of 30° latitude. Significant seasonal variations in the ice content of the Martian subsurface are not expected, and thus seasonally repeating measurements of dielectric permittivity are not required. This measurement requirement is consistent with MOSAIC Obj. I.A.–II.A and is essential for monitoring of surface changes due to volatile exchange with the atmosphere and for the characterization of potentially extractable water ice resources for ISRU required for human exploration.

ICE-3

Measurement requirement ICE-3 requires mapping the surface ice distribution over time. Changes in the seasonal components of the northern and southern polar caps have been well-documented by MOC WA (7.5 km resolution) and MARCI (1–10 km resolution) (e.g., James & Cantor 2001; Calvin et al. 2015). Active interannual changes have also been observed in the residual south polar layered deposits (e.g., Malin et al. 2001). Documenting these changes over time will help us to understand the exchange of ice between the surface and the atmosphere and to continue the longstanding record of observations from MOC WA and MARCI. This requires visible images of comparable resolution (~ 1 km) that can cover large swaths of the planet with daily near-global daytime coverage and visible-wavelength filters consistent with MARCI (400–750 nm). A 150° FOV at 300 km altitude allows for meeting this global coverage requirement via 14 images per day that each span from pole to pole on each orbit. This measurement requirement is consistent with MOSAIC Obj. I. A.–II.A, and is essential for monitoring of surface changes due to volatile exchange with the atmosphere and for the characterization of potentially extractable water ice resources for human exploration. The continued weather monitoring aspect is also important for future human habitation of Mars, in order to understand the spatial and temporal patterns of seasonal events such as dust storms and frost deposition, and how they may impact landing site selection.

A.2.2. Instruments: Subsurface and Surface Ice

P-band SAR + sounder (Mothership)

MOSAIC carries a fully polarimetric *P*-band combination SAR + sounder instrument on its mothership (Figure 17). The single, combined instrument uses a deployed 6 m dish antenna pointed either at 35° to the vertical (SAR) or nadir (sounder) depending on the measurement mode. The antenna is pointed by rotating the entire mothership platform. The majority of the SAR components are currently TRL 8–9, based on ESA’s Biomass instrument, and will be TRL 9 by the launch of Biomass in the early 2020s (Ramongassie et al. 2014). The sounder is TRL 9, based on NASA’s SHARAD on the Mars Reconnaissance Orbiter. The polarimetric SAR data product describes the power returned from the surface in the HH, HV, VH, and VV channels. The sounder data product is a radargram

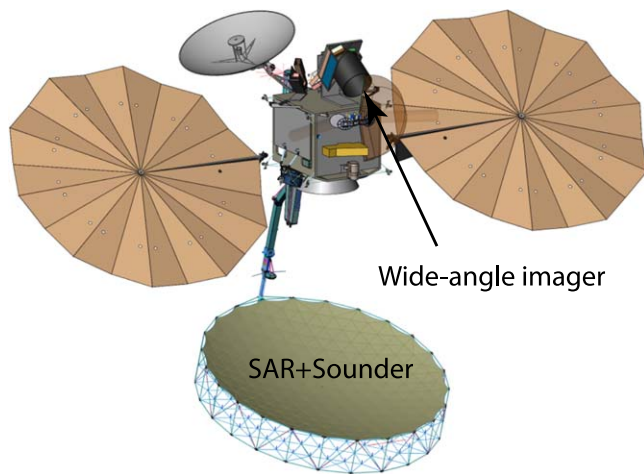


Figure 17. MOSAIC mothership with the SAR + sounder and wide-angle imager labeled.

(i.e., vertical radar profile) describing the returned power from the surface and subsurface (to maximum 15 m depth) at nadir. Threshold data rates are 2.3 Mbps for the sounder and 0.2–2.75 Mbps for the SAR, resulting from an onboard compression factor of 80–889. It has an expected mass of 90 kg and a maximum power of 500 W. For each measurement mode (sounder, SAR), there will be five measurements/sol. Measurements will begin one month after arrival. Because the sounder and SAR share an antenna, they will not operate at the same time.

Wide-angle imager (Mothership)

A wide-angle imager based on the design of the JHUAPL Mars Atmosphere, Volatile, and Resource Investigation Camera (MAVRIC; Byrne et al. 2020) was chosen to continue the multi-Mars-year record of surface ice (and weather) monitoring from MOC WA and MARCI. Expanding upon the range of these previous instruments, MAVRIC consists of six channels between 0.34 and 0.75 μm (UV+VIS) and an additional six channels between 1.1 and 1.6 μm (NIR). Similar to MARCI (Bell et al. 2009), images consist of a pole-to-pole swath with a 150° FOV in each band, passively building up near-global daily coverage in an always-on configuration on the dayside of the planet that allows for simultaneous operation with other instruments on board the mothership. The camera and electronics combined have a mass of 3.39 kg. While operating, it utilizes 2.1 W of power for the camera and 8.2 W for the electronics. Threshold data rates are 8.8 Gb/sol downlinked, with a collected orbit average of $\sim 102 \text{ Kb s}^{-1}$. Baseline data rates are 11 Gb/sol downlinked, with a collected orbit average of $\sim 127 \text{ Kb s}^{-1}$.

Thermal Infrared Radiometer

Since ice acts as a much better conductor of heat than dry Martian regolith, surface temperature measurements can be used to determine the thermophysical properties of the subsurface within $\sim 1 \text{ m}$ of the surface to identify the presence of shallow ice (Piqueux et al. 2019): Ice-rich terrain exhibits lower temperatures in spring/summer and higher temperatures in fall/winter, relative to ice-free regolith. The MOSAIC TIR (Section 4.2) will measure surface temperature (K) at a precision of 1 K over the full range of the Mars seasonal cycle and at local times near 2–3 AM/PM at a horizontal resolution of 1 km. These measurements will build upon the 7 km resolution multi-Mars-year measurements obtained by

Mars Climate Sounder (MCS) aboard the Mars Reconnaissance Orbiter, complementing the radar measurements to fill in our knowledge gap of the shallowest buried ice and how it may be changing over time. Instrument details may be found in Section A.3.2.

A.3. Investigation 2 and 3 Requirements

A.3.1. Required Measurements: Lower-middle Atmosphere Structure and Diurnal Behavior

Below, measurements with the prefix ATM pertain to Investigation 2, while the prefix DIU pertains to Investigation 3.

ATM-1 through ATM-4

Atmospheric temperature (K) and pressure (Pa) will be measured from the surface to 80 km altitude over the full range of the Mars seasonal cycle and at local times near 2–3 AM/PM at a vertical resolution of up to 2 km, a horizontal resolution of $\sim 60 \text{ km}$ (1° of latitude), and a precision in temperature of 1 K and in pressure of up to 0.5%. These measurements could be performed by radio occultation and thermal infrared spectrometric/radiometric sounding, but new techniques such as submm sounding would be necessary to fully satisfy the coverage, resolution, and validation criteria of the measurement requirements simultaneously.

ATM-5

Vertical profiles of zonal and meridional wind velocity (m s^{-1}) will be measured at a precision of 5 m s^{-1} from the surface to 80 km altitude over the full range of the Mars seasonal cycle and at local times near 2–3 AM/PM at a vertical resolution of $\leq 10 \text{ km}$ and a horizontal resolution of $\leq 300 \text{ km}$ (5° of latitude). These measurements can be performed by techniques never implemented before at Mars, such as submm sounding (sensitive to 10–80 km altitude) and Doppler shift measurements of lidar returns (sensitive to 0–40 km altitude). The use of both techniques would be necessary to meet the vertical range criterion of the measurement requirement.

ATM-6 through ATM-8

Vertical profiles of dust, water ice, and carbon dioxide ice opacity (km^{-1}) will be measured over a dynamic range of opacity equivalent to 10^{-6} – 10^{-1} km^{-1} at 1064 nm wavelength at a precision of up to 1% from the surface to 80 km altitude over the full range of the Mars seasonal cycle and at local times near 2–3 AM/PM at a vertical resolution of $< 5 \text{ km}$ and a horizontal resolution of $\sim 60 \text{ km}$. These measurements are most completely achieved by measuring atmospheric absorption and backscatter in lidar observations, but must be supplemented by near-infrared or thermal infrared passive remote sensing to fully satisfy the coverage, resolution, and validation criteria of the measurement requirements. The requirement to measure 10^{-1} km^{-1} opacity in the visible/near-infrared is equivalent to only 10–30 ppm of dust near the surface, which is significantly less than is observed in global dust storms (Heavens et al. 2019). However, this requirement is feasible for a lidar in the 1–2 μm spectral range. Nevertheless, it may be possible to retrieve up to 100 km^{-1} opacity from lidar measurements (Young et al. 2018), enabling the known dynamic range of dust mass mixing ratios to be observed. If opacities this high are not feasible to be retrieved robustly, the high vertical and horizontal resolution of the lidar will enable high-opacity regions within dust storms to be better isolated than previous

observations (Maattanen et al. 2009; Heavens et al. 2019), even if the lidar beam cannot backscatter from dust at the surface.

ATM-9

The vertical profile of water vapor will be measured over a dynamic range of 0–2000 ppmv at a precision of 10 ppmv from the surface to 80 km altitude over the full range of the Mars seasonal cycle and at local times near 2–3 AM/PM at a vertical resolution of <5 km and a horizontal resolution of <200 km. Measuring water vapor profiles at similar resolution and coverage to temperature and water ice opacity allows the thermodynamics of atmospheric water to be fully constrained and kinetic effects to be isolated. In conjunction with wind measurements, the transport of water around the planet can be directly calculated. The dynamic range is selected to be safely larger than the peak surface mixing ratio observed by the Phoenix lander, 1600 ppmv, at its northern high-latitude landing site (Fischer et al. 2019). These measurements can be done by thermal infrared or near-infrared spectroscopy/radiometry, and/or submm sounding.

ATM-10

Surface temperature (K) will be measured at a precision of 1 K over the full range of the Mars seasonal cycle and at local times near 2–3 AM/PM at a horizontal resolution of 1 km. These measurements are essential for monitoring of the atmospheric state, validating lower-resolution observations from areostationary orbit, and collection of/comparison with long-term climatologies. These measurements can be collected with a thermal infrared or submm spectrometer/radiometer, though using submm radiometry would be ideal to enable coverage in all conditions, particularly dust storms, while thermal infrared measurements would enable cross-validation with long-term climatologies.

ATM-11

Surface pressure (Pa) will be measured at a precision of 5% over the full range of the Mars seasonal cycle and at local times near 2–3 PM at a horizontal resolution of 2 km. These measurements are essential for monitoring of the atmospheric state and supporting/validating all vertical profile measurements. Surface pressure measurements can be done with a near-infrared spectrometer when the surface is illuminated.

DIU-1 through DIU-2

The extent and duration of dust and ice clouds will be measured from 80°S and 80°N at a spatial resolution of <5 km and temporal resolution of 30 minutes during the daytime across the Mars seasonal cycle and in as many large dust events as possible. These measurement requirements can be accomplished by UV or visible imaging from areostationary orbit.

DIU-3

Atmospheric temperature (K) will be measured from the surface to 40 km altitude at 10 km vertical resolution from 60°S to 60°N at a spatial resolution of <60 km and temporal resolution of 30 minutes throughout the course of a Mars day across the Mars seasonal cycle and in as many large dust events as possible. This measurement requirement can be accomplished by a thermal infrared radiometer from areostationary orbit.

DIU-4 through DIU-5

The column opacities of dust and water ice will be measured at 10%–20% precision over a dynamic range of 0–5 (optical depth), referenced to a wavelength of 1064 nm, from 60°S to 60°N at a spatial resolution of <60 km and temporal resolution of 30 minutes at most local times across the Mars seasonal

cycle and in as many large dust events as possible. This measurement requirement can be accomplished by near-infrared and thermal infrared spectrometers on areostationary orbiters.

DIU-6

The column opacity of CO₂ ice will be measured at 10%–20% precision over a dynamic range of 0–5 (optical depth), referenced to a wavelength of 1064 nm, from 60°S to 60°N at a spatial resolution of <60 km and temporal resolution of 30 minutes throughout the course of a Mars day across the Mars seasonal cycle. This is a best effort measurement for two reasons: (a) most polar CO₂ ice cloud activity is expected to be poleward of 60° (Neumann et al. 2003; Hayne et al. 2012) while the areostationary orbiters will not provide useful observations (i.e., those with emergence angles <70°) poleward of 60° latitude; and (b) opacity cannot be derived without a sufficient surface atmosphere contrast, which is often the case in the winter polar region.

DIU-7

Surface pressure (Pa) will be measured at 5–10 Pa precision over a dynamic range of 150–1500 Pa from 60°S to 60°N at a spatial resolution of <60 km and temporal resolution of 30 minutes throughout the course of a Mars day across the Mars seasonal cycle. This measurement is a best effort, because the necessary precision may be difficult to achieve in high dust conditions, when it would be most interesting to compare with aerosol cloud imagery. This measurement requirement can be accomplished by a near-infrared spectrometer on an areostationary orbiter.

DIU-8

Column water vapor (units of precipitable microns–pr. μm) will be measured at 10%–20% precision over a dynamic range of 5–400 pr. μm from 60°S to 60°N at a spatial resolution of <60 km and temporal resolution of 30 minutes throughout the course of a Mars day across the Mars seasonal cycle. This measurement is a best effort, because the necessary precision may be difficult to achieve in high dust conditions, when it would be most interesting to compare with aerosol cloud imagery. This measurement requirement can be accomplished by a near-infrared spectrometer on an areostationary orbiter.

DIU-9

Vertical profiles of atmospheric temperature (K) and pressure (Pa) will be measured from the surface to 80 km altitude over the full range of the Mars seasonal cycle and at as many local times other than 2–3 AM/PM as possible at a vertical resolution of up to 2 km, a horizontal resolution of 60–120 km, and a precision in temperature of 1 K and in pressure of up to 0.5% over 85°S–85°N.

These measurements can be executed by radio occultation and thermal infrared spectrometric/radiometric sounding on polar orbiters that cross the equator at different local times.

DIU-10 through DIU-12

Vertical profiles of dust, water ice, and carbon dioxide opacity (km^{-1}) will be measured over a dynamic range of 1×10^{-6} – $2 \times 10^{-2} \text{ km}^{-1}$ at 660 nm at a precision of 10%–20% over 85°S–85°N from the surface to 80 km altitude over the full range of the Mars seasonal cycle and as many local times other than 2–3 AM/PM as possible at a vertical resolution of 5 km and a horizontal resolution of 60–120 km.

These measurements can be executed by thermal infrared spectrometric/radiometric sounding on polar orbiters that cross the equator at different local times.

DIU-13

The vertical profile of water vapor (ppmv) will be measured over a dynamic range of 0–2000 ppmv at a precision of 10 ppmv over 85°S–85°N from the surface to 80 km altitude over the full range of the Mars seasonal cycle and at as many local times other than 2–3 AM/PM as possible at a vertical resolution of 5 km and a horizontal resolution of 60–120 km. Comparing with imagery, low vertical resolution temperature, and column measurements made under DIU-1 to DIU-9 would allow the relative roles of water vapor availability, temperature, and condensation nuclei availability (i.e., dust) in cloud formation and evolution to be studied. These measurements can be done by thermal infrared spectroscopy/radiometry on polar orbiters that cross the equator at different local times.

DIU-14

Surface temperature (K) will be measured at a precision of 1 K over 85°S–85°N over the full range of the Mars seasonal cycle and at as many local times other than 2–3 AM/PM as possible at a horizontal resolution of 1 km. As with other surface temperature measurements, these measurements can be used to measure the thermophysical properties of the subsurface within ~1 m of the surface, enabling the detection of shallow ice resources. These measurements can be done by thermal infrared spectroscopy/radiometry on polar orbiters that cross the equator at different local times.

DIU-15

Zonal and meridional winds (m s^{-1}) will be measured at a precision of $<10 \text{ m s}^{-1}$ wherever there are aerosol clouds or other features to be tracked. These measurements are essential for direct visual monitoring of the evolution of dust storms/water ice clouds/ CO_2 cloud evolution. They can also be used to reconstruct much of the global wind field, particularly its tidal component, at whatever level clouds are present. Imagery or image-like measurements with features trackable from measurement to measurement every 30 minutes are optimal to fulfill this measurement requirement. It should be noted that determining the altitude of the zonal and meridional winds, i.e., the altitude of the clouds used for tracking, can be achieved by leveraging vertical profiling information from investigations like ATM-6-ATM-8 and DIU-10-DIU-12.

DIU-16

Surface pressure (Pa) will be measured at a precision of 5% over the full range of the Mars seasonal cycle and at as many local times other than 2–3 AM/PM as possible at a horizontal resolution of 2 km.

Surface pressure measurements can be done when the surface is illuminated with near-infrared spectrometers on polar orbiters that cross the equator at different local times.

A.3.2. Instruments: Lower and Middle Atmosphere Structure and Diurnal Behavior

Radio Science Instrumentation (Mothership and Polar SmallSat, Elliptical)

Radio occultations (RO) can be performed among the different spacecraft in the MOSAIC constellation by leveraging the telecommunication systems on the spacecraft. RO instrumentation consists of a radio transponder, antenna, solid-state power amplifier, and an ultra-stable oscillator (USO). Precise measurement of the Doppler shift in the carrier tones transmitted from one spacecraft to another through the limb of the planet during ingress or egress condition can be used to retrieve vertical profiles of refractive index. Higher radio

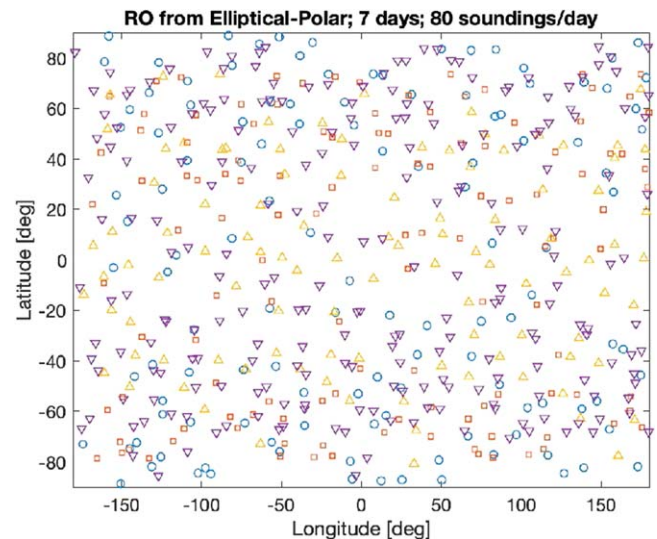


Figure 18. Radio occultation (RO) sounding distributions achievable over seven days between one elliptical orbiter and each of the four polar orbiters (each symbol type represents one polar orbiter). RO among the four polar orbiters themselves will add over 100 additional sounding profiles northward of ~60 deg. In contrast, RO from past orbiters can only provide 2–3 profiles per day on average, with limited coverage in latitude and local time constrained by Earth viewing geometry.

frequencies (e.g., X- or Ka-band) are preferred for sensing the lower atmosphere, while lower frequencies (e.g., UHF or S-band) are more sensitive to the ionosphere due to the fact that the refractivity in the ionosphere varies as the inverse frequency squared. Thus, dual-frequency RO measurements are baselined to simultaneously obtain both temperature, pressure, and geopotential height profiles in the lower atmosphere (~0–40 km) and electron density profiles in the ionosphere (~80–250 km), with high vertical resolution (~1 km) and ability to probe the Martian planetary boundary layer through dust and ice aerosols (Hinson et al. 1999). In contrast to traditional RO between a spacecraft and the Earth tracking station, RO between orbiting spacecraft provides a more uniform coverage over the planet and in all local times, similar to what has been achieved with GPS-RO for sensing the Earth’s atmosphere (Ho et al. 2020). For the MOSAIC constellation, RO between the polar orbiters will provide soundings with excellent coverage near the poles, while RO between the polar orbiters and the elliptical orbiter will provide good spatial and diurnal coverages at the lower latitudes. Figure 18 shows the spatial coverage theoretically achievable between one elliptical orbiter and four polar orbiters over seven days. This provides about 80 profiles per day, on average, compared to only 2–3 RO profiles per day from the Mars Global Surveyor (MGS). The Iris deep space radio transponder used on the MarCO CubeSats to demonstrate real-time relay during the EDL of the InSight probe (Klesh & Krajewski 2015) can be adapted to perform dual-frequency RO between the spacecraft, with an estimated mass of 3 kg (1.5 kg for Iris and 1.5 kg for the USO, not including antennas), using 15 W of power (average), and with a data rate of 20 kb s^{-1} .

Thermal IR radiometer (Mothership)

We require a thermal IR radiometer to profile temperature, pressure, dust, water and CO_2 ice, and water vapor in the lower and middle atmosphere (Kleinbohl et al. 2009), and to derive atmospherically corrected surface temperature (Piqueux et al. 2016). The radiometer is TRL 9, being nearly identical to the

Mars Climate Sounder (MCS) on board MRO (McCleese et al. 2007). Like MRO-MCS, the radiometer would observe surface and atmospheric emission from nadir and limb views, calibrated against views of space internal blackbody and solar reflection targets in nine spectral channels. Each channel would consist of a linear array of uncooled thermopile detectors, which instantaneously measures a radiance profile when vertically pointed at the limb. The main difference would be the modification of one of the far-infrared channels to allow the separation of aerosol and water vapor signals, enabling the accurate retrieval of water vapor profiles, which was not possible using MRO-MCS (Kleinböhl et al. 2016). MOSAIC-MCS would have a mass of 9 kg, use 18 W of power, and have a data rate of 4 kb s^{-1} .

Wind LIDAR (Mothership)

We have baselined the Mars lidar for global climate measurements from orbit (MARLI) direct-detection Doppler wind lidar, which is being developed at NASA GSFC under funding from the PICASSO and MATISSE programs (Cremons et al. 2020). A visualization of it is shown in Figure 19. It was scheduled to reach TRL 6 in 2020 June, prior to a suspension of work due to COVID-19. It consists of a 50 cm telescope and a 1064 nm laser that pulses at 250 Hz. The returned laser light passed through a Fabry–Perot etalon to discriminate the Doppler-shifted light that is backscattered by atmospheric dust and water ice aerosols. The receiver is sensitive to polarization, to discriminate between dust and water ice aerosols. Under normal atmospheric dust loading, MARLI is sensitive to the line-of-sight wind speed from the surface to $\sim 40 \text{ km}$ altitude at a precision of $\leq 4 \text{ m s}^{-1}$ at a vertical resolution of $\sim 2 \text{ km}$. Under high dust loading, MARLI is more sensitive (precision of $\leq 2 \text{ m s}^{-1}$) and can retrieve wind speed to higher altitudes. Aerosol extinction has 10% or less relative error. For MOSAIC, we have included a tilt table that would allow MARLI to retrieve the full wind vector. Including the tilt table, MARLI is 45 kg, uses 91 W of power, and has a data rate of $<100 \text{ kb s}^{-1}$ with a 90% duty cycle.

Submillimeter sounder (Mothership)

A submillimeter sounder, developed at JPL to TRL 5, is baselined to connect the lower atmospheric winds observed by the wind LIDAR to the upper atmospheric and thermospheric winds observed by the wind Doppler interferometer. It consists of two independently steerable receivers (see Figure 20), oriented orthogonally Craig qq and scanning between 12° and 32° below horizontal, to retrieve the full wind vector. The receivers have a 3 GHz bandwidth centered on 450 GHz to retrieve wind speed, water vapor, deuterated water vapor (HDO), and temperature profiles $\sim 10\text{--}80 \text{ km}$ altitude with 6–9 km vertical resolution for wind and 3–4 km vertical resolution for gas species and temperature. Precision is 15 m s^{-1} wind speed for a single profile, which is reduced to $5\text{--}10 \text{ m s}^{-1}$ with averaging, $<9 \text{ ppm}$ for water vapor below 50 km, $<0.1 \text{ ppm}$ for HDO below 50 km, and $<2 \text{ K}$ for temperature. Submillimeter observations are insensitive to atmospheric dust loading. The instrument is 35 kg. It uses 39 W on average, and 50 W at peak operation. Its baseline data rate is 40 kb s^{-1} .

Near IR spectrometer (Mothership, Areo Carrier, Areo SmallSats A/B, and Polar SmallSat)

Included in the threshold mission is a highly compact near-IR spectrometer known as Argus 2000 to measure surface pressure from low Mars and areostationary orbits. Argus 2000,

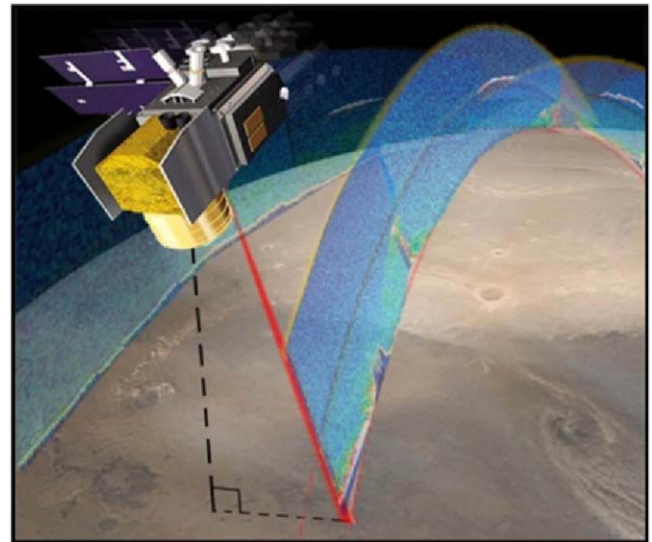


Figure 19. Visualization of the proposed wind LIDAR (MARLI) in operation. The lidar is pointed 30° off-nadir in the cross-track direction to help disambiguate between the zonal and meridional wind directions. The curtains of data illustrate the expected resolution of aerosol profiles from the instrument. Reproduced with permission from Cremons et al. (2020).

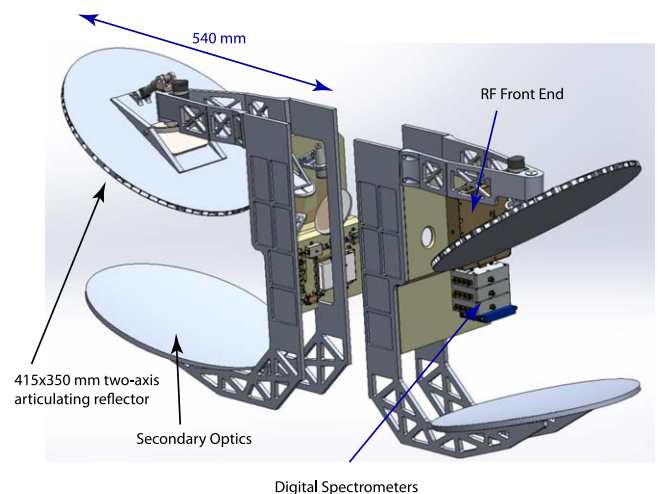


Figure 20. Design of a dual-antenna submm system. Each antenna scans 180° azimuthally, and the top antenna scans vertically for atmospheric profiling.

developed by Thoth Technologies (Canada) is TRL 9 with heritage from Argus 1000 (Rajinder et al. 2010), which flew on the CanX-2 nanosatellite mission in 2008. TRL may be rated lower because of the proposed use of the extended version of the spectrometer, which observes the NIR spectrum from 1000 to 2400 nm at 6 nm resolution to fully resolve the CO_2 band structure in reflected sunlight (see Figure 21) and collect the necessary information to correct for the effects of variability in surface albedo/composition and broadband aerosol absorption/scattering. From this information, column abundance of CO_2 then can be retrieved to obtain surface pressure (Toigo et al. 2013). Argus 2000 is a point spectrometer with an IFOV of 2.18 mrad, giving it a resolution of $<1 \text{ km}$ on the mothership and polar smallsat (excluding smearing during integration) and of $<40 \text{ km}$ from an areostationary orbit, where it may be slewed along with other instruments observing the disk. The instrument is 300 g, uses $<2.5 \text{ W}$ of power, and has a threshold

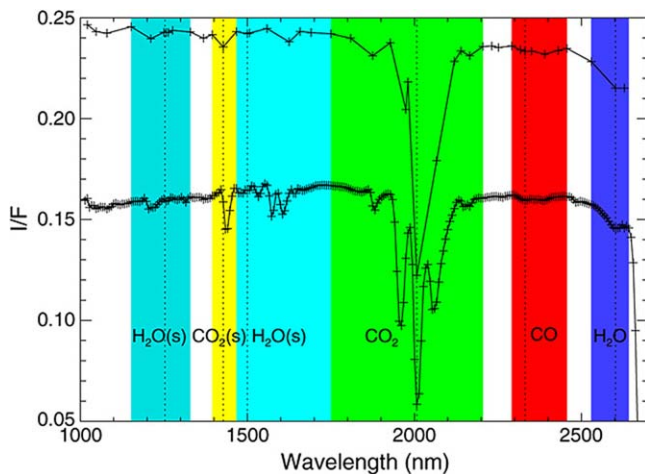


Figure 21. Sample NIR observation spectra from the Compact Reconnaissance Imaging Spectrometer (CRISM) on board the Mars Reconnaissance Orbiter (MRO), with absorption feature used by Toigo et al. (2013) to retrieve atmospheric gases and surface ices highlighted in different colors, as labeled. The lower-resolution observation (the top curve) has been shifted upward by 0.05, to be seen clearly. Each spectrum represents an average over an approximately 2 km square. MOSAIC's NIR spectrometer would focus on measuring the CO₂ absorption feature in green from both low Mars and areostationary orbit in order to retrieve CO₂ column abundance/surface pressure. Reproduced with permission from Toigo et al. (2013).

data rate of 1047 bps (assuming a high degree of onboard processing).

Visible camera (Areo Carrier and Areo SmallSat A/B)

Included in the Threshold mission is a highly compact, high-resolution, multispectral/hyperspectral imager known as Chameleon to observe from areostationary orbit the extent and duration of dust and ice clouds. Chameleon is TRL 6, with heritage from the SCS Aerospace Group Gecko Imager aboard the private South African nSight-1 satellite launched from the International Space Station in 2017 (Malan et al. 2017; Mhangara et al. 2020). Developed by Space Advisory Company (South Africa), Chameleon would be configured for MOSAIC to observe in panchromatic mode and eight multispectral channels to cover the typical visible/near-infrared range of past Mars weather cameras. It would have a lateral resolution of ~ 400 m in areostationary orbit, but with an FOV of $5^\circ.6$, it would need to be scanned to cover the Martian disk with ~ 14 nonoverlapping images. The instrument is 1.6 kg, uses <7 W of power, and has a baseline data rate of 30 Mbps, which could be significantly reduced by spatial and channel averaging and aerosol type identification during onboard processing.

Mini Thermal IR radiometer (Areo Carrier, Areo SmallSat A/B, and Polar SmallSats)

Also included in the threshold mission for the areostationary orbiters and the polar SmallSats is a miniaturized thermal IR filter radiometer to profile temperature and pressure; measure dust, water and CO₂ ice, and water vapor column opacity in the lower and middle atmosphere; and derive atmospherically corrected surface temperature. The radiometer is TRL 6, being a miniaturized version of the Mars Climate Sounder (MCS) on board MRO (McCleese et al. 2007), but designed to fit (including a mirror for pointing) into a 2U cubesat form factor. The subsystems have heritage from the Polar Radiant Energy in the Far-InfraRed Experiment (PREFIRE; Drouin & L'Ecuyer 2018) under development at JPL and scheduled for launch in 2021. The radiometer would observe surface and

atmospheric emission from approximately nadir views made by raster scanning across the disk with flip mirrors from areostationary orbit, or scan between limb, nadir, and space like MRO-MCS or MOSAIC-MCS from the polar SmallSat orbit. Note that disk scanning by MRO-MCS was demonstrated during MRO aerobraking (McCleese et al. 2007). These views would be regularly calibrated against views of space internal blackbody and solar reflection targets in nine spectral channels. Each channel would consist of a linear array of uncooled thermopile detectors with an individual detector resolution of ~ 60 km in areostationary orbit. The main difference from MRO-MCS (excluding miniaturization and adaptation to the areostationary platform) would be the modification of one of the far-infrared channels to allow the separation of aerosol and water vapor signals, enabling the accurate retrieval of water vapor profiles, which was not possible using MRO-MCS (Kleinböhl et al. 2016). MOSAIC-mini-MCS is expected to have a mass of 3.5 kg, use 8 W of power, and have a data rate of 4 kb s^{-1} .

A.4. Investigation 4 Requirements

A.4.1. Required Measurements: Thermosphere

THER-1

Measurement requirement THER-1 corresponds to atmospheric composition. The primary requirement is to measure CO₂ and O, with a secondary requirement to measure the recombination rate of atomic N and O to NO, over 120–200, 140–200, and 50–100 km altitude, respectively. The composition is needed to 25% precision, in 5 km altitude steps. These measurements are needed over the full range of Mars' seasonal cycle, covering all longitudes and latitudes to within 10° of the poles. Coarse longitudinal resolution of 30° and measurements covering the daylight local times are required.

The primary species in the thermosphere are CO₂ and O, and in addition NO is important for energy balance and is included as a secondary target. The varying altitude ranges correspond to the altitudes at which these species are significant components of the atmosphere, both in terms of density and energy. The altitude resolution provides information at one-third scale height needed to meaningfully track changes with altitude. The spatial coverage provides almost the entire globe, and coarse resolution is acceptable given the current state of knowledge and is sufficient to identify atmospheric tidal signatures.

THER-2

Measurement requirement THER-2 corresponds to atmospheric temperature from 80 to 150 km altitude in steps of 2.5–5 km, with a precision of 10%. These measurements are needed over the full range of Mars' seasonal cycle, covering all longitudes and latitudes to within 10° of the poles. Coarse longitudinal resolution of 30° and measurements covering the daylight local times are required.

Temperature is an essential measure of the energetics of the thermosphere. The altitude range requirement covers the region from the cold middle atmosphere up to the point where the thermosphere is essentially isothermal with altitude. The variable altitude resolution reflects the changes in scale height across this region and provides one-third scale height needed to meaningfully track changes with altitude. The spatial coverage provides almost the entire globe, and coarse resolution is acceptable given the current state of knowledge and is sufficient to identify atmospheric tidal signatures.

THER-3

Measurement requirement THER-4 corresponds to horizontal neutral winds, which are needed from 60 to 150 km altitude with a precision of 20 m s^{-1} , in 5 km altitude steps. These measurements are needed over the full range of Mars' seasonal cycle, covering all longitudes and latitudes to within 10° of the poles. Coarse longitudinal resolution of 30° and measurements covering the daylight local times are required.

There are extremely limited observations of winds in the thermosphere of Mars, and none fall within the altitude range where the middle and upper atmosphere meet. Knowledge of these winds is essential to understanding not only the dynamics of the upper atmosphere, but also its connection to the middle atmosphere. The altitude range of the measurements provides the connection to the middle atmosphere, and reaches up to the altitude at which models suggest the winds no longer vary significantly with altitude. The altitude resolution permits the capture of wind shears that may be present, e.g., in the lower thermosphere where the temperature begins to rise. The spatial coverage provides almost the entire globe, and coarse resolution is acceptable given the current state of knowledge and is sufficient to identify atmospheric tidal signatures.

A.4.2. Instruments: Thermosphere

Wind Doppler interferometer (Mothership)

The wind Doppler interferometer makes measurements of the horizontal winds from 60 to 150 km during daytime. It consists of two identical units, each of which measures the line-of-sight Doppler shift of both 557.7 nm and 1.27 μm airglow lines. This allows altitude profiles of the winds in the thermosphere to be measured in addition to the wind field just below, so that coupling between the lower and upper atmosphere can be quantified. As each measurement of the Doppler shift provides simply a component of the horizontal wind, two measurements of the same volume with lines of sight close to 90° apart are required. The two lines of sight are mounted at 45° and 135° to the spacecraft ram direction, allowing both components of the horizontal wind to be obtained on the limb. All altitudes are measured simultaneously, limiting moving parts. The two units together have a mass of 40 kg, require 13 W of power, and produce an orbit-averaged data rate of 14 kbps. To use the measurements of the line-of-sight Doppler shift to infer winds, precise knowledge of the spacecraft pointing is needed, in addition to pointing control that maintains the limb view in the correct orientation. Measurements are made at all points on the dayside, with at least one measurement every 2° of travel of the spacecraft.

The heritage instrument for the wind Doppler interferometer is the Michelson Interferometer for Global High-Resolution Thermospheric Imaging (MIGHTI) on board NASA's Ionospheric Connection Explorer (Immel et al. 2017). This measures the winds in Earth's thermosphere, using the same 557.7 nm airglow emission for MOSAIC, in addition to red airglow emission at 630.0 nm, which is replaced by the near-IR emission for MOSAIC. Just as with the instrument for MOSAIC, this measures the Doppler shift of both of these emissions across the whole altitude range with each exposure. The optical design for MIGHTI is shown in Figure 22 and is described in Englert et al. (2017). Of note is the long baffle (between the front aperture AB and Aperture A1), which ensures that light reflecting from either the solid surface or clouds is not seen by the instrument. The interferometer is a

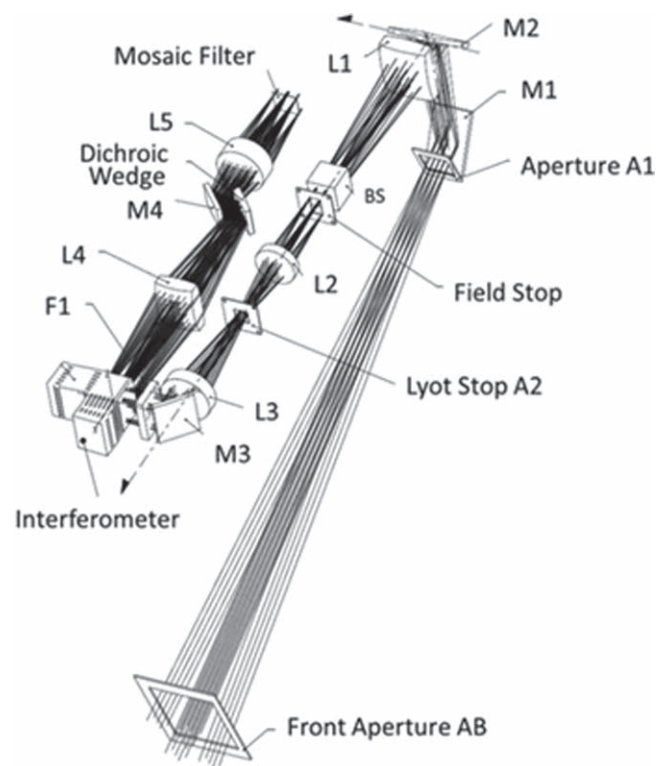


Figure 22. Optical layout of the MIGHTI Doppler wind interferometer. The entrance baffle ensures light from the solid planet or cloud tops does not reach the detector. Mirrors such as M1, M2, and M3 provide a relatively compact layout. The interferometer produces the interference pattern, allowing the Doppler shift of the airglow to be measured. The dichroic wedge separates the two airglow wavelengths, and the final mosaic filter rejects any other out-of-band light. After Englert et al. (2017).

monolithic design that requires no moving parts (Harlander et al. 2017). The dichroic wedge positioned after the interferometer projects the two wavelengths onto different halves of the detector, allowing a single CCD to record the interferogram for both wavelengths and all tangent altitudes seen. Finally, the mosaic (not to be confused with the acronym for this mission concept) filter selects wavelengths close to the two airglow features the instrument must measure.

FUV/MUV spectrograph (Mothership)

The FUV-MUV spectrograph measures a number of emissions from CO_2 , O on the limb during daytime, and NO during nighttime, over an altitude range spanning 50–250 km. A single unit is limb-mounted and requires sufficient attitude control to maintain its limb pointing. The instrument can either image the entire limb at once or employ a scan mirror to sample all these altitudes. The instrument mass is 15–27 kg, and power is 15–28 W for the imaging/scanning variants, respectively. The orbit-averaged data rate is 13 kbps. The instrument places stringent contamination controls, and possibly some materials selection restrictions on the rest of the spacecraft, as the optics can be damaged by organic and volatile compounds. Some heritage instruments have required continuous N_2 purging while in air.

The heritage instrument for the FUV/MUV spectrometer is the IUVS instrument on MAVEN (McClintock et al. 2015), shown in Figure 23. The instrument measures both wavelength ranges simultaneously on a pair of detectors. Using these, it is able to measure both the dayglow related to CO_2 and O (Evans



Figure 23. MAVEN IUVS instrument, described in McClintock et al. (2015). Covers over the two apertures are in place in this photograph, with one shown on the left of the image.

et al. 2015), and the nightglow related to NO (Bertaux et al. 2005; Stiepen et al. 2017).

A.5. Investigation 5 Requirements

A.5.1. Required Measurements: Ionosphere

IONO-1

Measure electron density in the range $0\text{--}10^6\text{ cm}^{-3}$ with uncertainty $<2 \times 10^3\text{ cm}^{-3}$ over altitude range 80–250 km with 1–2 km vertical resolution at a rate of 150 profiles per day for one Mars year, where each day's profiles are widely geographically dispersed.

IONO-2

Measure electron density in the range $10^2\text{--}10^5\text{ cm}^{-3}$ with uncertainty $<10^2\text{ cm}^{-3}$ over altitude range 150–800 km with 0.5 second temporal resolution at a rate of 20 profiles per day for one Mars year, where each day's profiles are widely geographically dispersed.

IONO-3

Search for electron density irregularities between 100 and 200 km altitude with length scale > 1 km and magnitude $> 5 \times 10^2\text{ cm}^{-3}$, with 1–2 km vertical resolution at a rate of 150 profiles per day for one Mars year, where each day's profiles are widely geographically dispersed.

A.5.2. Instruments: Ionosphere Smallsat Langmuir Probe

An instrument suite consisting of a variety of Langmuir probe implementations satisfies requirement IONO-2: a multi-needle Langmuir probe, two planar ion probes, and a floating potential probe, on board each elliptical spacecraft. This multisensor package is being developed for the ESCAPEDE mission (Lillis et al. 2019) and is currently TRL 6. It is designed to not exacerbate spacecraft charging issues commonly seen on small spacecraft with sweeping-voltage

Langmuir probes. The instrument suite's plasma density measurements will span $50\text{--}200,000\text{ cm}^{-3}$, with an accuracy of 50% at the lower end and better than 10% at the higher end. Its total estimated mass and power are 0.5 kg and 1.5 W, respectively, both within $\pm 20\%$.

The multi-needle Langmuir probe (mNLP) measures absolute electron density and consists of four gold-plated needle Langmuir probes (<10 g each) biased at different positive potentials (5, 6, 7, and 9 V). It needs to be mounted on a boom at least 0.5 m from the spacecraft. Power consumption is <1 W, while orbit-average data rate would be <10 bits per second. Two planar ion probes (PIPs) measure absolute ion density below 250 km, serving as a calibration for total electron density (Barjatya & Merritt 2018). They are flat-plate ($10\text{ cm} \times 10\text{ cm}$) Langmuir probes (<15 g each) biased negatively in the ion saturation regime, mounted on orthogonal sides of the spacecraft. Power consumption is <0.4 W, while orbit average data rate would be 12.5 bits per second. The floating potential probe (FPP) measures relative changes in spacecraft potential, critical to assess whether the PIP and mNLP sensors are operating in their expected regimes. It is a small, one-inch, gold-plated sphere (100 g) on a short, 10 cm boom isolated from the spacecraft chassis ground. Power consumption is <0.1 W. All three sensors' electronics are embedded on a single circuit board ($\sim 100\text{ cm}^2$) sharing the same rad-hard A/D converters and microprocessor.

Radio Occultation

As well as measuring neutral densities and temperatures (Section 4.6), the radio occultation experiment would make measurements of electron density (requirement IONO-1) and electron density irregularities (requirement IONO-3). It would conduct spacecraft-to-spacecraft radio occultations between the Mothership, Polar spacecraft, and Elliptical spacecraft. Observations would be acquired by transmitting a carrier-only radio signal from one spacecraft to another at times when one spacecraft is entering into/emerging from occultation behind Mars from the perspective of the other spacecraft. The instrument would make use of spacecraft communications systems, but would also require a dedicated transponder. For small spacecraft, the strawman transponder would be the JPL IRIS transponder. For the larger mothership, the strawman transponder would be the JPL universal Space Transponder (UST). For this application, both transponders are judged to be TRL > 6 . The IRIS transponder has a mass of 1.45 kg, power consumption of <33 W, and volume of $10\text{ cm} \times 10\text{ cm} \times 5\text{ cm}$. The antenna boresight would be steerable in a range of $\pm 60^\circ$ in azimuth and $\pm 10^\circ$ in elevation about the velocity and antiveloccity directions. A 1.5 kg ultra-stable oscillator would also be required. The experiment would operate in UHF, L, or S band, with dual-frequency observations preferred. Each sample of data would contain 16 bits, 8 bits for the I component of the radio signal and 8 bits for the Q component of the radio signal. The sampling rate would be 1 kHz for the electron density measurements (requirement IONO-1) and 1 Hz for the scintillation measurements of irregularities (requirement IONO-3). The orbit-averaged data rate would be 11 kbps. Onboard data processing might be able to reduce this data rate significantly. Importantly, this operation has already been demonstrated at Mars between the Odyssey and Mars Reconnaissance Orbiter spacecraft (Ao et al. 2015). A cartoon demonstrating spacecraft-spacecraft radio occultation is shown in Figure 24.

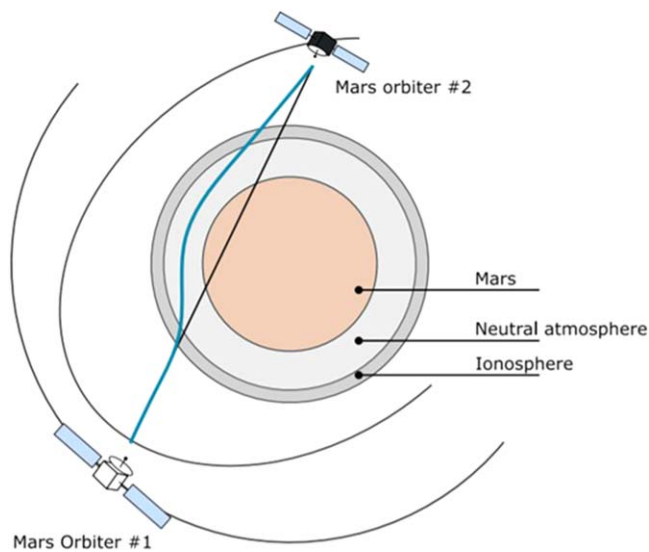


Figure 24. Schematic illustration of a spacecraft-spacecraft radio occultation. Refraction in the ionosphere and neutral atmosphere cause the ray path to bend slightly from the direct path between the spacecraft, which introduces a measurable frequency shift into the radio signal. Image from Tellmann et al. (2013).

A.6. Investigation 6: Exosphere and Neutral Escape

A.6.1. Required Measurements: Exosphere and Neutral Escape

EXO-1

EXO-1 lays out rough requirements for the measurement of hydrogen and oxygen escaping from the planet. Because direct detection of escaping neutral H and O at thermal energies is not feasible, the definitive technique for constraining this loss is measurement of ultraviolet light scattered by escaping and bound H and O atoms in the corona. While measurements of this brightness have been made since the early Mariner missions (e.g., (Anderson & Hord 1971), reliable uncertainty analysis has only recently become computationally feasible (Chaffin et al. 2018). For this reason, the physical parameter retrieved (H and O escape rate) has relatively large uncertainty bounds when compared to other MOSAIC parameters. Nevertheless, the data we require as inputs to the retrieval are well-known: we require UV images of the planet at Ly α (121.6 nm), Oxygen 130.4 nm, and perhaps Lyman beta (102.6 nm) wavelengths, covering the disk and inner corona to ~ 6 Mars radii, as shown in Figure 25. On the limb and disk, the spatial/altitude resolution of these measurements must be on the order of 15 km, the neutral atmospheric scale height, to resolve the thermospheric H profile and distinguish impulsive proton aurora from neutral H (Deighan et al. 2018; Ritter et al. 2018; Hughes et al. 2019). To constrain known spatial variability (e.g., Chaffin et al. 2015; Chaufray et al. 2015; Bhattacharyya et al. 2020), such images should be gathered from four to six vantage points around the satellite orbit, including images from near the subsolar point, as well as the dawn and dusk terminators, with coverage of the nightside as Ly α light is multiply scattered around the planet and illuminates even midnight. The measurement time cadence is set by the regular seasonal variability of H loss (Chaffin et al. 2014; Clarke et al. 2014; Halekas 2017), impulsive responses to dust events (Chaffin et al. 2019), and short-timescale variability of the thermospheric inventory caused by solar impulsive events

(Mayyasi et al. 2018), requiring a measurement cadence of at most several days to a week, in which all images must be gathered. By comparison with H, the O emission and retrieval are relatively straightforward and rely on optically thin radiative transfer coupled to an ionosphere/thermosphere escape model (Deighan et al. 2015). Generic measurement requirements are summarized in Table 6.

A.6.2. Instruments: Exosphere and Neutral Escape

An FUV spectrograph mounted on an areostationary platform is sufficient to fulfill the measurement requirements for the exosphere investigation. Such a spectrograph produces a spectral image, recording brightness as a function of wavelength along a 1D slit typically 10° in length. To build 2D images, the instrument requires spacecraft pointing along at least one axis, which can be combined with an internal scan mirror to reduce the amount of spacecraft pointing required. Combined motion from the spacecraft is required to raster the slit across the planet to high altitude in order to build an image from the 1D slit.

An FUV spectrograph typically measures wavelength ranges of ~ 110 – 170 nm, with an optional extension to lower wavelengths enabling measurement of Lyman beta and higher fidelity in the escape rate measurement, at the cost of added complexity in instrument and detector design, because measuring wavelengths less than 110 nm requires specialized detectors that cannot be exposed to water or oxygen.

These spectrographs are TRL 9 with extensive design heritage, having flown in space since the early Mariner missions. Contemporary examples include MAVEN/IUVS (McClintock et al. 2015) shown in Figure 23, Rosetta/Alice (Stern et al. 2007), EMUS on the Emirates Mars Mission (Holsclaw et al. 2021), and many others. Based on MAVEN/IUVS, these spectrographs as built by LASP have typically weighed ~ 20 kg and consumed ~ 20 W of power. Data rates are highly configurable, given the many onboard options for binning and reducing the data, but we estimate for MOSAIC that the typical data rate will be ~ 2 Gbit/week, with a threshold rate $4\times$ lower.

A.7. Investigation 7 and 8: Magnetosphere, Ion Escape, and Space Weather

A.7.1. Required Measurements: Magnetosphere, Ion Escape, and Space Weather

MAGN-01

Vector magnetic field: Measure the vector magnetic field from ~ 1 to 3000 nT with a sensitivity of 0.3 nT or 10%, whichever is larger, throughout the Mars environment. The magnetic field is essential for interpreting charged particle measurements. The magnetic field configuration and its topology (in conjunction with suprathermal electron measurements) are crucial for understanding the motion (and escape) of charged particles in the Mars environment. The wide dynamic range is needed to measure the solar wind field upstream of the bow shock as well as strong crustal magnetic fields near periapsis. The accuracy on the amplitude is primarily needed to constrain the magnetic field direction when the amplitude is small.

MAGN-02

Suprathermal electron flux: Suprathermal electrons, consisting of ionospheric primary photoelectrons, upstream and shocked solar wind electrons, and accelerated electrons in the induced magnetotail and crustal magnetic cusp regions span a wide range of fluxes.

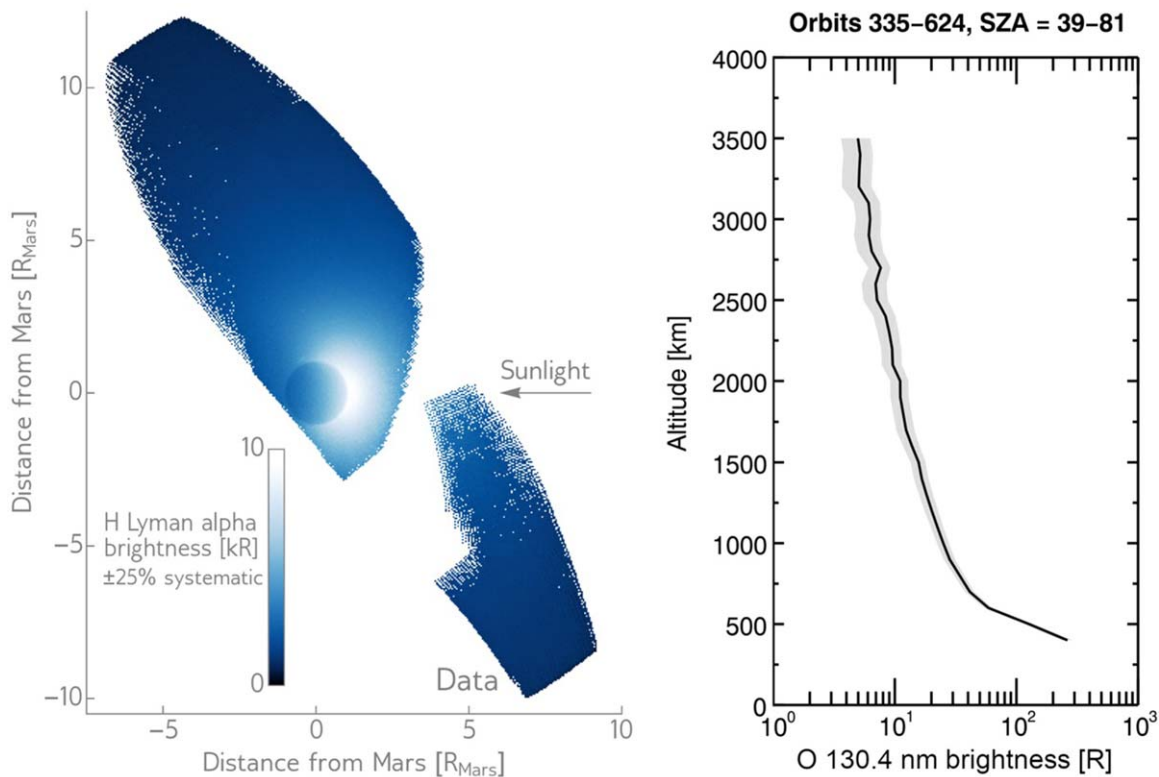


Figure 25. Observations of the Mars hydrogen and oxygen corona from MAVEN IUVS. (Left) H Ly α (121.6 nm) observations from MAVEN’s insertion orbit, as presented in Chaffin et al. (2015). (Right) Observations of the thermal and hot oxygen corona as presented by Deighan et al. (2015). Observations of the extended corona such as these can constrain the H and O loss rates from Mars, and by extension the volatile loss history of the planet.

The lowest fluxes ($<1\text{e}4\text{ eV cm}^{-2}\text{ s ster eV}$) are observed within “suprathermal electron voids” that occur on closed crustal magnetic field lines on the night hemisphere. The highest fluxes ($>\sim 1\text{e}9\text{ eV cm}^{-2}\text{ s ster eV}$) are observed just downstream of the bow shock and during energized precipitation (auroral) events in crustal magnetic field cusps.

MAGN-03

Suprathermal electron energy: Ionospheric primary photoelectrons span the energy range from $\sim 1\text{ eV}$ to $\sim 500\text{ eV}$, with diagnostic features at 7 eV (corresponding to a minimum in the electron–neutral collision cross section), $22\text{--}24\text{ eV}$ (corresponding to photoelectrons produced by the intense solar He-II line at 304 nm), and 500 eV (corresponding to oxygen Auger electrons). Solar wind electrons, consisting of core and halo populations, extend from a few eV to $\sim 1\text{ keV}$. Shocked magnetosheath electrons are energized but typically span a similar energy range. Higher-energy electrons are occasionally produced by solar storms (CMEs, solar flares, and interplanetary shocks).

MAGN-04

Suprathermal electron angular distribution: Electrons in the solar wind and throughout the Mars environment have thermal velocities that are much larger than their bulk velocities (or spacecraft orbital velocities). Thus, electrons are incident from all directions. The electron angular distribution has anisotropies with respect to the magnetic field, from which magnetic topology, electrostatic potentials parallel to the magnetic field, and plasma heat flux can be determined. The field of view should be large enough that these anisotropies can be identified and measured. At a minimum, the field of view should cover $\sim 50\%$ of the sky and should include the typical solar wind

magnetic field direction. An angular resolution of $\sim 30^\circ$ is sufficient to characterize anisotropies.

MAGN-05

Ion flux (ionosphere/magnetosphere): Ion flux spans six orders of magnitude, from planetary pickup ions ($\sim 10^4\text{ eV/cm}^2\text{ s ster eV}$) to shocked solar wind H^+ in the magnetosheath ($\sim 10^8\text{--}10^9$) to cold ionospheric O_2^+ ($\sim 10^{10}$). Since the distribution does not change rapidly, low-pickup ion fluxes can be measured over longer timescales (~ 10 minutes) to increase the signal-to-noise ratio.

MAGN-06

Ion energy (ionosphere/magnetosphere): With a periapsis velocity of $\sim 4\text{ km s}^{-1}$ for the elliptical platforms, ionospheric O^+ and O_2^+ have energies of 1.5 and 3 eV , respectively. Cold ion outflow can occur at energies down to $\sim 1\text{ eV}$, and sometimes lower if the spacecraft is moving in the same direction as the flow. Pickup O^+ ions have energies from nearly zero when they are initially ionized to $\sim 50\text{ keV}$ (with gyro radii of several Mars radii) after they have been fully accelerated by the solar wind convection electric field. Ions that are picked up close to the planet, where the neutral density is much higher, have comparatively low energies because of the lower solar wind flow speed and the shorter distance to accelerate. Overall, the pickup ion distribution can be reasonably well-characterized by measuring energies up to $\sim 20\text{ keV}$.

MAGN-07

Ion angular distribution (ionosphere/magnetosphere): In the magnetosheath, shocked solar wind ions are incident from all directions. Accurate plasma moments (density, temperature, pressure) depend on measuring as much of the angular distribution function as possible, preferably over the full sky. Below the exobase, ionospheric O^+ is beamed in the ram

direction because of the spacecraft's supersonic orbital velocity. Above the exobase, ions can be accelerated by electric fields arising from several processes.

MAGN-08

Ion mass (ionosphere/magnetosphere): the mass analyzer portion of the ion instrument should be able to distinguish the major solar wind and planetary ions: H^+ , He^{++} , O^+ , O_2^+ , and CO_2^+ . This is important for constraining the source regions of the measured ion fluxes, for converting ion number fluxes to fluxes of the main species, and for calculating bulk velocity and temperature from the measured energy, direction, and mass.

MAGN-09

Ion flux (solar wind): the flux of the solar wind ion beam is typically in the range 10^7 – 10^{10} eV/cm² s ster eV. This range is encompassed by MAGN-05 above.

MAGN-10

Ion energy (solar wind): solar wind velocities are typically from 250 to 750 km s⁻¹, corresponding to energies of 0.3–3 keV for H^+ and 1.2–12 keV for He^{++} . These ranges are encompassed by MAGN-06.

MAGN-11

Ion angular distribution (solar wind): upstream of Mars' bow shock, the solar wind is a ~ 1 keV beam typically several degrees wide and traveling radially away from the Sun. The beam is deflected and broadened when crossing the bow shock. A $\sim 40^\circ$ wide field of view centered on the Sun direction is needed to measure both the unperturbed and shocked solar wind.

MAGN-12

Vector electric field: the electric fields associated with flows, flow diversions, and macro-scale instabilities are expected to have amplitudes smaller than ~ 300 mV m⁻¹ (DC) with variations smaller than ~ 100 mV m⁻¹ (AC). An accuracy of 1 mV m⁻¹ or 10%, whichever is larger, allows these fields to be characterized.

MAGN-13

Electric field wave power: the low-frequency (<60 Hz) electric field waves associated with current disruption and interchange-like instabilities in the magnetotail current sheet, as well as the higher-frequency waves associated with energization, scattering, and loss of electrons, are expected to have wave powers in the range of 10^{-4} – 10^2 mV m⁻¹/sqrt(Hz). This power should be measured with an accuracy of 10^{-4} mV m⁻¹/sqrt(Hz) or 10%, whichever is larger, to allow this wave power to be characterized.

MAGN-14

Magnetic field wave power: the magnetic field component of plasma waves provides information to distinguish the various types of waves (e.g., ULF, whistler, Alfvén), which in turn provide insight into the physical mechanisms involved (e.g., magnetic reconnection, current disruption, plasma instabilities, particle energization) and to calculate the Poynting flux ($E \times B$), which is a measure of electromagnetic energy flux through the plasma. Magnetic wave power is expected to be in the range of 10^{-4} –1 nT/sqrt(Hz), which should be measured with an accuracy of 10^{-4} nT/sqrt(Hz) or 10%, whichever is larger.

SPA-1

Solar EUV spectral irradiance: the spectral irradiance should be measured in three band passes that probe different regions of the solar atmosphere, which have very different time variability associated with different solar phenomena, such as active

regions and flares. Based on well-established measurements at both Earth and Mars, this irradiance should have an intensity from 10^{-6} to 3×10^{-2} W m⁻² nm⁻¹ and be measured with an accuracy of 15% (dI/I).

SPA-2

Vector magnetic field: Measure the vector magnetic field from ~ 1 to 3000 nT with a sensitivity of 0.3 nT or 10%, whichever is larger, throughout the Mars environment. The magnetic field is essential for interpreting charged particle measurements and for establishing the solar wind properties that drive the interaction with Mars' ionosphere and crustal magnetic fields. The wide dynamic range is needed to measure the solar wind field upstream of the bow shock (~ 1 nT) as well as much larger fields associated with coronal mass ejections that impact Mars. The accuracy on the amplitude is primarily needed to constrain the magnetic field direction when the amplitude is small.

SPA-3

Ion flux: the flux of the solar wind ion beam is typically in the range 10^7 – 10^{10} eV/cm² s ster eV. This range is encompassed by MAGN-05 above.

SPA-4

Ion energy: Solar wind velocities are typically from 250 to 750 km s⁻¹, corresponding to energies of 0.3–3 keV for H^+ and 1.2–12 keV for He^{++} . These ranges are encompassed by MAGN-06.

SPA-5

Ion angular distribution: Upstream of Mars' bow shock, the solar wind is a ~ 1 keV beam typically several degrees wide and traveling radially away from the Sun. The beam is deflected and broadened when crossing the bow shock. A $\sim 40^\circ$ wide field of view centered on the direction of the Sun is needed to measure both the unperturbed and shocked solar wind.

SPA-6

Suprathermal electron flux: Suprathermal electrons consist of upstream and shocked solar wind electrons and accelerated electrons in the induced magnetotail. The solar wind electron distribution at Mars typically peaks at an energy of ~ 10 eV with a flux of $\sim 10^8$ eV/cm² s ster eV. The highest fluxes ($> \sim 10^9$ eV/cm² s ster eV) are observed just downstream of the bow shock. The solar wind electron distribution also has a high-energy halo that can extend out to ~ 1 keV, with fluxes down to 10^4 eV/cm² s ster eV. The halo distribution is typically anisotropic, with a component (the "strahl") that is beamed along the magnetic field. The strahl is an important carrier of heat flux in the solar wind and can be used to determine the magnetic topology of the interplanetary magnetic field (i.e., whether one or both ends of the field line are connected to the solar corona).

SPA-7

Suprathermal electron energy: Solar wind electrons, consisting of core and halo populations, extend from a few eV to ~ 1 keV. Shocked magnetosheath electrons are energized but typically span a similar energy range. Higher-energy electrons are occasionally produced by solar storms (CMEs, solar flares, and interplanetary shocks). Measurements from ~ 1 to ~ 10 keV cover all but the most energetic (and rarest) events. (These higher-energy events are covered by SPA-9 to SPA-11.)

SPA-8

Suprathermal electron angular distribution: Electrons in the solar wind and throughout the Mars environment have thermal

velocities that are much larger than their bulk velocities (or spacecraft orbital velocities). Thus, electrons are incident from all directions. The electron angular distribution has anisotropies with respect to the magnetic field, from which magnetic topology, electrostatic potentials parallel to the magnetic field, and plasma heat flux can be determined. The field of view should be large enough that these anisotropies can be identified and measured. At a minimum, the field of view should cover $\sim 50\%$ of the sky and should include the typical solar wind magnetic field direction. An angular resolution of $\sim 30^\circ$ is sufficient to characterize anisotropies.

SPA-9

Energetic ion/electron flux: Energetic ions and electrons are produced in solar flares, in shock fronts driven by coronal mass ejections, and in other interplanetary shocks, such as those associated with solar wind stream interactions. Based on a long history of measuring these energetic species at Earth and Mars, a flux range of $10\text{--}10^6 \text{ eV/cm}^2 \text{ s ster eV}$ with an accuracy of 10% is sufficient to characterize energetic particle events.

SPA-10

Energetic ion energy: Solar energetic ions span the range from a few keV to 10s of MeV; however, most of the energy deposition in the thermosphere results from ions with energies from 50 keV to a few MeV. An energy resolution of 50% ($\Delta E/E$) is sufficient to resolve energy input at different altitudes.

SPA-11

Energetic electron energy: Solar energetic electrons span the range from a few keV to tens of MeV; however, most of the energy deposition in the thermosphere results from electrons with energies from ~ 50 to a few hundred keV. An energy resolution of 50% ($\Delta E/E$) is sufficient to resolve energy input at different altitudes.

A.7.2. Instruments: Magnetosphere, Ion Escape, and Space Weather

Fluxgate magnetometer (Elliptical, Areo Carrier, and Areo SmallSat A/B platforms)

We have baselined a vector fluxgate magnetometer that measures the intensity and direction of the magnetic field: interplanetary, induced magnetospheric, ionospheric, and crustal. These measurements, when combined with pitch angle distributions (PADs) from the electron spectrometer, help to determine the magnetic structure and topology of the ionosphere, magnetosphere, and magnetotail, as well as low-frequency wave behavior. The magnetometer operates over a very large dynamic range, from $\pm 2048 \text{ nT}$, accommodating the largest field associated with Martian crustal magnetic anomalies (measured from orbit), to $\pm 65,536 \text{ nT}$, allowing operation in the Earth's field. A 16 bit A/D converter results in a resolution of 0.06 nT . The overall sensitivity to ambient fields further depends on spacecraft magnetic cleanliness and the ability to remove spacecraft-generated fields. The instrument operates continuously with a nominal cadence of one vector per second, although higher cadences are possible. The instrument has a mass of 1.3 kg (including a $\sim 1.2 \text{ m}$ boom) and consumes 4.9 W (including heaters). It is highly desirable to have two identical magnetometers, one mounted at the end of the boom and a second mounted closer to the spacecraft. This gradiometer configuration greatly improves the ability to quantify and remove spacecraft generated fields. This instrument has been flown on numerous missions from Voyager to Juno, including two successful Mars missions: MGS (Acuña



Figure 26. Photograph of the MAVEN magnetometer sensor, with shielded harness (Connerney et al. 2015).

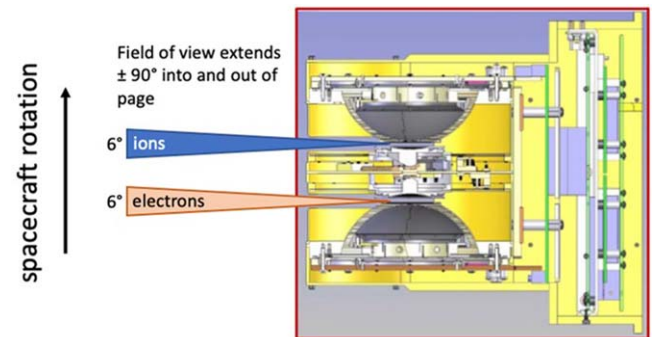


Figure 27. The THEMIS-ESA ion and electron spectrometers are packaged together with a common aperture mechanism and electronics packaging. Both spectrometers have a fan-shaped $180 \times 6^\circ$ field of view that sweeps out the entire sky with no obstructions once per spacecraft spin. Figure shows cutaway of the top-hat electrostatic analyzers. Adapted from Figure 1 of McFadden et al. (2008). The ion spectrometer for MOSAIC would include a time-of-flight (TOF) section (not shown) to discriminate ion mass. This TOF section would be based on that of MAVEN-STATIC (McFadden et al. 2015).

et al. 1992) and MAVEN (Connerney et al. 2015) (see Figure 26). It is TRL 9.

Ion and electron spectrometers (Elliptical platform)

We have baselined a pair of top-hat, hemispheric electrostatic analyzers that measure ion and electron energy per charge. These are largely based on the THEMIS design, which is optimized for a spinning spacecraft (see Figure 27). These sensors have energy resolutions for electrons and ions of 15% and 19% (dE/E , FWHM), respectively. The sensors have programmable energy sweeps that can extend from $<1 \text{ eV}$ to $> 20 \text{ keV}$. The instruments operate continuously, generating 32 energy sweeps (64 sweeps for the ion sensor in solar wind mode) per spin. Both sensors have an instantaneous $180^\circ \times 6^\circ$ field of view, with the 6° direction rotating with the spacecraft to provide 4π steradian coverage once per spin. Angular resolution is 11.25° in rotation phase. Depending on the spacing of 8–16 discrete anodes along the 180° , angular resolutions ranging from 5.625° (to resolve the solar wind ion beam) to 22.5° are typical. The ion instrument would include a time-of-flight section similar to the MAVEN-STATIC design, to separate solar wind H^+ and He^{++} , as well as the major planetary ions (O^+ , O_2^+ , and CO_2^+). The combined

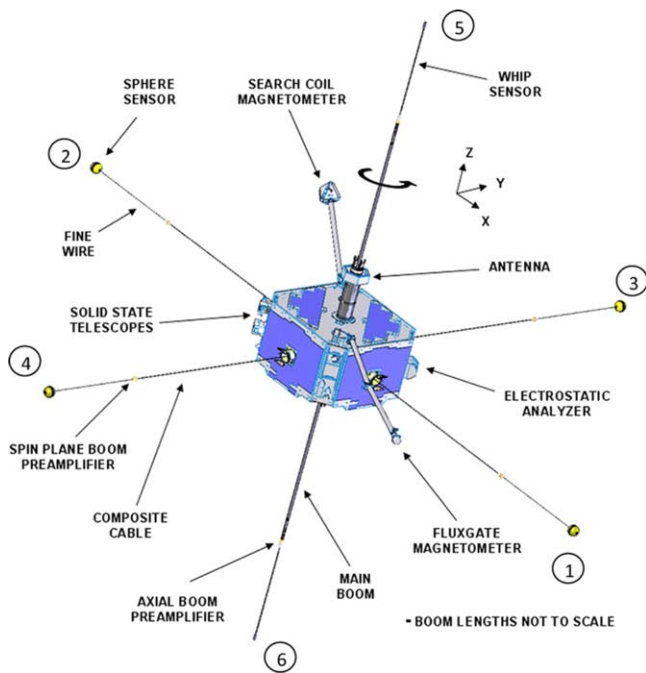


Figure 28. The Elliptical platform is based on the THEMIS spacecraft (Harvey et al. 2008), shown above. This platform carries the Magnetosphere and Ion Escape instruments. The spacecraft spins at 16 RPM to stabilize the radial EFI booms and sweep out the fields of view of the particle instruments (ESA and SST). The steady spin also helps to calibrate the magnetometers.

ion-electron instrument is expected to have a mass of ~ 5 kg and consume ~ 6 W. The electron instrument is TRL 9. The components of the ion instrument (electrostatic analyzer and time-of-flight mass spectrometer) are flight-proven through successful mission operations—e.g., THEMIS-ESA (McFadden et al. 2008), shown in Figure 28, and MAVEN-STATIC (McFadden et al. 2015)—although this particular configuration has not been flown. Thus, the ion instrument is TRL 6.

Electric field instrument (Elliptical platform)

The Electric Field Instrument measures the three components of the ambient electric field over a range of ± 300 mV m $^{-1}$ (DC) and ± 100 mV m $^{-1}$ (AC). Waveform measurements cover DC up to 4 kHz, with AC-coupled differential measurements from ~ 10 Hz to 8 kHz. Onboard spectral measurements cover the same ranges, in addition to providing an estimate of integrated power in the 100–400 kHz band. The instrument also measures the spacecraft floating potential. The instrument operates continuously, producing spin-averaged vectors, waveform data, and spectral data, which can be configured to fit within the available telemetry bandwidth. The instrument, which is based on THEMIS EFI (Bonnell et al. 2008), is composed of six sensors (high-input-impedance, low-noise, broadband digital voltmeters) with preamps at the ends of six booms: four spin-stabilized 22 m wire booms orthogonal to the spin axis, and two 2.5 m stacer booms along the spin axis, as shown in Figure 28. The mass including booms is 12 kg, and the instrument consumes 0.24 W. This instrument is TRL 9.

Search coil magnetometer (Elliptical platform)

The tri-axial Search Coil Magnetometer is designed to measure the magnetic components of plasma waves in the Mars environment. Three search coil antennas cover the bandwidth from 0.1 Hz to 4 kHz, which provides overlap with the fluxgate magnetometer. Each antenna consists of a high magnetic permeability core (which amplifies the ambient field) surrounded

by two wire windings. The main winding, with $\sim 50,000$ turns, passively detects voltage induced by the changing external field. The secondary winding is used to induce feedback to flatten the temperature-dependent frequency response. The sensor is mounted at the end of a rigid one-meter boom. The instrument operates continuously, producing waveforms, FFT processed data, and filter-bank data. The instrument has a mass of 1.8 kg and consumes 0.075 W. The instrument has flown on eight Earth-orbiting and interplanetary missions, most recently THEMIS (Roux et al. 2008). It is TRL 9.

Ion spectrometer (Aero Carrier and Aero SmallSat A/B platforms)

The ion spectrometer for the non-spinning areostationary platform is a toroidal electrostatic analyzer with electrostatic deflectors to provide a $360 \times 90^\circ$ field of view, with a mechanical attenuator to provide a high dynamic range. The instrument measures ions from 5 eV to 25 keV, with an energy resolution of 14.5% (dE/E , FWHM) and an angular resolution of $3.75^\circ \times 4.5^\circ$ in the sunward direction and $22.5^\circ \times 22.5^\circ$ elsewhere. The instrument operates continuously, generating energy-angle distributions, energy spectra, and bulk moments. These data products are packaged into telemetry with different (adjustable) cadences to fit within the available telemetry bandwidth. This instrument would be based closely on MAVEN-SWIA (shown in Figure 28 left) (Halekas et al. 2015), which has a mass of 2.6 kg and consumes 2.1 W. It is TRL 9.

Electron spectrometer (Aero Carrier and Aero SmallSat A/B platforms)

The electron spectrometer is a hemispherical electrostatic analyzer with electrostatic deflectors to provide a $360 \times 120^\circ$ field of view. The instrument measures the energy and angle distributions of electrons from 3 eV to 4.6 keV with an energy resolution of 17% (dE/E , FWHM) and an angular resolution of $22.5 \times 20^\circ$. The instrument has two concentric toroidal entrance grids across which a sweepable potential can be placed to decelerate electrons as they enter the analyzer. This can be used to provide finer energy resolution for measuring ionospheric photoelectrons, for lowering the sensitivity to high magnetosheath fluxes, and to calibrate the low-energy response in flight. The instrument operates continuously, generating energy-angle distributions, PADs, and energy spectra with different cadences to fit within the available telemetry bandwidth. PADs are calculated on board in real time using data from the fluxgate magnetometer. This allows high-cadence PADs with modest telemetry usage. This instrument would be based closely on MAVEN-SWEA (shown in Figure 29 right) (Mitchell et al. 2016), which has a mass of 1.8 kg and consumes 1.6 W. It is TRL 9.

Solid-state telescope (Energetic Particle Detector) (Aero Carrier and Aero SmallSat A platforms)

The solid-state telescope measures the energy spectrum and angular distribution of energetic electrons (20–1000 keV) and ions (20–6000 keV). It consists of two identical sensors located on the spacecraft body. Each sensor consists of a dual, double-ended telescope that collimates ions and electrons onto a stack of three passivated ion-implanted silicon detectors. One end of the telescope is covered by a foil that stops ions below 400 keV, while the opposite end has a broom magnet that sweeps away electrons below 400 keV, so ions and electrons below this energy are cleanly separated. Higher-energy electrons and ions are identified by the energy loss in an

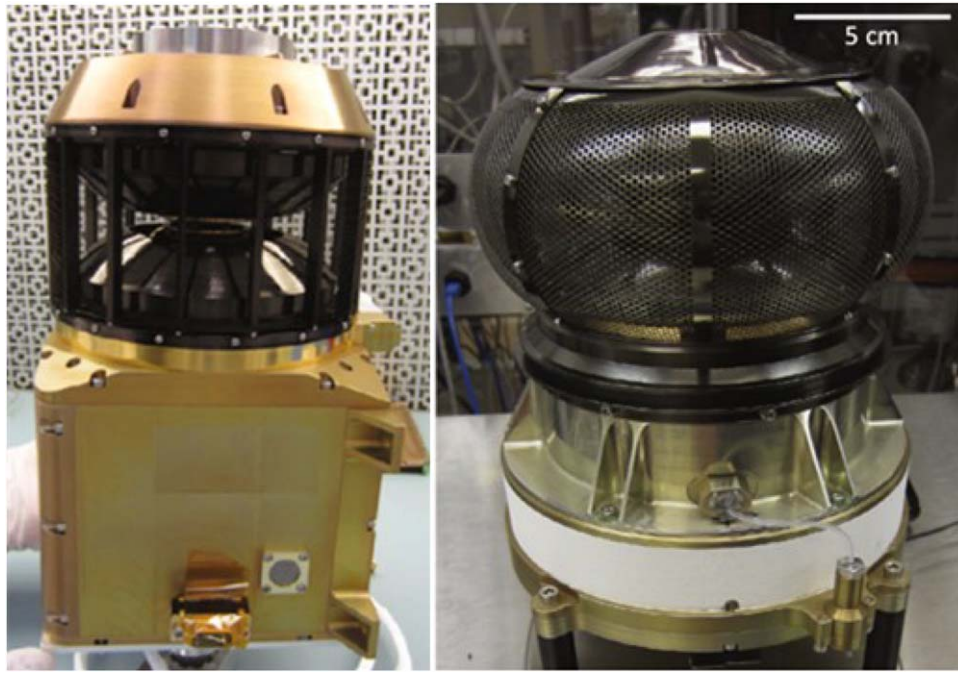


Figure 29. The ion and electron spectrometers on the Areo platforms are based on the MAVEN Solar Wind Ion Analyzer (Halekas et al. 2015), left, and Solar Wind Electron Analyzer (Mitchell et al. 2016), right. Both instruments use electrostatic deflectors to increase their fields of view on a three-axis stabilized spacecraft.

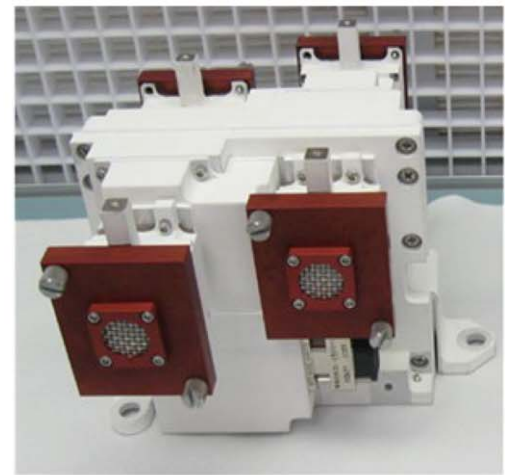
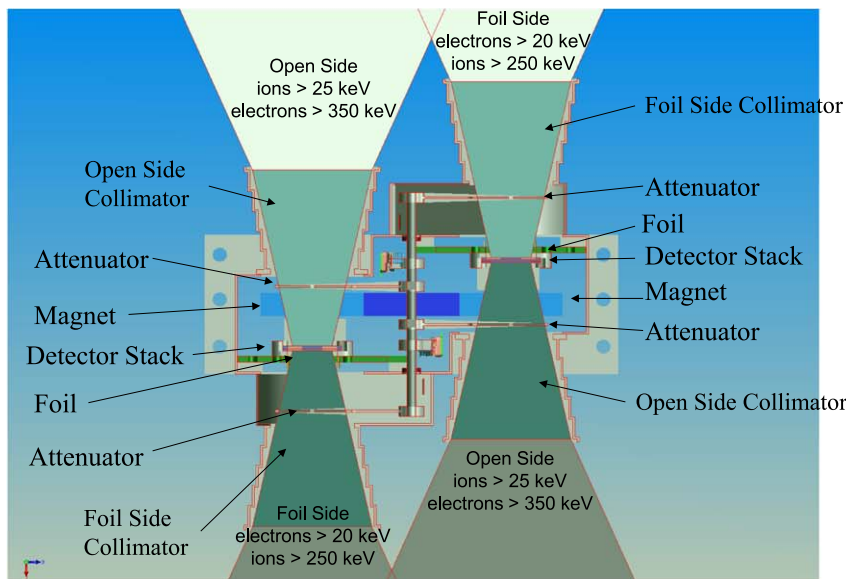


Figure 30. The solid-state telescope on the Aero platforms is based on MAVEN SEP (Larson et al. 2015), above. Top: Cross section showing the locations of the solid-state detector stack and the positions of sweep magnets and foils to separate energetic ions and electrons. Bottom: MAVEN SEP flight model. Red aperture covers are for protection on the ground and are removed for flight.

outside detector (dE/dx) coincident with the energy (E) deposited in the center detector. Two telescopes are packaged with oppositely directed sweep magnets sharing a yoke to save mass and minimize stray fields (see Figure 30). Each telescope has a rectangular $42 \times 31^\circ$ field of view. The instrument operates continuously, measuring events once per second, which are collected, accumulated, and packetized to fit within the available telemetry bandwidth. A total of 128 energy/angle bins are available for accumulations, allowing 16 energy steps \times 4 angles \times 2 species per time step. The instrument has

a mass of 0.9 kg and consumes an average power of 5.5 W. This instrument has been flown on MAVEN (shown in Figure 30) (Larson et al. 2015), THEMIS, and STEREO (Lin et al. 2008). It is TRL 9.

EUV monitor (Areo Carrier and Areo SmallSat A platforms)

The EUV monitor is a set of four photometers that consist of very stable Si photodiodes covered by thin metal film or interference filters and a pre-amplifier circuit. Different filters provide sensitivity in three wavelength ranges: C/Al/Nb/C thin foil (17–22 nm), C/Al/Ti/C thin foil (0.1–7 nm), and an

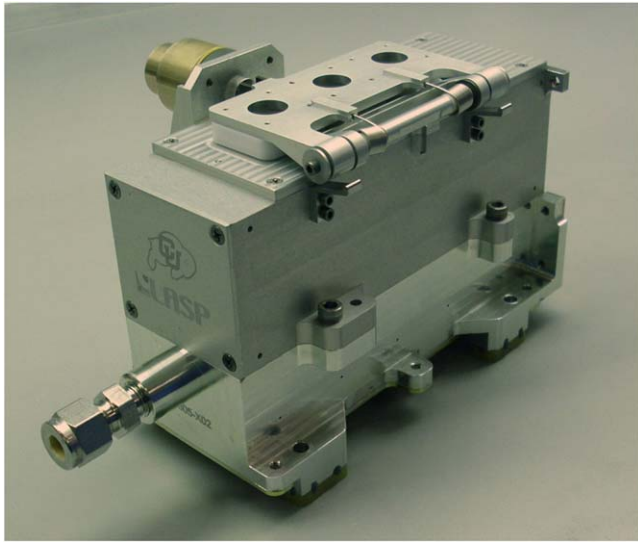


Figure 31. The MAVEN EUV monitor (Eparvier et al. 2015) shown on a lab bench. Photo credit: University of Colorado LASP.

interference filter for $\text{Ly}\alpha$ (121–122 nm). A fourth diode is permanently covered to monitor variations in dark signal due to

temperature and radiation background changes. The three science channels monitor emissions from the highly variable corona and transition region of the solar atmosphere. The instrument operates continuously with a measurement cadence of 1 s. The broadband sensors monitor the most rapid changes in solar irradiance due to flares. These measurements can be used in a spectral irradiance model (M-FISM) to generate the full EUV spectrum at Mars from 0.1 to 190 nm in 1 nm bins (Thiemann et al. 2017). The instrument has a mass of 1.1 kg and consumes 0.73 W. The instrument is based on MAVEN-EUVM (Eparvier et al. 2015) (see Figure 31), with three modifications: (1) a smaller, lower-power electronics box, (2) a smaller, lower-mass photometer system, and (3) a modified optical path that includes a reflection to reject soft X-rays for improved sensitivity in the 17–22 nm channel. It is currently TRL 4, but could be brought to TRL 6 within ~ 6 months.

A.8. Measurement Requirements

Figure 32 provides detailed requirements for all of MOSAIC’s required measurements, separately for each of the eight scientific investigations.

																			Observable Quantity (OQ).															Mass (where applicable)			
																			Separate from physical parameter for remote data.															Mass Range		Mass Resolution	
ID	Instrument Type(s)	Physical Parameter (PP) Description	Link to Objectives	Units	PP Range	PP Resolution	PP Altitude Range	PP Altitude Resolution	PP Coordinate System	PP Local Time (LT) Range	PP LT Resolution	PP Longitude Range	PP Longitude Resolution	PP Latitude Range	PP Latitude Resolution	PP Cadence	PP Seasonal Range	PP Seasonal Resolution	OQ Description	OQ Units	OQ Dynamic Range	OQ Precision	OQ SNR	OQ Time Resolution	Angular FOV (X) range	Azimuth (X) Resolution	Polar (Y) Range	Polar (Y) Resolution	Energy/Wavelength/Frequency Range	Resolution							
ICE-1	Radar (P-band Polarimetric SAR)	Surface ice distribution over time	Objectives I.A. - II.A. Essential for monitoring of surface changes due to volatile exchange with the atmosphere and for the characterization of potentially extractable water ice resources	Percent ice coverage per unit area over time	0-100%	10%	0 m	N/A	IAU Mars	0-24 h	N/A	180°W - 180°E	30 m	80°S - 80°N	30 m	N/A - Cadence determined by orbital speed and longitude/latitude resolution	0-360° Ls	90°	Returned radar power as a ratio of a standard power	Watts or dimensionless	-30 dB to infinity (saturation level of instrument)	-30 dB noise limit	9	N/A - Cadence determined by orbital speed and longitude/latitude resolution.	N/A - no imaging. Each integration is one "pixel"	0.15°	N/A - no imaging. Each integration is one "pixel"	3°	350-450 MHz	N/A each pulse is a multi-frequency 'chirp'	N/A	N/A					
ICE-2	Radar (P-band Polarimetric SAR)	Near-surface moisture content	Objectives I.A. - II.A. Essential for monitoring of surface changes due to volatile exchange with the atmosphere and for the characterization of potentially extractable water ice resources	Percentage (%)	0-100%	Moisture content: 0-1 cm³/cm³	0-3 m subsurface	Bulk measurement (no resolution, sensitive to entire column)	IAU Mars	0-24 h	N/A	180°W - 180°E	30 m	80°S - 80°N	30 m	N/A - Cadence determined by orbital speed and longitude/latitude resolution	0-360° Ls	90°	Circular polarization ratio	Dimensionless	0-2	0.1	N/A	N/A - Cadence determined by orbital speed and longitude/latitude resolution.	N/A - no imaging. Each integration is one "pixel"	0.15°	N/A - no imaging. Each integration is one "pixel"	3°	350-450 MHz	N/A each pulse is a multi-frequency 'chirp'	N/A	N/A					
ICE-2	Radar (P-band Sounder)	Near-surface moisture content	Objectives I.A. - II.A. Essential for monitoring of surface changes due to volatile exchange with the atmosphere and for the characterization of potentially extractable water ice resources	Percentage (%)	0-100%	Moisture content: 0-1 cm³/cm³	1-15 m subsurface	0.8 m in water ice	IAU Mars	0-24 h	N/A	180°W - 180°E	1 km	80°S - 80°N	1 km	N/A - Cadence determined by orbital speed and longitude/latitude resolution	0-360° Ls	90°	Dielectric permittivity	Dimensionless	0-15	0.1	maximum 9 (decreases with depth)	N/A - Cadence determined by orbital speed and longitude/latitude resolution.	N/A - no imaging. Each integration is one "pixel"	0.15°	N/A - no imaging. Each integration is one "pixel"	3°	350-450 MHz	N/A each pulse is a multi-frequency 'chirp'	N/A	N/A					
ICE-3	Wide angle imager (VIS)	Surface ice distribution over time	Objectives I.A. - II.A. Essential for monitoring of surface changes due to volatile exchange with the atmosphere and for the characterization of potentially extractable water ice resources	Percent ice coverage per unit area over time	0-100%	10%	N/A	N/A	IAU Mars	Daytime	N/A	180°W - 180°E	1 km	80°S - 80°N	1 km	Daily global coverage (as downlink rate allows)	0-360° Ls	90°	RGB values	Data number (DN)	0-2047 (11 bit)	< 10% (VIS), < 20% (UV)	> 100 (VIS)	10-100 s msec (VIS), 1-10 s sec (UV)	22°	0.01°	22°	0.01°	0.34-0.75 µm, 1.1-1.6 µm	6 channels between 0.34-0.75 µm, 6 channels between 1.1-1.6 µm	N/A	N/A					
ATM-1	Radio occultation	Vertical profile of temperature	Objectives I.B. - I.C.1. - II.B. Essential for monitoring of atmospheric state and collection of comparison with long-term climatologies.	Kelvin	150-300 K	1 K near the surface (10 K at 40 km)	0-40 km	2 km or less	PC	0-24 h	depends on number of satellites and orbits	180°W - 180°E	~ 1°	90°S - 90°N possible (depends on orbits)	~ 1 deg	up to ~30 soundings/ daily per pair of spacecrafts	0-360° Ls	depends on number of satellites and orbits	Doppler shift	Hz	10 Hz at X-band	10 mHz at X-band	50 dB-Hz	0.1 sec	60°	N/A	10°	N/A	1-10 GHz	N/A	N/A	N/A					
ATM-2	Radio occultation (Added Sub-mm here as note that it's derived along with other variables)	Vertical profile of pressure	Objectives I.B. - I.C.1. - II.B. Essential for monitoring of atmospheric state and collection of comparison with long-term climatologies.	Pascals	10⁻³ - 10³ Pa, Sub-mm: derived with other variables	2 Pa near the surface (0.6 Pa at 40 km)	0-40 km	2 km or less	PC	0-24 h	depends on number of satellites and orbits	180°W - 180°E	~ 1°	90°S - 90°N possible (depends on orbits)	~ 1 deg	up to ~30 soundings/ daily per pair of spacecrafts	0-360° Ls	depends on number of satellites and orbits	Doppler shift	Hz	10 Hz at X-band	10 mHz at X-band	50 dB-Hz	0.1 sec	60°	N/A	10°	N/A	1-10 GHz	N/A	N/A	N/A					

Figure 32. Detailed Requirements for Each of the Measurements Required to Complete the Eight MOSAIC Science Investigations

Instrument ID	Physical Parameter Description	Link to Objectives	Units	PP Range	PP Resolution	PP Altitude	PP Coord. System	PP Local Time	PP Long. Range	PP Long. Resolution	PP Latitude Range	PP Latitude Resolution	PP Cadence	PP Seasonal Range	PP Seasonal Resolution	PP Description	Separate from physical parameter for remote data.	Angular FOV	Polar (°) Resolution	Energy/ Frequency Range	Resolution	Mass (where applicable)
ATM-3 Thermal infrared spectrometer	Vertical profile of temperature	Objectives I.C.1 - I.B. Essential for monitoring of atmospheric state and collection of comparison with long-term climatologies.	Kelvin	10-280 K	2 K	0-50 km	PC	2 local times (2-3AMP)	180°E - 180°W	180°E - 180°W	1-4°	1-4°	20 sols	0-360° Ls	1-2° Ls	Radiance (W m ⁻² sr ⁻¹ μm ⁻¹)	Dynamic Range: 1000 K	2-5 mm; 180° azimuth	N/A	micron (CO ₂ band); integrated near infrared (differential absorption lidar)	Sub-mm; 455 GHz; tunable	N/A
ATM-4 Thermal infrared spectrometer	Vertical profile of pressure	Objectives I.C.1 - I.B. Essential for monitoring of atmospheric state and collection of comparison with long-term climatologies.	Pascals	10 ⁻⁵ - 10 ⁻¹ Pa	5%	0-50 km	PC	2 local times (2-3AMP)	180°E - 180°W	180°E - 180°W	1-4°	1-4°	20 sols	0-360° Ls	1-2° Ls	Radiance (W m ⁻² sr ⁻¹ μm ⁻¹)	Dynamic Range: 1000 K	2-5 mm; 180° azimuth	N/A	micron (CO ₂ band); integrated near infrared (differential absorption lidar)	Sub-mm; 455 GHz; tunable	N/A
ATM-5 Microwave radar and doppler lidar	Vertical profile of its zonal and meridional components (U/V) atmospheric circulation	Objectives I.B. - I.C.1 - I.B. Essential for monitoring of atmospheric state and collection of comparison with long-term climatologies.	Meters per second	0-180 m/s	5 m/s	0-50 km	PC	2 local times (2-3AMP)	180°E - 180°W	180°E - 180°W	1-4°	1-4°	20 sols	0-360° Ls	1-2° Ls	Doppler shift in backscatter light (lidar)	Dynamic Range: 1000 K	2-5 mm; 180° azimuth	N/A	micron (CO ₂ band); integrated near infrared (differential absorption lidar)	Sub-mm; 455 GHz; tunable	N/A
ATM-6 Thermal infrared spectrometer	Vertical profile of dust opacity	Objectives I.B. - I.C.1 - I.B. Essential for monitoring of atmospheric state and collection of comparison with long-term climatologies.	Per kilometer (relief)	10 ⁻⁴ - 10 ⁻¹ km ⁻¹	1-20%	0-50 km	PC	2 local times (2-3AMP)	180°E - 180°W	180°E - 180°W	1-4°	1-4°	20 sols	0-360° Ls	1-2° Ls	Scattering (lidar)	Dynamic Range: 1000 K	2-5 mm; 180° azimuth	N/A	micron (CO ₂ band); integrated near infrared (differential absorption lidar)	Sub-mm; 455 GHz; tunable	N/A
ATM-7 Thermal infrared spectrometer	Vertical profile of water ice opacity	Objectives I.A - I.B. Essential for monitoring of atmospheric state, water cycle, and collection of comparison with long-term climatologies.	Per kilometer (relief)	10 ⁻⁴ - 10 ⁻¹ km ⁻¹	1-20%	0-50 km	PC	2 local times (2-3AMP)	180°E - 180°W	180°E - 180°W	1-4°	1-4°	20 sols	0-360° Ls	1-2° Ls	Scattering (lidar)	Dynamic Range: 1000 K	2-5 mm; 180° azimuth	N/A	micron (CO ₂ band); integrated near infrared (differential absorption lidar)	Sub-mm; 455 GHz; tunable	N/A

Figure 32. (Continued.)

ID	Instrument Type(s)	Physical Parameter Description (PP)	Link to Objectives	Units	Observable Quantity (OQ)										Separate from physical parameter for meta-data					Angular Resolution					Polar (Y) Resolution	Energy/Wavelength Range	Frequency Resolution	Mass (where applicable)
					PP Resolution	PP Range	PP Altitude	PP Latitude	PP Longitude	PP Local Time	PP LT Range	PP LT Resolution	PP Latitude Resolution	PP Longitude Resolution	PP Cadence	PP Seasonal Resolution	PP Description	QO Units	QO Dynamic Range	QO Precision	QO SRR	QO Time Resolution	QO Azimuth (X) Resolution	QO Altitude Resolution				
YTM-8	Thermal infrared spectrometer/radiometer/lidar	Vertical profile of carbon dioxide (scattering) and methane (absorption) opacity	Objectives 1A, 1B, 1C, 1D, 1E, 1F, 1G, 1H, 1I, 1J, 1K, 1L, 1M, 1N, 1O, 1P, 1Q, 1R, 1S, 1T, 1U, 1V, 1W, 1X, 1Y, 1Z, 1AA, 1AB, 1AC, 1AD, 1AE, 1AF, 1AG, 1AH, 1AI, 1AJ, 1AK, 1AL, 1AM, 1AN, 1AO, 1AP, 1AQ, 1AR, 1AS, 1AT, 1AU, 1AV, 1AW, 1AX, 1AY, 1AZ, 1BA, 1BB, 1BC, 1BD, 1BE, 1BF, 1BG, 1BH, 1BI, 1BJ, 1BK, 1BL, 1BM, 1BN, 1BO, 1BP, 1BQ, 1BR, 1BS, 1BT, 1BU, 1BV, 1BW, 1BX, 1BY, 1BZ, 1CA, 1CB, 1CC, 1CD, 1CE, 1CF, 1CG, 1CH, 1CI, 1CJ, 1CK, 1CL, 1CM, 1CN, 1CO, 1CP, 1CQ, 1CR, 1CS, 1CT, 1CU, 1CV, 1CW, 1CX, 1CY, 1CZ, 1DA, 1DB, 1DC, 1DD, 1DE, 1DF, 1DG, 1DH, 1DI, 1DJ, 1DK, 1DL, 1DM, 1DN, 1DO, 1DP, 1DQ, 1DR, 1DS, 1DT, 1DU, 1DV, 1DW, 1DX, 1DY, 1DZ, 1EA, 1EB, 1EC, 1ED, 1EE, 1EF, 1EG, 1EH, 1EI, 1EJ, 1EK, 1EL, 1EM, 1EN, 1EO, 1EP, 1EQ, 1ER, 1ES, 1ET, 1EU, 1EV, 1EW, 1EX, 1EY, 1EZ, 1FA, 1FB, 1FC, 1FD, 1FE, 1FF, 1FG, 1FH, 1FI, 1FJ, 1FK, 1FL, 1FM, 1FN, 1FO, 1FP, 1FQ, 1FR, 1FS, 1FT, 1FU, 1FV, 1FW, 1FX, 1FY, 1FZ, 1GA, 1GB, 1GC, 1GD, 1GE, 1GF, 1GG, 1GH, 1GI, 1GJ, 1GK, 1GL, 1GM, 1GN, 1GO, 1GP, 1GQ, 1GR, 1GS, 1GT, 1GU, 1GV, 1GW, 1GX, 1GY, 1GZ, 1HA, 1HB, 1HC, 1HD, 1HE, 1HF, 1HG, 1HH, 1HI, 1HJ, 1HK, 1HL, 1HM, 1HN, 1HO, 1HP, 1HQ, 1HR, 1HS, 1HT, 1HU, 1HV, 1HW, 1HX, 1HY, 1HZ, 1IA, 1IB, 1IC, 1ID, 1IE, 1IF, 1IG, 1IH, 1II, 1IJ, 1IK, 1IL, 1IM, 1IN, 1IO, 1IP, 1IQ, 1IR, 1IS, 1IT, 1IU, 1IV, 1IW, 1IX, 1IY, 1IZ, 1JA, 1JB, 1JC, 1JD, 1JE, 1JF, 1JG, 1JH, 1JI, 1JJ, 1JK, 1JL, 1JM, 1JN, 1JO, 1JP, 1JQ, 1JR, 1JS, 1JT, 1JU, 1JV, 1JW, 1JX, 1JY, 1JZ, 1KA, 1KB, 1KC, 1KD, 1KE, 1KF, 1KG, 1KH, 1KI, 1KJ, 1KK, 1KL, 1KM, 1KN, 1KO, 1KP, 1KQ, 1KR, 1KS, 1KT, 1KU, 1KV, 1KW, 1KX, 1KY, 1KZ, 1LA, 1LB, 1LC, 1LD, 1LE, 1LF, 1LG, 1LH, 1LI, 1LJ, 1LK, 1LL, 1LM, 1LN, 1LO, 1LP, 1LQ, 1LR, 1LS, 1LT, 1LU, 1LV, 1LW, 1LX, 1LY, 1LZ, 1MA, 1MB, 1MC, 1MD, 1ME, 1MF, 1MG, 1MH, 1MI, 1MJ, 1MK, 1ML, 1MN, 1MO, 1MP, 1MQ, 1MR, 1MS, 1MT, 1MU, 1MV, 1MW, 1MX, 1MY, 1MZ, 1NA, 1NB, 1NC, 1ND, 1NE, 1NF, 1NG, 1NH, 1NI, 1NJ, 1NK, 1NL, 1NM, 1NO, 1NP, 1NQ, 1NR, 1NS, 1NT, 1NU, 1NV, 1NW, 1NX, 1NY, 1NZ, 1OA, 1OB, 1OC, 1OD, 1OE, 1OF, 1OG, 1OH, 1OI, 1OJ, 1OK, 1OL, 1OM, 1ON, 1OO, 1OP, 1OQ, 1OR, 1OS, 1OT, 1OU, 1OV, 1OW, 1OX, 1OY, 1OZ, 1PA, 1PB, 1PC, 1PD, 1PE, 1PF, 1PG, 1PH, 1PI, 1PJ, 1PK, 1PL, 1PM, 1PN, 1PO, 1PP, 1PQ, 1PR, 1PS, 1PT, 1PU, 1PV, 1PW, 1PX, 1PY, 1PZ, 1QA, 1QB, 1QC, 1QD, 1QE, 1QF, 1QG, 1QH, 1QI, 1QJ, 1QK, 1QL, 1QM, 1QN, 1QO, 1QP, 1QQ, 1QR, 1QS, 1QT, 1QU, 1QV, 1QW, 1QX, 1QY, 1QZ, 1RA, 1RB, 1RC, 1RD, 1RE, 1RF, 1RG, 1RH, 1RI, 1RJ, 1RK, 1RL, 1RM, 1RN, 1RO, 1RP, 1RQ, 1RR, 1RS, 1RT, 1RU, 1RV, 1RW, 1RX, 1RY, 1RZ, 1SA, 1SB, 1SC, 1SD, 1SE, 1SF, 1SG, 1SH, 1SI, 1SJ, 1SK, 1SL, 1SM, 1SN, 1SO, 1SP, 1SQ, 1SR, 1SS, 1ST, 1SU, 1SV, 1SW, 1SX, 1SY, 1SZ, 1TA, 1TB, 1TC, 1TD, 1TE, 1TF, 1TG, 1TH, 1TI, 1TJ, 1TK, 1TL, 1TM, 1TN, 1TO, 1TP, 1TQ, 1TR, 1TS, 1TT, 1TU, 1TV, 1TW, 1TX, 1TY, 1TZ, 1UA, 1UB, 1UC, 1UD, 1UE, 1UF, 1UG, 1UH, 1UI, 1UJ, 1UK, 1UL, 1UM, 1UN, 1UO, 1UP, 1UQ, 1UR, 1US, 1UT, 1UU, 1UV, 1UW, 1UX, 1UY, 1UZ, 1VA, 1VB, 1VC, 1VD, 1VE, 1VF, 1VG, 1VH, 1VI, 1VJ, 1VK, 1VL, 1VM, 1VN, 1VO, 1VP, 1VQ, 1VR, 1VS, 1VT, 1VU, 1VV, 1VW, 1VX, 1VY, 1VZ, 1WA, 1WB, 1WC, 1WD, 1WE, 1WF, 1WG, 1WH, 1WI, 1WJ, 1WK, 1WL, 1WM, 1WN, 1WO, 1WP, 1WQ, 1WR, 1WS, 1WT, 1WU, 1WV, 1WW, 1WX, 1WY, 1WZ, 1XA, 1XB, 1XC, 1XD, 1XE, 1XF, 1XG, 1XH, 1XI, 1XJ, 1XK, 1XL, 1XM, 1XN, 1XO, 1XP, 1XQ, 1XR, 1XS, 1XT, 1XU, 1XV, 1XW, 1XX, 1XY, 1XZ, 1YA, 1YB, 1YC, 1YD, 1YE, 1YF, 1YG, 1YH, 1YI, 1YJ, 1YK, 1YL, 1YM, 1YN, 1YO, 1YP, 1YQ, 1YR, 1YS, 1YT, 1YU, 1YV, 1YW, 1YX, 1YY, 1YZ, 1ZA, 1ZB, 1ZC, 1ZD, 1ZE, 1ZF, 1ZG, 1ZH, 1ZI, 1ZJ, 1ZK, 1ZL, 1ZM, 1ZN, 1ZO, 1ZP, 1ZQ, 1ZR, 1ZS, 1ZT, 1ZU, 1ZV, 1ZW, 1ZX, 1ZY, 1ZZ, 2AA, 2AB, 2AC, 2AD, 2AE, 2AF, 2AG, 2AH, 2AI, 2AJ, 2AK, 2AL, 2AM, 2AN, 2AO, 2AP, 2AQ, 2AR, 2AS, 2AT, 2AU, 2AV, 2AW, 2AX, 2AY, 2AZ, 2BA, 2BB, 2BC, 2BD, 2BE, 2BF, 2BG, 2BH, 2BI, 2BJ, 2BK, 2BL, 2BM, 2BN, 2BO, 2BP, 2BQ, 2BR, 2BS, 2BT, 2BU, 2BV, 2BW, 2BX, 2BY, 2BZ, 2CA, 2CB, 2CC, 2CD, 2CE, 2CF, 2CG, 2CH, 2CI, 2CJ, 2CK, 2CL, 2CM, 2CN, 2CO, 2CP, 2CQ, 2CR, 2CS, 2CT, 2CU, 2CV, 2CW, 2CX, 2CY, 2CZ, 2DA, 2DB, 2DC, 2DD, 2DE, 2DF, 2DG, 2DH, 2DI, 2DJ, 2DK, 2DL, 2DM, 2DN, 2DO, 2DP, 2DQ, 2DR, 2DS, 2DT, 2DU, 2DV, 2DW, 2DX, 2DY, 2DZ, 2EA, 2EB, 2EC, 2ED, 2EE, 2EF, 2EG, 2EH, 2EI, 2EJ, 2EK, 2EL, 2EM, 2EN, 2EO, 2EP, 2EQ, 2ER, 2ES, 2ET, 2EU, 2EV, 2EW, 2EX, 2EY, 2EZ, 2FA, 2FB, 2FC, 2FD, 2FE, 2FF, 2FG, 2FH, 2FI, 2FJ, 2FK, 2FL, 2FM, 2FN, 2FO, 2FP, 2FQ, 2FR, 2FS, 2FT, 2FU, 2FV, 2FW, 2FX, 2FY, 2FZ, 2GA, 2GB, 2GC, 2GD, 2GE, 2GF, 2GG, 2GH, 2GI, 2GJ, 2GK, 2GL, 2GM, 2GN, 2GO, 2GP, 2GQ, 2GR, 2GS, 2GT, 2GU, 2GV, 2GW, 2GX, 2GY, 2GZ, 2HA, 2HB, 2HC, 2HD, 2HE, 2HF, 2HG, 2HH, 2HI, 2HJ, 2HK, 2HL, 2HM, 2HN, 2HO, 2HP, 2HQ, 2HR, 2HS, 2HT, 2HU, 2HV, 2HW, 2HX, 2HY, 2HZ, 2IA, 2IB, 2IC, 2ID, 2IE, 2IF, 2IG, 2IH, 2II, 2IJ, 2IK, 2IL, 2IM, 2IN, 2IO, 2IP, 2IQ, 2IR, 2IS, 2IT, 2IU, 2IV, 2IW, 2IX, 2IY, 2IZ, 2JA, 2JB, 2JC, 2JD, 2JE, 2JF, 2JG, 2JH, 2JI, 2JJ, 2JK, 2JL, 2JM, 2JN, 2JO, 2JP, 2JQ, 2JR, 2JS, 2JT, 2JU, 2JV, 2JW, 2JX, 2JY, 2JZ, 2KA, 2KB, 2KC, 2KD, 2KE, 2KF, 2KG, 2KH, 2KI, 2KJ, 2KK, 2KL, 2KM, 2KN, 2KO, 2KP, 2KQ, 2KR, 2KS, 2KT, 2KU, 2KV, 2KW, 2KX, 2KY, 2KZ, 2LA, 2LB, 2LC, 2LD, 2LE, 2LF, 2LG, 2LH, 2LI, 2LJ, 2LK, 2LL, 2LM, 2LN, 2LO, 2LP, 2LQ, 2LR, 2LS, 2LT, 2LU, 2LV, 2LW, 2LX, 2LY, 2LZ, 2MA, 2MB, 2MC, 2MD, 2ME, 2MF, 2MG, 2MH, 2MI, 2MJ, 2MK, 2ML, 2MN, 2MO, 2MP, 2MQ, 2MR, 2MS, 2MT, 2MU, 2MV, 2MW, 2MX, 2MY, 2MZ, 2NA, 2NB, 2NC, 2ND, 2NE, 2NF, 2NG, 2NH, 2NI, 2NJ, 2NK, 2NL, 2NM, 2NO, 2NP, 2NQ, 2NR, 2NS, 2NT, 2NU, 2NV, 2NW, 2NX, 2NY, 2NZ, 2OA, 2OB, 2OC, 2OD, 2OE, 2OF, 2OG, 2OH, 2OI, 2OJ, 2OK, 2OL, 2OM, 2ON, 2OO, 2OP, 2OQ, 2OR, 2OS, 2OT, 2OU, 2OV, 2OW, 2OX, 2OY, 2OZ, 2PA, 2PB, 2PC, 2PD, 2PE, 2PF, 2PG, 2PH, 2PI, 2PJ, 2PK, 2PL, 2PM, 2PN, 2PO, 2PP, 2PQ, 2PR, 2PS, 2PT, 2PU, 2PV, 2PW, 2PX, 2PY, 2PZ, 2QA, 2QB, 2QC, 2QD, 2QE, 2QF, 2QG, 2QH, 2QI, 2QJ, 2QK, 2QL, 2QM, 2QN, 2QO, 2QP, 2QQ, 2QR, 2QS, 2QT, 2QU, 2QV, 2QW, 2QX, 2QY, 2QZ, 2RA, 2RB, 2RC, 2RD, 2RE, 2RF, 2RG, 2RH, 2RI, 2RJ, 2RK, 2RL, 2RM, 2RN, 2RO, 2RP, 2RQ, 2RR, 2RS, 2RT, 2RU, 2RV, 2RW, 2RX, 2RY, 2RZ, 2SA, 2SB, 2SC, 2SD, 2SE, 2SF, 2SG, 2SH, 2SI, 2SJ, 2SK, 2SL, 2SM, 2SN, 2SO, 2SP, 2SQ, 2SR, 2SS, 2ST, 2SU, 2SV, 2SW, 2SX, 2SY, 2SZ, 2TA, 2TB, 2TC, 2TD, 2TE, 2TF, 2TG, 2TH, 2TI, 2TJ, 2TK, 2TL, 2TM, 2TN, 2TO, 2TP, 2TQ, 2TR, 2TS, 2TT, 2TU, 2TV, 2TW, 2TX, 2TY, 2TZ, 2UA, 2UB, 2UC, 2UD, 2UE, 2UF, 2UG, 2UH, 2UI, 2UJ, 2UK, 2UL, 2UM, 2UN, 2UO, 2UP, 2UQ, 2UR, 2US, 2UT, 2UU, 2UV, 2UW, 2UX, 2UY, 2UZ, 2VA, 2VB, 2VC, 2VD, 2VE, 2VF, 2VG, 2VH, 2VI, 2VJ, 2VK, 2VL, 2VM, 2VN, 2VO, 2VP, 2VQ, 2VR, 2VS, 2VT, 2VU, 2VV, 2VW, 2VX, 2VY, 2VZ, 2WA, 2WB, 2WC, 2WD, 2WE, 2WF, 2WG, 2WH, 2WI, 2WJ, 2WK, 2WL, 2WM, 2WN, 2WO, 2WP, 2WQ, 2WR, 2WS, 2WT, 2WU, 2WV, 2WW, 2WX, 2WY, 2WZ, 2XA, 2XB, 2XC, 2XD, 2XE, 2XF, 2XG, 2XH, 2XI, 2XJ, 2XK, 2XL, 2XM, 2XN, 2XO, 2XP, 2XQ, 2XR, 2XS, 2XT, 2XU, 2XV, 2XW, 2XX, 2XY, 2XZ, 2YA, 2YB, 2YC, 2YD, 2YE, 2YF, 2YG, 2YH, 2YI, 2YJ, 2YK, 2YL, 2YM, 2YN, 2YO, 2YP, 2YQ, 2YR, 2YS, 2YT, 2YU, 2YV, 2YW, 2YX, 2YY, 2YZ, 2ZA, 2ZB, 2ZC, 2ZD, 2ZE, 2ZF, 2ZG, 2ZH, 2ZI, 2ZJ, 2ZK, 2ZL, 2ZM, 2ZN, 2ZO, 2ZP, 2ZQ, 2ZR, 2ZS, 2ZT, 2ZU, 2ZV, 2ZW, 2ZX, 2ZY, 2ZZ, 3AA, 3AB, 3AC, 3AD, 3AE, 3AF, 3AG, 3AH, 3AI, 3AJ, 3AK, 3AL, 3AM, 3AN, 3AO, 3AP, 3AQ, 3AR, 3AS, 3AT, 3AU, 3AV, 3AW, 3AX, 3AY, 3AZ, 3BA, 3BB, 3BC, 3BD, 3BE, 3BF, 3BG, 3BH, 3BI, 3BJ, 3BK, 3BL, 3BM, 3BN, 3BO, 3BP, 3BQ, 3BR, 3BS, 3BT, 3BU, 3BV, 3BW, 3BX, 3BY, 3BZ, 3CA, 3CB, 3CC, 3CD, 3CE, 3CF, 3CG, 3CH, 3CI, 3CJ, 3CK, 3CL, 3CM, 3CN, 3CO, 3CP, 3CQ, 3CR, 3CS, 3CT, 3CU, 3CV, 3CW, 3CX, 3CY, 3CZ, 3DA, 3DB, 3DC, 3DD, 3DE, 3DF, 3DG, 3DH, 3DI, 3DJ, 3DK, 3DL, 3DM, 3DN, 3DO, 3DP, 3DQ, 3DR, 3DS, 3DT, 3DU, 3DV, 3DW, 3DX, 3DY, 3DZ, 3EA, 3EB, 3EC, 3ED, 3EE, 3EF, 3EG, 3EH, 3EI, 3EJ, 3EK, 3EL, 3EM, 3EN, 3EO, 3EP, 3EQ, 3ER, 3ES, 3ET, 3EU, 3EV, 3EW, 3EX, 3EY, 3EZ, 3FA, 3FB, 3FC, 3FD, 3FE, 3FF, 3FG, 3FH, 3FI, 3FJ, 3FK, 3FL, 3FM, 3FN, 3FO, 3FP, 3FQ, 3FR, 3FS, 3FT, 3FU, 3FV, 3FW, 3FX, 3FY, 3FZ, 3GA, 3GB, 3GC, 3GD, 3GE, 3GF, 3GG, 3GH, 3GI, 3GJ, 3GK, 3GL, 3GM, 3GN, 3GO, 3GP, 3GQ, 3GR, 3GS, 3GT, 3GU, 3GV, 3GW, 3GX, 3GY, 3GZ, 3HA, 3HB, 3HC, 3HD, 3HE, 3HF, 3HG, 3HH, 3HI, 3HJ, 3HK, 3HL, 3HM, 3HN, 3HO, 3HP, 3HQ, 3HR, 3HS, 3HT, 3HU, 3HV, 3HW, 3HX, 3HY, 3HZ, 3IA, 3IB, 3IC, 3ID, 3IE, 3IF, 3IG, 3IH, 3II, 3IJ, 3IK, 3IL, 3IM, 3IN, 3IO, 3IP, 3IQ, 3IR, 3IS, 3IT, 3IU, 3IV, 3IW, 3IX, 3IY, 3IZ, 3JA, 3JB, 3JC, 3JD, 3JE, 3JF, 3JG, 3JH, 3JI, 3JJ, 3JK, 3JL, 3JM, 3JN, 3JO, 3JP, 3JQ, 3JR, 3JS, 3JT, 3JU, 3JV, 3JW, 3JX, 3JY, 3JZ, 3KA, 3KB, 3KC, 3KD, 3KE, 3KF, 3KG, 3KH, 3KI, 3KJ, 3KK, 3KL, 3KM, 3KN, 3KO, 3KP, 3KQ, 3KR, 3KS, 3KT, 3KU, 3KV, 3KW, 3KX, 3KY, 3KZ, 3LA, 3LB, 3LC, 3LD, 3LE, 3LF, 3LG, 3LH, 3LI, 3LJ, 3LK, 3LL, 3LM, 3LN, 3LO, 3LP, 3LQ, 3LR, 3LS, 3LT, 3LU, 3LV, 3LW, 3LX, 3LY, 3LZ, 3MA, 3MB, 3MC, 3MD, 3ME, 3MF, 3MG, 3MH, 3MI, 3MJ, 3MK, 3ML, 3MN, 3MO, 3MP, 3MQ, 3MR, 3MS, 3MT, 3MU, 3MV, 3MW, 3MX, 3MY, 3MZ, 3NA, 3NB, 3NC, 3ND, 3NE, 3NF, 3NG, 3NH, 3NI, 3NJ, 3NK, 3NL, 3NM, 3NO, 3NP, 3NQ, 3NR, 3NS, 3NT, 3NU, 3NV, 3NW, 3NX, 3NY, 3NZ, 3OA, 3OB, 3OC, 3OD, 3OE, 3OF, 3OG, 3OH, 3OI, 3OJ, 3OK, 3OL, 3OM, 3ON, 3OO, 3OP, 3OQ, 3OR, 3OS, 3OT, 3OU, 3OV, 3OW, 3OX, 3OY, 3OZ, 3PA, 3PB, 3PC, 3PD, 3PE, 3PF, 3PG, 3PH, 3PI, 3PJ, 3PK, 3PL, 3PM, 3PN, 3PO, 3PP, 3PQ, 3PR, 3PS, 3PT, 3PU, 3PV, 3PW, 3PX, 3PY, 3PZ, 3QA, 3QB, 3QC, 3QD, 3QE, 3QF, 3QG, 3QH, 3QI, 3QJ, 3QK, 3QL, 3QM, 3QN, 3QO, 3QP, 3QQ, 3QR, 3QS, 3QT, 3QU, 3QV, 3QW, 3QX, 3QY, 3QZ, 3RA, 3RB, 3RC, 3RD, 3RE, 3RF, 3RG, 3RH, 3RI, 3RJ, 3RK, 3RL, 3RM, 3RN, 3RO, 3RP, 3RQ, 3RR, 3RS, 3RT, 3RU, 3RV, 3RW, 3RX, 3RY, 3RZ, 3SA, 3SB, 3SC, 3SD, 3SE, 3SF, 3SG, 3SH, 3SI, 3SJ, 3SK, 3SL, 3SM, 3SN, 3SO, 3SP, 3SQ, 3SR, 3SS, 3ST, 3SU, 3SV, 3SW, 3SX, 3SY, 3SZ, 3TA, 3TB, 3TC, 3TD, 3TE, 3TF, 3TG, 3TH, 3TI, 3TJ, 3TK, 3TL, 3TM, 3TN, 3TO, 3TP, 3TQ, 3TR, 3TS, 3TT, 3TU, 3TV, 3TW, 3TX, 3TY, 3TZ, 3UA, 3UB, 3UC, 3UD, 3UE, 3UF, 3UG, 3UH, 3UI, 3UJ, 3UK, 3UL, 3UM, 3UN, 3UO, 3UP, 3UQ, 3UR, 3US, 3UT, 3UU, 3UV, 3UW, 3UX, 3UY, 3UZ, 3VA, 3VB, 3VC, 3VD, 3VE, 3VF, 3VG, 3VH, 3VI, 3VJ, 3VK, 3VL, 3VM, 3VN, 3VO, 3VP, 3VQ, 3VR, 3VS, 3VT, 3VU, 3VV, 3VW, 3VX, 3VY, 3VZ, 3WA, 3WB, 3WC, 3WD, 3WE, 3WF, 3WG, 3WH, 3WI, 3WJ, 3WK, 3WL, 3WM, 3WN, 3WO, 3WP, 3WQ, 3WR, 3WS, 3WT, 3WU, 3WV, 3WW, 3WX, 3WY, 3WZ, 3XA, 3XB, 3XC, 3XD, 3XE, 3XF, 3XG, 3XH, 3XI, 3XJ, 3XK, 3XL, 3XM, 3XN, 3XO, 3XP, 3XQ, 3XR, 3XS, 3XT, 3XU, 3XV, 3XW, 3XX, 3XY, 3XZ, 3YA, 3YB, 3YC, 3YD, 3YE, 3YF, 3YG, 3YH, 3YI, 3YJ, 3YK, 3YL, 3YM, 3YN, 3YO, 3YP, 3YQ, 3YR, 3YS, 3YT, 3YU, 3YV, 3YW, 3YX, 3YY, 3YZ, 3ZA, 3ZB, 3ZC, 3ZD, 3ZE, 3ZF, 3ZG, 3ZH, 3ZI, 3ZJ, 3ZK, 3ZL, 3ZM, 3ZN, 3ZO, 3ZP, 3ZQ, 3ZR, 3ZS, 3ZT, 3ZU, 3ZV, 3ZW, 3ZX, 3ZY, 3ZZ, 4AA, 4AB, 4AC, 4AD, 4AE, 4AF, 4AG, 4AH, 4AI, 4AJ, 4AK, 4AL, 4AM, 4AN, 4AO, 4AP, 4AQ, 4AR, 4AS, 4AT, 4AU, 4AV, 4AW, 4AX, 4AY, 4AZ, 4BA, 4BB, 4BC, 4BD, 4BE, 4BF, 4BG, 4BH, 4BI, 4BJ, 4BK, 4BL, 4BM, 4BN, 4BO, 4BP, 4BQ, 4BR, 4BS, 4BT, 4BU, 4BV, 4BW, 4BX, 4BY, 4BZ, 4CA, 4CB, 4CC, 4CD, 4CE, 4CF, 4CG, 4CH, 4CI, 4CJ, 4CK, 4CL, 4CM, 4CN, 4CO, 4CP, 4CQ, 4CR, 4CS, 4CT, 4CU, 4CV, 4CW, 4CX, 4CY, 4CZ, 4DA, 4DB, 4DC, 4DD, 4DE, 4DF, 4DG, 4DH, 4DI, 4DJ, 4DK, 4DL, 4DM, 4DN, 4DO, 4DP, 4DQ, 4DR, 4DS, 4DT, 4DU, 4DV, 4DW, 4DX, 4DY, 4DZ, 4EA, 4EB, 4EC, 4ED, 4EE, 4EF, 4EG, 4EH, 4EI, 4EJ, 4EK, 4EL, 4EM, 4EN, 4EO, 4EP, 4EQ, 4ER, 4ES, 4ET, 4EU, 4EV, 4EW, 4EX, 4EY, 4EZ, 4FA, 4FB, 4FC, 4FD, 4FE, 4FF, 4FG, 4FH, 4FI, 4FJ, 4FK, 4FL, 4FM, 4FN, 4FO, 4FP, 4FQ, 4FR, 4FS, 4FT, 4FU, 4FV, 4FW, 4FX, 4FY, 4FZ, 4GA, 4GB, 4GC, 4GD, 4GE, 4GF, 4GG, 4GH, 4GI, 4GJ, 4GK, 4GL, 4GM, 4GN, 4GO, 4GP, 4GQ, 4GR, 4GS, 4GT, 4GU, 4GV, 4GW, 4GX, 4GY, 4GZ, 4HA, 4HB, 4HC, 4HD, 4HE, 4HF, 4HG, 4HH, 4HI, 4HJ, 4HK, 4HL, 4HM, 4HN, 4HO, 4HP, 4HQ, 4HR, 4HS, 4HT, 4HU, 4HV, 4HW, 4HX, 4HY, 4HZ, 4IA, 4IB, 4IC, 4ID, 4IE, 4IF, 4IG, 4IH, 4II, 4IJ, 4IK, 4IL, 4IM, 4IN, 4IO, 4IP, 4IQ, 4IR, 4IS, 4IT, 4IU, 4IV, 4IW, 4IX, 4IY, 4IZ, 4JA, 4JB, 4JC, 4JD, 4JE, 4JF, 4JG, 4JH, 4JI, 4JJ, 4JK, 4JL, 4JM, 4JN, 4JO, 4JP, 4JQ, 4JR, 4JS, 4JT, 4JU, 4JV, 4JW, 4JX, 4JY, 4JZ, 4KA, 4KB, 4KC, 4KD, 4KE, 4KF, 4KG, 4KH, 4KI, 4KJ, 4KK, 4KL, 4KM, 4KN, 4KO, 4KP, 4KQ, 4KR, 4KS, 4KT, 4KU, 4KV, 4KW, 4KX, 4KY, 4KZ, 4LA, 4LB, 4LC, 4LD, 4LE, 4LF, 4LG, 4LH, 4LI, 4LJ, 4LK, 4LL, 4LM, 4LN, 4LO, 4LP, 4LQ, 4LR, 4LS, 4LT, 4LU, 4LV, 4LW, 4LX, 4LY, 4LZ, 4MA, 4MB, 4MC, 4MD, 4ME, 4MF, 4MG, 4MH, 4MI, 4MJ, 4MK, 4ML, 4MN, 4MO, 4MP, 4MQ, 4MR, 4MS, 4MT, 4MU, 4MV, 4MW, 4MX, 4MY, 4MZ, 4NA, 4NB, 4NC, 4ND, 4NE, 4NF, 4NG, 4NH, 4NI, 4NJ, 4NK, 4NL, 4NM, 4NO, 4NP, 4NQ, 4NR, 4NS, 4NT, 4NU, 4NV, 4NW, 4NX, 4NY, 4NZ, 4OA, 4OB, 4OC, 4OD, 4OE, 4OF, 4OG, 4OH, 4OI, 4OJ, 4OK, 4OL, 4OM, 4ON, 4OO, 4OP, 4OQ, 4OR, 4OS, 4OT, 4OU, 4OV, 4OW, 4OX, 4OY, 4OZ, 4PA, 4PB, 4PC, 4PD, 4PE, 4PF, 4PG, 4PH, 4PI, 4PJ, 4PK, 4PL, 4PM, 4PN, 4PO, 4PP, 4PQ, 4PR, 4PS, 4PT, 4PU, 4PV, 4PW, 4PX, 4PY, 4PZ, 4QA, 4QB, 4QC, 4QD, 4QE, 4QF, 4QG, 4QH, 4QI, 4QJ, 4QK, 4QL, 4QM, 4QN, 4QO, 4QP, 4QQ, 4QR, 4QS, 4QT, 4QU, 4QV, 4QW, 4QX, 4QY, 4QZ, 4RA, 4RB, 4RC, 4RD, 4RE, 4RF, 4RG, 4RH, 4RI, 4RJ, 4RK, 4RL, 4RM, 4RN, 4RO, 4RP, 4RQ, 4RR, 4RS, 4RT, 4RU, 4RV, 4RW, 4RX, 4RY, 4RZ, 4SA, 4SB, 4SC, 4SD, 4SE, 4SF, 4SG, 4SH, 4SI, 4SJ, 4SK, 4SL, 4SM, 4SN, 4SO, 4SP, 4SQ, 4SR, 4SS, 4ST, 4SU, 4SV, 4SW, 4SX, 4SY, 4SZ, 4TA, 4TB, 4TC, 4TD, 4TE, 4TF, 4TG, 4TH, 4TI, 4TJ, 4TK, 4TL, 4TM, 4TN, 4TO, 4TP, 4TQ, 4TR, 4TS, 4TT, 4TU, 4TV, 4TW, 4TX, 4TY, 4TZ, 4UA, 4UB, 4UC, 4UD, 4UE, 4UF, 4UG, 4UH, 4UI, 4UJ, 4UK, 4UL, 4UM, 4UN, 4UO, 4UP, 4UQ, 4UR, 4US, 4UT, 4UU, 4UV, 4UW, 4UX, 4UY, 4UZ, 4VA, 4VB, 4VC, 4VD, 4VE, 4VF, 4VG, 4VH, 4VI, 4VJ, 4VK, 4VL, 4VM, 4VN, 4VO, 4VP, 4VQ, 4VR, 4VS, 4VT, 4VU, 4VV, 4VW, 4VX, 4VY, 4VZ, 4WA, 4WB, 4WC, 4WD, 4WE, 4WF, 4WG, 4WH, 4WI, 4WJ, 4WK, 4WL, 4WM, 4WN, 4WO, 4WP, 4WQ, 4WR, 4WS, 4WT, 4WU, 4WV, 4WW, 4WX, 4WY, 4WZ, 4XA, 4XB, 4XC, 4XD, 4XE, 4XF, 4XG, 4XH, 4XI, 4XJ, 4XK, 4XL, 4XM, 4XN, 4XO, 4XP, 4XQ, 4XR, 4XS, 4XT, 4XU, 4XV, 4XW, 4XX, 4XY, 4XZ, 4YA, 4YB, 4YC, 4YD, 4YE, 4YF, 4YG, 4YH, 4YI, 4YJ, 4YK, 4YL, 4YM, 4YN, 4YO, 4YP, 4YQ, 4YR, 4YS, 4YT, 4YU, 4YV, 4YW, 4YX, 4YY, 4YZ, 4ZA, 4ZB, 4ZC, 4ZD, 4ZE, 4ZF, 4ZG, 4ZH, 4ZI, 4ZJ, 4ZK, 4ZL, 4ZM, 4ZN, 4ZO, 4ZP, 4ZQ, 4ZR, 4ZS, 4ZT, 4ZU, 4ZV, 4ZW, 4ZX, 4ZY, 4ZZ, 5AA, 5AB, 5AC, 5AD, 5AE, 5AF, 5AG, 5AH, 5AI, 5AJ, 5AK, 5AL, 5AM, 5AN, 5AO, 5AP, 5AQ, 5AR, 5AS, 5AT, 5AU, 5AV, 5AW, 5AX, 5AY, 5AZ, 5BA, 5BB, 5BC, 5BD, 5BE, 5BF, 5BG, 5BH, 5BI, 5BJ, 5BK, 5BL, 5BM, 5BN, 5BO, 5BP, 5BQ, 5BR, 5BS, 5BT, 5BU, 5BV, 5BW, 5BX, 5BY, 5BZ, 5CA, 5CB, 5CC, 5CD, 5CE, 5CF, 5CG, 5CH, 5CI, 5CJ, 5CK, 5CL, 5CM, 5CN, 5CO, 5CP, 5CQ, 5CR, 5CS, 5CT, 5CU, 5CV, 5CW, 5CX, 5CY, 5CZ, 5DA, 5DB, 5DC, 5DD, 5DE, 5DF, 5DG, 5DH, 5DI, 5DJ, 5DK, 5DL, 5DM, 5DN, 5DO, 5DP, 5DQ, 5DR, 5DS, 5DT, 5DU, 5DV, 5DW, 5DX, 5DY, 5DZ, 5EA, 5EB, 5EC, 5ED, 5EE, 5EF, 5EG, 5EH, 5EI, 5EJ, 5EK, 5EL, 5EM, 5EN, 5EO, 5EP, 5EQ, 5ER, 5ES, 5ET, 5EU, 5EV, 5EW, 5EX, 5EY, 5EZ, 5FA, 5FB, 5FC, 5FD, 5FE, 5FF, 5FG, 5FH, 5FI, 5FJ, 5FK, 5FL, 5FM, 5FN, 5FO, 5FP, 5FQ, 5FR, 5FS, 5FT, 5FU, 5FV, 5FW, 5FX, 5FY, 5FZ, 5GA, 5GB, 5GC, 5GD, 5GE, 5GF, 5GG, 5GH, 5																									

Figure 32. (Continued.)

ID	Instrument Type(s)	Physical Parameter (PP) Description	Link to Objectives	Units	PP Range	PP Resolution	PP Altitude Range	PP Altitude Resolution	PP Coord. System	PP Local Time (LT) Range	PP Long. Res. Range	PP Lat. Res. Range	PP Seasonal Range	PP Seasonal Resolution	Observable Quantity (OQ)				Angular Azimuth (X) Range	Polar (Y) Resolution	Energy/ Wavelength Frequency Range	Resolution (VIS, NIR, or UV)	Mass Range	Mass Resolution																																																																																																																																																																																																																																																																																																																																																																																																																																																																																																																																																																																																																																																																																																																																																																																																																																																																																																																																																																																																																																																																																																																																																																																																																																																																																																																														
															PP Description	PP Resolution	PP Altitude Range	PP Altitude Resolution							PP Coord. System	PP Local Time (LT) Range	PP Long. Res. Range	PP Lat. Res. Range	PP Seasonal Range	PP Seasonal Resolution	PP Description	PP Resolution	PP Altitude Range	PP Altitude Resolution	PP Coord. System	PP Local Time (LT) Range	PP Long. Res. Range	PP Lat. Res. Range	PP Seasonal Range	PP Seasonal Resolution	PP Description	PP Resolution	PP Altitude Range	PP Altitude Resolution	PP Coord. System	PP Local Time (LT) Range	PP Long. Res. Range	PP Lat. Res. Range	PP Seasonal Range	PP Seasonal Resolution	PP Description	PP Resolution	PP Altitude Range	PP Altitude Resolution	PP Coord. System	PP Local Time (LT) Range	PP Long. Res. Range	PP Lat. Res. Range	PP Seasonal Range	PP Seasonal Resolution	PP Description	PP Resolution	PP Altitude Range	PP Altitude Resolution	PP Coord. System	PP Local Time (LT) Range	PP Long. Res. Range	PP Lat. Res. Range	PP Seasonal Range	PP Seasonal Resolution	PP Description	PP Resolution	PP Altitude Range	PP Altitude Resolution	PP Coord. System	PP Local Time (LT) Range	PP Long. Res. Range	PP Lat. Res. Range	PP Seasonal Range	PP Seasonal Resolution	PP Description	PP Resolution	PP Altitude Range	PP Altitude Resolution	PP Coord. System	PP Local Time (LT) Range	PP Long. Res. Range	PP Lat. Res. Range	PP Seasonal Range	PP Seasonal Resolution	PP Description	PP Resolution	PP Altitude Range	PP Altitude Resolution	PP Coord. System	PP Local Time (LT) Range	PP Long. Res. Range	PP Lat. Res. Range	PP Seasonal Range	PP Seasonal Resolution	PP Description	PP Resolution	PP Altitude Range	PP Altitude Resolution	PP Coord. System	PP Local Time (LT) Range	PP Long. Res. Range	PP Lat. Res. Range	PP Seasonal Range	PP Seasonal Resolution	PP Description	PP Resolution	PP Altitude Range	PP Altitude Resolution	PP Coord. System	PP Local Time (LT) Range	PP Long. Res. Range	PP Lat. Res. Range	PP Seasonal Range	PP Seasonal Resolution	PP Description	PP Resolution	PP Altitude Range	PP Altitude Resolution	PP Coord. System	PP Local Time (LT) Range	PP Long. Res. Range	PP Lat. Res. Range	PP Seasonal Range	PP Seasonal Resolution	PP Description	PP Resolution	PP Altitude Range	PP Altitude Resolution	PP Coord. System	PP Local Time (LT) Range	PP Long. Res. Range	PP Lat. Res. Range	PP Seasonal Range	PP Seasonal Resolution	PP Description	PP Resolution	PP Altitude Range	PP Altitude Resolution	PP Coord. System	PP Local Time (LT) Range	PP Long. Res. Range	PP Lat. Res. Range	PP Seasonal Range	PP Seasonal Resolution	PP Description	PP Resolution	PP Altitude Range	PP Altitude Resolution	PP Coord. System	PP Local Time (LT) Range	PP Long. Res. Range	PP Lat. Res. Range	PP Seasonal Range	PP Seasonal Resolution	PP Description	PP Resolution	PP Altitude Range	PP Altitude Resolution	PP Coord. System	PP Local Time (LT) Range	PP Long. Res. Range	PP Lat. Res. Range	PP Seasonal Range	PP Seasonal Resolution	PP Description	PP Resolution	PP Altitude Range	PP Altitude Resolution	PP Coord. System	PP Local Time (LT) Range	PP Long. Res. Range	PP Lat. Res. Range	PP Seasonal Range	PP Seasonal Resolution	PP Description	PP Resolution	PP Altitude Range	PP Altitude Resolution	PP Coord. System	PP Local Time (LT) Range	PP Long. Res. Range	PP Lat. Res. Range	PP Seasonal Range	PP Seasonal Resolution	PP Description	PP Resolution	PP Altitude Range	PP Altitude Resolution	PP Coord. System	PP Local Time (LT) Range	PP Long. Res. Range	PP Lat. Res. Range	PP Seasonal Range	PP Seasonal Resolution	PP Description	PP Resolution	PP Altitude Range	PP Altitude Resolution	PP Coord. System	PP Local Time (LT) Range	PP Long. Res. Range	PP Lat. Res. Range	PP Seasonal Range	PP Seasonal Resolution	PP Description	PP Resolution	PP Altitude Range	PP Altitude Resolution	PP Coord. System	PP Local Time (LT) Range	PP Long. Res. Range	PP Lat. Res. Range	PP Seasonal Range	PP Seasonal Resolution	PP Description	PP Resolution	PP Altitude Range	PP Altitude Resolution	PP Coord. System	PP Local Time (LT) Range	PP Long. Res. Range	PP Lat. Res. Range	PP Seasonal Range	PP Seasonal Resolution	PP Description	PP Resolution	PP Altitude Range	PP Altitude Resolution	PP Coord. System	PP Local Time (LT) Range	PP Long. Res. Range	PP Lat. Res. Range	PP Seasonal Range	PP Seasonal Resolution	PP Description	PP Resolution	PP Altitude Range	PP Altitude Resolution	PP Coord. System	PP Local Time (LT) Range	PP Long. Res. Range	PP Lat. Res. Range	PP Seasonal Range	PP Seasonal Resolution	PP Description	PP Resolution	PP Altitude Range	PP Altitude Resolution	PP Coord. System	PP Local Time (LT) Range	PP Long. Res. Range	PP Lat. Res. Range	PP Seasonal Range	PP Seasonal Resolution	PP Description	PP Resolution	PP Altitude Range	PP Altitude Resolution	PP Coord. System	PP Local Time (LT) Range	PP Long. Res. Range	PP Lat. Res. Range	PP Seasonal Range	PP Seasonal Resolution	PP Description	PP Resolution	PP Altitude Range	PP Altitude Resolution	PP Coord. System	PP Local Time (LT) Range	PP Long. Res. Range	PP Lat. Res. Range	PP Seasonal Range	PP Seasonal Resolution	PP Description	PP Resolution	PP Altitude Range	PP Altitude Resolution	PP Coord. System	PP Local Time (LT) Range	PP Long. Res. Range	PP Lat. Res. Range	PP Seasonal Range	PP Seasonal Resolution	PP Description	PP Resolution	PP Altitude Range	PP Altitude Resolution	PP Coord. System	PP Local Time (LT) Range	PP Long. Res. Range	PP Lat. Res. Range	PP Seasonal Range	PP Seasonal Resolution	PP Description	PP Resolution	PP Altitude Range	PP Altitude Resolution	PP Coord. System	PP Local Time (LT) Range	PP Long. Res. Range	PP Lat. Res. Range	PP Seasonal Range	PP Seasonal Resolution	PP Description	PP Resolution	PP Altitude Range	PP Altitude Resolution	PP Coord. System	PP Local Time (LT) Range	PP Long. Res. Range	PP Lat. Res. Range	PP Seasonal Range	PP Seasonal Resolution	PP Description	PP Resolution	PP Altitude Range	PP Altitude Resolution	PP Coord. System	PP Local Time (LT) Range	PP Long. Res. Range	PP Lat. Res. Range	PP Seasonal Range	PP Seasonal Resolution	PP Description	PP Resolution	PP Altitude Range	PP Altitude Resolution	PP Coord. System	PP Local Time (LT) Range	PP Long. Res. Range	PP Lat. Res. Range	PP Seasonal Range	PP Seasonal Resolution	PP Description	PP Resolution	PP Altitude Range	PP Altitude Resolution	PP Coord. System	PP Local Time (LT) Range	PP Long. Res. Range	PP Lat. Res. Range	PP Seasonal Range	PP Seasonal Resolution	PP Description	PP Resolution	PP Altitude Range	PP Altitude Resolution	PP Coord. System	PP Local Time (LT) Range	PP Long. Res. Range	PP Lat. Res. Range	PP Seasonal Range	PP Seasonal Resolution	PP Description	PP Resolution	PP Altitude Range	PP Altitude Resolution	PP Coord. System	PP Local Time (LT) Range	PP Long. Res. Range	PP Lat. Res. Range	PP Seasonal Range	PP Seasonal Resolution	PP Description	PP Resolution	PP Altitude Range	PP Altitude Resolution	PP Coord. System	PP Local Time (LT) Range	PP Long. Res. Range	PP Lat. Res. Range	PP Seasonal Range	PP Seasonal Resolution	PP Description	PP Resolution	PP Altitude Range	PP Altitude Resolution	PP Coord. System	PP Local Time (LT) Range	PP Long. Res. Range	PP Lat. Res. Range	PP Seasonal Range	PP Seasonal Resolution	PP Description	PP Resolution	PP Altitude Range	PP Altitude Resolution	PP Coord. System	PP Local Time (LT) Range	PP Long. Res. Range	PP Lat. Res. Range	PP Seasonal Range	PP Seasonal Resolution	PP Description	PP Resolution	PP Altitude Range	PP Altitude Resolution	PP Coord. System	PP Local Time (LT) Range	PP Long. Res. Range	PP Lat. Res. Range	PP Seasonal Range	PP Seasonal Resolution	PP Description	PP Resolution	PP Altitude Range	PP Altitude Resolution	PP Coord. System	PP Local Time (LT) Range	PP Long. Res. Range	PP Lat. Res. Range	PP Seasonal Range	PP Seasonal Resolution	PP Description	PP Resolution	PP Altitude Range	PP Altitude Resolution	PP Coord. System	PP Local Time (LT) Range	PP Long. Res. Range	PP Lat. Res. Range	PP Seasonal Range	PP Seasonal Resolution	PP Description	PP Resolution	PP Altitude Range	PP Altitude Resolution	PP Coord. System	PP Local Time (LT) Range	PP Long. Res. Range	PP Lat. Res. Range	PP Seasonal Range	PP Seasonal Resolution	PP Description	PP Resolution	PP Altitude Range	PP Altitude Resolution	PP Coord. System	PP Local Time (LT) Range	PP Long. Res. Range	PP Lat. Res. Range	PP Seasonal Range	PP Seasonal Resolution	PP Description	PP Resolution	PP Altitude Range	PP Altitude Resolution	PP Coord. System	PP Local Time (LT) Range	PP Long. Res. Range	PP Lat. Res. Range	PP Seasonal Range	PP Seasonal Resolution	PP Description	PP Resolution	PP Altitude Range	PP Altitude Resolution	PP Coord. System	PP Local Time (LT) Range	PP Long. Res. Range	PP Lat. Res. Range	PP Seasonal Range	PP Seasonal Resolution	PP Description	PP Resolution	PP Altitude Range	PP Altitude Resolution	PP Coord. System	PP Local Time (LT) Range	PP Long. Res. Range	PP Lat. Res. Range	PP Seasonal Range	PP Seasonal Resolution	PP Description	PP Resolution	PP Altitude Range	PP Altitude Resolution	PP Coord. System	PP Local Time (LT) Range	PP Long. Res. Range	PP Lat. Res. Range	PP Seasonal Range	PP Seasonal Resolution	PP Description	PP Resolution	PP Altitude Range	PP Altitude Resolution	PP Coord. System	PP Local Time (LT) Range	PP Long. Res. Range	PP Lat. Res. Range	PP Seasonal Range	PP Seasonal Resolution	PP Description	PP Resolution	PP Altitude Range	PP Altitude Resolution	PP Coord. System	PP Local Time (LT) Range	PP Long. Res. Range	PP Lat. Res. Range	PP Seasonal Range	PP Seasonal Resolution	PP Description	PP Resolution	PP Altitude Range	PP Altitude Resolution	PP Coord. System	PP Local Time (LT) Range	PP Long. Res. Range	PP Lat. Res. Range	PP Seasonal Range	PP Seasonal Resolution	PP Description	PP Resolution	PP Altitude Range	PP Altitude Resolution	PP Coord. System	PP Local Time (LT) Range	PP Long. Res. Range	PP Lat. Res. Range	PP Seasonal Range	PP Seasonal Resolution	PP Description	PP Resolution	PP Altitude Range	PP Altitude Resolution	PP Coord. System	PP Local Time (LT) Range	PP Long. Res. Range	PP Lat. Res. Range	PP Seasonal Range	PP Seasonal Resolution	PP Description	PP Resolution	PP Altitude Range	PP Altitude Resolution	PP Coord. System	PP Local Time (LT) Range	PP Long. Res. Range	PP Lat. Res. Range	PP Seasonal Range	PP Seasonal Resolution	PP Description	PP Resolution	PP Altitude Range	PP Altitude Resolution	PP Coord. System	PP Local Time (LT) Range	PP Long. Res. Range	PP Lat. Res. Range	PP Seasonal Range	PP Seasonal Resolution	PP Description	PP Resolution	PP Altitude Range	PP Altitude Resolution	PP Coord. System	PP Local Time (LT) Range	PP Long. Res. Range	PP Lat. Res. Range	PP Seasonal Range	PP Seasonal Resolution	PP Description	PP Resolution	PP Altitude Range	PP Altitude Resolution	PP Coord. System	PP Local Time (LT) Range	PP Long. Res. Range	PP Lat. Res. Range	PP Seasonal Range	PP Seasonal Resolution	PP Description	PP Resolution	PP Altitude Range	PP Altitude Resolution	PP Coord. System	PP Local Time (LT) Range	PP Long. Res. Range	PP Lat. Res. Range	PP Seasonal Range	PP Seasonal Resolution	PP Description	PP Resolution	PP Altitude Range	PP Altitude Resolution	PP Coord. System	PP Local Time (LT) Range	PP Long. Res. Range	PP Lat. Res. Range	PP Seasonal Range	PP Seasonal Resolution	PP Description	PP Resolution	PP Altitude Range	PP Altitude Resolution	PP Coord. System	PP Local Time (LT) Range	PP Long. Res. Range	PP Lat. Res. Range	PP Seasonal Range	PP Seasonal Resolution	PP Description	PP Resolution	PP Altitude Range	PP Altitude Resolution	PP Coord. System	PP Local Time (LT) Range	PP Long. Res. Range	PP Lat. Res. Range	PP Seasonal Range	PP Seasonal Resolution	PP Description	PP Resolution	PP Altitude Range	PP Altitude Resolution	PP Coord. System	PP Local Time (LT) Range	PP Long. Res. Range	PP Lat. Res. Range	PP Seasonal Range	PP Seasonal Resolution	PP Description	PP Resolution	PP Altitude Range	PP Altitude Resolution	PP Coord. System	PP Local Time (LT) Range	PP Long. Res. Range	PP Lat. Res. Range	PP Seasonal Range	PP Seasonal Resolution	PP Description	PP Resolution	PP Altitude Range	PP Altitude Resolution	PP Coord. System	PP Local Time (LT) Range	PP Long. Res. Range	PP Lat. Res. Range	PP Seasonal Range	PP Seasonal Resolution	PP Description	PP Resolution	PP Altitude Range	PP Altitude Resolution	PP Coord. System	PP Local Time (LT) Range	PP Long. Res. Range	PP Lat. Res. Range	PP Seasonal Range	PP Seasonal Resolution	PP Description	PP Resolution	PP Altitude Range	PP Altitude Resolution	PP Coord. System	PP Local Time (LT) Range	PP Long. Res. Range	PP Lat. Res. Range	PP Seasonal Range	PP Seasonal Resolution	PP Description	PP Resolution	PP Altitude Range	PP Altitude Resolution	PP Coord. System	PP Local Time (LT) Range	PP Long. Res. Range	PP Lat. Res. Range	PP Seasonal Range	PP Seasonal Resolution	PP Description	PP Resolution	PP Altitude Range	PP Altitude Resolution	PP Coord. System	PP Local Time (LT) Range	PP Long. Res. Range	PP Lat. Res. Range	PP Seasonal Range	PP Seasonal Resolution	PP Description	PP Resolution	PP Altitude Range	PP Altitude Resolution	PP Coord. System	PP Local Time (LT) Range	PP Long. Res. Range	PP Lat. Res. Range	PP Seasonal Range	PP Seasonal Resolution	PP Description	PP Resolution	PP Altitude Range	PP Altitude Resolution	PP Coord. System	PP Local Time (LT) Range	PP Long. Res. Range	PP Lat. Res. Range	PP Seasonal Range	PP Seasonal Resolution	PP Description	PP Resolution	PP Altitude Range	PP Altitude Resolution	PP Coord. System	PP Local Time (LT) Range	PP Long. Res. Range	PP Lat. Res. Range	PP Seasonal Range	PP Seasonal Resolution	PP Description	PP Resolution	PP Altitude Range	PP Altitude Resolution	PP Coord. System	PP Local Time (LT) Range	PP Long. Res. Range	PP Lat. Res. Range	PP Seasonal Range	PP Seasonal Resolution	PP Description	PP Resolution	PP Altitude Range	PP Altitude Resolution	PP Coord. System	PP Local Time (LT) Range	PP Long. Res. Range	PP Lat. Res. Range	PP Seasonal Range	PP Seasonal Resolution	PP Description	PP Resolution	PP Altitude Range	PP Altitude Resolution	PP Coord. System	PP Local Time (LT) Range	PP Long. Res. Range	PP Lat. Res. Range	PP Seasonal Range	PP Seasonal Resolution	PP Description	PP Resolution	PP Altitude Range	PP Altitude Resolution	PP Coord. System	PP Local Time (LT) Range	PP Long. Res. Range	PP Lat. Res. Range	PP Seasonal Range	PP Seasonal Resolution	PP Description	PP Resolution	PP Altitude Range	PP Altitude Resolution	PP Coord. System	PP Local Time (LT) Range	PP Long. Res. Range	PP Lat. Res. Range	PP Seasonal Range	PP Seasonal Resolution	PP Description	PP Resolution	PP Altitude Range	PP Altitude Resolution	PP Coord. System	PP Local Time (LT) Range	PP Long. Res. Range	PP Lat. Res. Range	PP Seasonal Range	PP Seasonal Resolution	PP Description	PP Resolution	PP Altitude Range	PP Altitude Resolution	PP Coord. System	PP Local Time (LT) Range	PP Long. Res. Range	PP Lat. Res. Range	PP Seasonal Range	PP Seasonal Resolution	PP Description	PP Resolution	PP Altitude Range	PP Altitude Resolution	PP Coord. System	PP Local Time (LT) Range	PP Long. Res. Range	PP Lat. Res. Range	PP Seasonal Range	PP Seasonal Resolution	PP Description	PP Resolution	PP Altitude Range	PP Altitude Resolution	PP Coord. System	PP Local Time (LT) Range	PP Long. Res. Range	PP Lat. Res. Range	PP Seasonal Range	PP Seasonal Resolution	PP Description	PP Resolution	PP Altitude Range	PP Altitude Resolution	PP Coord. System	PP Local Time (LT) Range	PP Long. Res. Range	PP Lat. Res. Range	PP Seasonal Range	PP Seasonal Resolution	PP Description	PP Resolution	PP Altitude Range	PP Altitude Resolution	PP Coord. System	PP Local Time (LT) Range	PP Long. Res. Range	PP Lat. Res. Range	PP Seasonal Range	PP Seasonal Resolution	PP Description	PP Resolution	PP Altitude Range	PP Altitude Resolution	PP Coord. System	PP Local Time (LT) Range	PP Long. Res. Range	PP Lat. Res. Range	PP Seasonal Range	PP Seasonal Resolution	PP Description	PP Resolution	PP Altitude Range	PP Altitude Resolution	PP Coord. System	PP Local Time (LT) Range	PP Long. Res. Range	PP Lat. Res. Range	PP Seasonal Range	PP Seasonal Resolution	PP Description	PP Resolution	PP Altitude Range	PP Altitude Resolution	PP Coord. System	PP Local Time (LT) Range	PP Long. Res. Range	PP Lat. Res. Range	PP Seasonal Range	PP Seasonal Resolution	PP Description	PP Resolution	PP Altitude Range	PP Altitude Resolution	PP Coord. System	PP Local Time (LT) Range	PP Long. Res. Range	PP Lat. Res. Range	PP Seasonal Range	PP Seasonal Resolution	PP Description	PP Resolution	PP Altitude Range	PP Altitude Resolution	PP Coord. System	PP Local Time (LT) Range	PP Long. Res. Range	PP Lat. Res. Range	PP Seasonal Range	PP Seasonal Resolution	PP Description	PP Resolution	PP Altitude Range	PP Altitude Resolution	PP Coord. System	PP Local Time (LT) Range	PP Long. Res. Range	PP Lat. Res. Range	PP Seasonal Range	PP Seasonal Resolution	PP Description	PP Resolution	PP Altitude Range	PP Altitude Resolution	PP Coord. System	PP Local Time (LT) Range	PP Long. Res. Range	PP Lat. Res. Range	PP Seasonal Range	PP Seasonal Resolution	PP Description	PP Resolution	PP Altitude Range	PP Altitude Resolution	PP Coord. System	PP Local Time (LT) Range	PP Long. Res. Range	PP Lat. Res. Range	PP Seasonal Range	PP Seasonal Resolution	PP Description	PP Resolution	PP Altitude Range	PP Altitude Resolution	PP Coord. System	PP Local Time (LT) Range	PP Long. Res. Range	PP Lat. Res. Range	PP Seasonal Range	PP Seasonal Resolution	PP Description	PP Resolution	PP Altitude Range	PP Altitude Resolution	PP Coord. System	PP Local Time (LT) Range	PP Long. Res. Range	PP Lat. Res. Range	PP Seasonal Range	PP Seasonal Resolution	PP Description	PP Resolution	PP Altitude Range	PP Altitude Resolution	PP Coord. System	PP Local Time (LT) Range	PP Long. Res. Range	PP Lat. Res. Range	PP Seasonal Range	PP Seasonal Resolution	PP Description	PP Resolution	PP Altitude Range	PP Altitude Resolution	PP Coord. System	PP Local Time (LT) Range	PP Long. Res. Range	PP Lat. Res. Range	PP Seasonal Range	PP Seasonal Resolution	PP Description	PP Resolution	PP Altitude Range	PP Altitude Resolution	PP Coord. System	PP Local Time (LT) Range	PP Long. Res. Range	PP Lat. Res. Range	PP Seasonal Range	PP Seasonal Resolution	PP Description	PP Resolution	PP Altitude Range	PP Altitude Resolution	PP Coord. System	PP Local Time (LT) Range	PP Long. Res. Range	PP Lat. Res. Range	PP Seasonal Range	PP Seasonal Resolution	PP Description	PP Resolution	PP Altitude Range	PP Altitude Resolution	PP Coord. System	PP Local Time (LT) Range	PP Long. Res. Range	PP Lat. Res. Range	PP Seasonal Range	PP Seasonal Resolution	PP Description	PP Resolution	PP Altitude Range	PP Altitude Resolution	PP Coord. System	PP Local Time (LT) Range	PP Long. Res. Range	PP Lat. Res. Range	PP Seasonal Range	PP Seasonal Resolution	PP Description	PP Resolution	PP Altitude Range	PP Altitude Resolution	PP Coord. System	PP Local Time (LT) Range	PP Long. Res. Range	PP Lat. Res. Range	PP Seasonal Range	PP Seasonal Resolution	PP Description	PP Resolution	PP Altitude Range	PP Altitude Resolution	PP Coord. System	PP Local Time (LT) Range	PP Long. Res. Range	PP Lat. Res. Range	PP Seasonal Range	PP Seasonal Resolution	PP Description	PP Resolution	PP Altitude Range	PP Altitude Resolution	PP Coord. System	PP Local Time (LT) Range	PP Long. Res. Range	PP Lat. Res. Range	PP Seasonal Range	PP Seasonal Resolution	PP Description	PP Resolution	PP Altitude Range	PP Altitude Resolution	PP Coord. System	PP Local Time (LT) Range	PP Long. Res. Range	PP Lat. Res. Range	PP Seasonal Range	PP Seasonal Resolution	PP Description	PP Resolution	PP Altitude Range	PP Altitude Resolution	PP Coord. System	PP Local Time (LT) Range	PP Long. Res. Range	PP Lat. Res. Range	PP Seasonal Range	PP Seasonal Resolution	PP Description	PP Resolution	PP Altitude Range	PP Altitude Resolution	PP Coord. System	PP Local Time (LT) Range	PP Long. Res. Range	PP Lat. Res. Range	PP Seasonal Range	PP Seasonal Resolution	PP Description	PP Resolution	PP Altitude Range	PP Altitude Resolution	PP Coord. System	PP Local Time (LT) Range	PP Long. Res. Range	PP Lat. Res. Range	PP Seasonal Range	PP Seasonal Resolution	PP Description	PP Resolution	PP Altitude Range	PP Altitude Resolution	PP Coord. System	PP Local Time (LT) Range	PP Long. Res. Range	PP Lat. Res. Range	PP Seasonal Range	PP Seasonal Resolution	PP Description	PP Resolution	PP Altitude Range	PP Altitude Resolution	PP Coord. System	PP Local Time (LT) Range	PP Long. Res. Range	PP Lat. Res. Range	PP Seasonal Range	PP Seasonal Resolution	PP Description	PP Resolution	PP Altitude Range	PP Altitude Resolution	PP Coord. System	PP Local Time (LT) Range	PP Long. Res. Range	PP Lat. Res. Range	PP Seasonal Range	PP Seasonal Resolution	PP Description	PP Resolution	PP Altitude Range	PP Altitude Resolution	PP Coord. System	PP Local Time (LT) Range	PP Long. Res. Range	PP Lat. Res. Range	PP Seasonal Range	PP Seasonal Resolution	PP Description	PP Resolution	PP Altitude Range	PP Altitude Resolution	PP Coord. System	PP Local Time (LT) Range	PP Long. Res. Range	PP Lat. Res. Range	PP Seasonal Range	PP Seasonal Resolution	PP Description	PP Resolution	PP Altitude Range	PP Altitude Resolution	PP Coord. System	PP Local Time (LT) Range	PP Long. Res. Range	PP Lat. Res. Range	PP Seasonal Range	PP Seasonal Resolution	PP Description	PP Resolution	PP Altitude Range	PP Altitude Resolution	PP Coord. System	PP Local Time (LT) Range	PP Long. Res. Range	PP Lat. Res. Range	PP Seasonal Range	PP Seasonal Resolution	PP Description	PP Resolution	PP Altitude Range	PP Altitude Resolution	PP Coord. System	PP Local Time (LT) Range	PP Long. Res. Range	PP Lat. Res. Range	PP Seasonal Range	PP Seasonal Resolution	PP Description	PP Resolution	PP Altitude Range	PP Altitude Resolution	PP Coord. System	PP Local Time (LT) Range	PP Long. Res. Range	PP Lat. Res. Range	PP Seasonal Range	PP Seasonal Resolution	PP Description	PP Resolution	PP Altitude Range	PP Altitude Resolution	PP Coord. System	PP Local Time (LT) Range	PP Long. Res. Range	PP Lat. Res. Range	PP Seasonal Range	PP Seasonal Resolution	PP Description	PP Resolution	PP Altitude Range	PP Altitude Resolution	PP Coord. System	PP Local Time (LT) Range	PP Long. Res. Range	PP Lat. Res. Range	PP Seasonal Range	PP Seasonal Resolution	PP Description	PP Resolution	PP Altitude Range	PP Altitude Resolution	PP Coord. System	PP Local Time (LT) Range	PP Long. Res. Range	PP Lat. Res. Range	PP Seasonal Range	PP Seasonal Resolution	PP Description	PP Resolution	PP Altitude Range	PP Altitude Resolution	PP Coord. System	PP Local Time (LT) Range	PP Long. Res. Range	PP Lat. Res. Range	PP Seasonal Range	PP Seasonal Resolution	PP Description	PP Resolution	PP Altitude Range	PP Altitude Resolution	PP Coord. System	PP Local Time (LT) Range	PP Long. Res. Range	PP Lat. Res. Range	PP Seasonal Range	PP Seasonal Resolution	PP Description	PP Resolution	PP Altitude Range	PP Altitude Resolution	PP Coord. System	PP Local Time (LT) Range	PP Long. Res. Range	PP Lat. Res. Range	PP Seasonal Range	PP Seasonal Resolution	PP Description	PP Resolution	PP Altitude Range	PP Altitude Resolution	PP Coord. System	PP Local Time (LT) Range	PP Long. Res. Range	PP Lat. Res. Range	PP Seasonal Range	PP Seasonal Resolution	PP Description	PP Resolution	PP Altitude Range	PP Altitude Resolution	PP Coord. System	PP Local Time (LT) Range	PP Long. Res. Range	PP Lat. Res. Range	PP Seasonal Range	PP Seasonal Resolution	PP Description	PP Resolution	PP Altitude Range	PP Altitude Resolution	PP Coord. System	PP Local Time (LT) Range	PP Long. Res. Range	PP Lat. Res. Range	PP Seasonal Range	PP Seasonal Resolution	PP Description	PP Resolution	PP Altitude Range	PP Altitude Resolution	PP Coord. System	PP Local Time (LT) Range	PP Long. Res. Range	PP Lat. Res. Range	PP Seasonal Range	PP Seasonal Resolution	PP Description	PP Resolution	PP Altitude Range	PP Altitude Resolution	PP Coord. System	PP Local Time (LT) Range	PP Long. Res. Range	PP Lat. Res. Range	PP Seasonal Range	PP Seasonal Resolution	PP Description	PP Resolution	PP Altitude Range	PP Altitude Resolution	PP Coord. System	PP Local Time (LT) Range	PP Long. Res. Range	PP Lat. Res. Range	PP Seasonal Range	PP Seasonal Resolution	PP Description	PP Resolution	PP Altitude Range	PP Altitude Resolution	PP Coord. System	PP Local Time (LT) Range	PP Long. Res. Range	PP Lat. Res. Range	PP Seasonal Range	PP Seasonal Resolution	PP Description	PP Resolution	PP Altitude Range	PP Altitude Resolution	PP Coord. System	PP Local Time (LT) Range	PP Long. Res. Range	PP Lat. Res. Range	PP Seasonal Range	PP Seasonal Resolution	PP Description	PP Resolution	PP Altitude Range	PP Altitude Resolution	PP Coord. System	PP Local Time (LT) Range	PP Long. Res. Range	PP Lat. Res. Range	PP Seasonal Range	PP Seasonal Resolution	PP Description	PP Resolution

Figure 32. (Continued.)

ID	Instrument Type(s)	Physical Parameter (PP) Description	Link to Objectives	Units	PP Range	PP Resolution	PP Altitude Range	PP Coord. System	PP Local Time Range	PP Long. Range	PP Lat. Range	PP Res. Resolution	PP Cadence	PP Seasonal Range	PP Seasonal Res. Resolution	Separate from physical parameter for remote data.				Angular FOV (X) Range	Azimuth (X) Polar (Y) Resolution	Polar (Y) Resolution	Energy/ Wavelength/ Frequency	Resolution Channels	Mass Range	Mass Res. Resolution
																QO Description	QO Units	QO Dynamic Range	QO Precision	QO SNR	QO Time Resolution					
DIU-3	Thermal infrared spectrometer	Vertical profile of atmospheric temperature	Objectives: I.B. - Essential for monitoring of atmospheric state and collection of long-term climatologies.	Kelvin	10-20 K	10-20 K	0-40 km	PC	0-24 h	180°W - 180°E	85°S - 85°N	2°	30 minutes-300°	5°	5°	Radiance	mW m ⁻² sr ⁻¹ (cm ⁻¹) ⁻¹	0-40 mW m ⁻² sr ⁻¹ (cm ⁻¹) ⁻¹	1%	NER < 0.12 mW m ⁻² sr ⁻¹ (cm ⁻¹) ⁻¹	10 s	270°	0.1°	15 micron CO ₂ band	~50 and 100 channels	N/A
DIU-10	Thermal infrared spectrometer	Vertical profile of dust opacity	Objectives: I.B. - Essential for monitoring of atmospheric state and collection of long-term climatologies.	Per kilometer	10 ⁻⁴ km ⁻¹ to 10 ⁻² km ⁻¹	10 ⁻⁴ km ⁻¹ to 10 ⁻² km ⁻¹	0-40 km	PC	0-24 h	180°W - 180°E	85°S - 85°N	2°	1 sol	0-360°	5°	Radiance	TIR: mW m ⁻² sr ⁻¹ (cm ⁻¹) ⁻¹ ; NIR: W m ⁻² sr ⁻¹ (cm ⁻¹) ⁻¹	0-40 mW m ⁻² sr ⁻¹ (cm ⁻¹) ⁻¹	1%	NER < 0.1 mW m ⁻² sr ⁻¹ (cm ⁻¹) ⁻¹	10 s	270°	0.1°	9 or 22 microns, e.g. 40-400 cm ⁻¹ channels	~50 and 100 channels	N/A
DIU-11	Thermal infrared spectrometer	Vertical profile of water ice opacity	Objectives: I.A. - I.B. Essential for monitoring of atmospheric state and collection of long-term climatologies.	Per kilometer	10 ⁻⁴ km ⁻¹ to 10 ⁻² km ⁻¹	10 ⁻⁴ km ⁻¹ to 10 ⁻² km ⁻¹	0-40 km	PC	0-24 h	180°W - 180°E	85°S - 85°N	2°	1 sol	0-360°	5°	Radiance	TIR: mW m ⁻² sr ⁻¹ (cm ⁻¹) ⁻¹ ; NIR: W m ⁻² sr ⁻¹ (cm ⁻¹) ⁻¹	0-40 mW m ⁻² sr ⁻¹ (cm ⁻¹) ⁻¹	1%	NER < 0.1 mW m ⁻² sr ⁻¹ (cm ⁻¹) ⁻¹	10 s	270°	0.1°	12 microns, e.g. 40-400 cm ⁻¹ channels	~50 cm ⁻¹ channel	N/A
DIU-12	Thermal infrared spectrometer	Vertical profile of carbon dioxide opacity	Objectives: I.A. - I.B. Essential for monitoring of atmospheric state and collection of long-term climatologies.	Per kilometer	10 ⁻⁴ km ⁻¹ to 10 ⁻² km ⁻¹	10 ⁻⁴ km ⁻¹ to 10 ⁻² km ⁻¹	0-40 km	PC	0-24 h	180°W - 180°E	85°S - 85°N	2°	1 sol	0-360°	5°	Radiance	TIR: mW m ⁻² sr ⁻¹ (cm ⁻¹) ⁻¹ ; NIR: W m ⁻² sr ⁻¹ (cm ⁻¹) ⁻¹	0-40 mW m ⁻² sr ⁻¹ (cm ⁻¹) ⁻¹	1%	NER < 0.1 mW m ⁻² sr ⁻¹ (cm ⁻¹) ⁻¹	10 s	270°	0.1°	22 microns, e.g. 400-500 cm ⁻¹ centered at 22.2 microns	~100 cm ⁻¹ channels	N/A
DIU-13	Thermal infrared spectrometer	Vertical profile of water vapor opacity	Objectives: I.A. - I.B. Essential for monitoring of atmospheric state and collection of long-term climatologies.	Parts per million	0-2000 ppmv	0-2000 ppmv	0-40 km	PC	0-24 h	180°W - 180°E	85°S - 85°N	2°	1 sol	0-360°	5°	Radiance	mW m ⁻² sr ⁻¹ (cm ⁻¹) ⁻¹	0-40 mW m ⁻² sr ⁻¹ (cm ⁻¹) ⁻¹	1%	NER < 0.1 mW m ⁻² sr ⁻¹ (cm ⁻¹) ⁻¹	10 s	270°	0.1°	220-260 cm ⁻¹ channels	40 cm ⁻¹ and 12 cm ⁻¹ channels	N/A
DIU-14	Thermal infrared spectrometer	Surface temperature	Objectives: I.A. - I.B. Essential for monitoring of atmospheric state and collection of long-term climatologies.	Kelvin	130-320 K	130-320 K	N/A	PC	0-24 h	180°W - 180°E	85°S - 85°N	<0.02°	1 sol	0-360°	5°	Radiance	mW m ⁻² sr ⁻¹ (cm ⁻¹) ⁻¹	0-40 mW m ⁻² sr ⁻¹ (cm ⁻¹) ⁻¹	1%	NER < 0.17 mW m ⁻² sr ⁻¹ (cm ⁻¹) ⁻¹	4 s	270°	0.1°	290-340 cm ⁻¹ or beyond 50 microns really	50 cm ⁻¹ channel	N/A
DIU-15	Visible and/or UV imager	U.V. wind, dust storm and cloud structure and evolution	Objectives: I.A. - I.B. Essential for direct monitoring of dust storms/water ice clouds/CO ₂	Meters per second	0-200 m/s	0-200 m/s	depends on features, on up to 80 km (see km)	PC	Daylight hours	180°W - 180°E	80°S - 80°N	<0.1°	1 sol	0-360°	<<1°	Change in feature position	km	N/A	N/A	N/A	22°	0.01°	200-100 nm	100 nm	N/A	N/A

Figure 32.(Continued.)

ID	Instrument Type(s)	Physical Parameter (PP) Description	Link to Objectives	Units	PP Range		PP Resolution	PP Altitude Resolution	PP Coordinate System	PP Local Time (LT) Range	PP Longitude Resolution	PP Latitude Resolution	PP Seasonal Range	PP Seasonal Resolution	PP Description	Separate from physical parameter for remote data.				Angular Resolution (X) Polar (Y) Resolution	Polar (Y) Resolution	Energy/Wavelength/Frequency Range	Mass Range Resolution	Mass Resolution
					PP Range	PP Resolution	PP Altitude Resolution	PP Coordinate System	PP Local Time (LT) Range	PP Longitude Resolution	PP Latitude Resolution	PP Seasonal Range	PP Seasonal Resolution	PP Description	QO Units	QO Dynamic Range	QO Precision	QO SNR	QO Time Resolution	Angular Resolution (X) Polar (Y) Resolution	Polar (Y) Resolution	Energy/Wavelength/Frequency Range	Mass Range Resolution	Mass Resolution
HER-MUV/FUV 1	NIR spectrometer	Surface pressure	cloud evolution	Pascals	150-1500	5-10	N/A	N/A	PC	0-24 h	180°W-180°E	60°S-60°N	0-360°	1 sol	Radiance (I/F)	W m ⁻² sr ⁻¹ nm ⁻¹ dimensionless (C-L) (

Figure 32. (Continued.)

ID	Instrument Type(s)	Physical Parameter Description (pp)	Link to Objectives	Units	PP Range	PP Altitude Range	PP Altitude	PP Coord. System	PP Local Time Range	PP LT Range	PP Longitude	PP Latitude Range	PP Celestial Range	PP Seasonal Range	PP Seasonal Resolution	PP Description	QO Units	QO Dynamic Range	QO Precision	QO SNR	QO Time Resolution	Angular FOV (X)	Azimuth (Y) Range	Polar (Y) Range	Energy/ Wavelength/ Frequency Range	Resolution	Mass (where applicable)
1	LANGMUIR probe	Electron density	Obj 1 C, 2	Per cubic centimeter	200+ TE4	200-800 km	5 km	MSO	0-24 h	0-360°	15°	90°S to 90°N	20 vertical profiles per sol for 1 Mars year, widely dispersed in MSO	0-360°	Daily	N/A same as physical parameter	N/A same as physical parameter	N/A same as physical parameter	N/A	N/A	N/A	N/A	N/A	N/A	N/A	N/A	
2	SPACERATE	Electron density irregularities • Spectral density • Scatter electron occultation irregularities with length-scale > 10 km and magnitude > 1000 cm ⁻¹	Obj 1 C	Dimensionless	N/A	100-200 km	5 km	MSO	0-24 h	80-120° ± 300°	15°	90°S to 90°N	20 measurements per sol for 1 Mars year, widely dispersed in MSO	0-360°	Daily	Received radio power	Watts	Implementation dependent	Few %	1 second	N/A	N/A	N/A	Appropriate UHF (e.g., 100 MHz) needs to be selected	N/A	N/A	
3	IONOSPHERIC	Escape rate of ionospheric inventory of H ⁺	Obj 1 C	Measure loss rate of H ⁺ as a function of atmospheric density	10 ¹⁰ H ⁺ cm ⁻¹ s ⁻¹	100-1000 km	5 km	MSO	Global	~6 h	all	~45°	~daily	all	~daily	Lyman alpha brightness	Rayleighs	1% to 1-20	1%	100	~daily for one set of parameters	< 2°	> 10°	121-123 nm	1.5 nm	N/A	
4	IONOSPHERIC	Vector magnetic field	Obj 1 C Obj 1 D	nanotesla	~1 to 300 nT	0.3 nT or 200+ km	100 km	MSO	0-24 h	N/A	0-360°	90°S to 90°N	64 Hz	0-360°	N/A	N/A same as physical parameter	N/A same as physical parameter	N/A same as physical parameter	N/A	N/A	N/A	N/A	N/A	N/A	N/A	N/A	
5	IONOSPHERIC	Suprathermal electron flux	Obj 1 C Obj 1 D	eV per square centimeter per second	TE4 to 10 ⁵ eV	200+ km	N/A	MSO, MSE	0-24 h	N/A	0-360°	90°S to 90°N	16 sec	0-360°	N/A	N/A same as physical parameter	N/A same as physical parameter	N/A same as physical parameter	N/A	N/A	0-360°	30°	-80 to +90°	~1 eV to 10 keV	20% (DEE)	N/A	
6	IONOSPHERIC	Mass-separated ionospheric thermal ion flux	Obj 1 C Obj 1 D	eV per square centimeter per second	TE4 to 10 ⁵ eV	200+ km	N/A	MSO, MSE	0-24 h	N/A	0-360°	90°S to 90°N	16 sec	0-360°	N/A	N/A same as physical parameter	N/A same as physical parameter	N/A same as physical parameter	N/A	N/A	0-360°	30°	-80 to +90°	~1 eV to 20 keV	25% (DEE)	1 to 44 amu ± 2	
7	IONOSPHERIC	Vector electric field	Obj 1 C Obj 1 D	millivolts per meter	~300 to >300 mV/m	200+ km	N/A	MSO, MSE	0-24 h	N/A	0-360°	90°S to 90°N	2-16 samples/sec	0-360°	N/A	N/A same as physical parameter	N/A same as physical parameter	N/A same as physical parameter	N/A	N/A	N/A	N/A	N/A	N/A	N/A	N/A	
8	IONOSPHERIC	Electric field wave	Obj 1 C Obj 1 D	millivolts per meter	TE4 to 1E4 mV/m	200+ km	N/A	MSO, MSE	0-24 h	N/A	0-360°	90°S to 90°N	100 samples/sec w/ burst	0-360°	N/A	N/A same as physical parameter	N/A same as physical parameter	N/A same as physical parameter	N/A	N/A	N/A	N/A	N/A	DC to 8 Hz	N/A	N/A	
9	MAGNETIC	Magnetic field	Obj 1 C Obj 1 D	nT per root Hz	TE4 to 1E4 nT	200+ km	N/A	MSO, MSE	0-24 h	N/A	0-360°	90°S to 90°N	100 samples/sec w/ burst	0-360°	N/A	N/A same as physical parameter	N/A same as physical parameter	N/A same as physical parameter	N/A	N/A	N/A	N/A	N/A	1 Hz to 4 kHz	N/A	N/A	

Figure 32. (Continued.)

ID	Instrument	Physical Parameter (PP)	Link to Observables	Units	PP Res-olution	PP Altitude Range	PP Res-olution	PP Coord-inate System	PP Local Time	PP Long-itude Range	PP Long-itude Res-olution	PP Latitude Range	PP Latitude Res-olution	PP Cadence	PP Seasonal Range	PP Seasonal Res-olution	Observable Quantity (OQ)						Polar (Y) Res-olution	Energy/ Wavelength/ Frequency	Mass Range	Mass Res-olution
																	QO Description	QO Units	QO Dynamic Range	QO Precision	QO SNR	QO Time Resolution				
SPA-1	Solar EUV monitor	Solar EUV spectral irradiance	Obj 1.D8	Watts per meter per square nanometer	1E3 to 3E2	1E3 to 2000 km (upstream m solar wind)	> 2000 km (upstream m solar wind)	N/A	N/A	N/A	N/A	N/A	N/A	16 sec	0-360° Ls	N/A	N/A: same as physical parameter	N/A: same as physical parameter	N/A: same as physical parameter	N/A: same as physical parameter	N/A: same as physical parameter	N/A	10-22 nm, 12.16 nm	N/A	N/A	
SPA-2	Fluoride mag	Vector magnetic field	Obj 1.D8	nano Tesla	1 to 2000 nT	> 2000 km (upstream m solar wind)	N/A	MSC, MSE	N/A	N/A	N/A	N/A	N/A	64 Hz	0-360° Ls	N/A	N/A: same as physical parameter	N/A: same as physical parameter	N/A: same as physical parameter	N/A: same as physical parameter	N/A: same as physical parameter	N/A	N/A	N/A	N/A	
SPA-3	Ion energy/angle analyzer	Ion flux	Obj 1.D8	eV per square centimeter per second per steradian	1E7 to 1E10 eV/cm ² per second per eV	> 2000 km (upstream m solar wind)	N/A	MSC, MSE	N/A	N/A	N/A	N/A	N/A	16 sec	0-360° Ls	N/A	N/A: same as physical parameter	N/A: same as physical parameter	N/A: same as physical parameter	N/A: same as physical parameter	N/A: same as physical parameter	20 to 220° centered on Sun	-50 eV to 10 MeV	N/A	N/A	
SPA-4	Electron energy/angle analyzer	Suprathermal electron flux	Obj 1.D8	eV per square centimeter per second per steradian	1E4 to 1E10 eV/cm ² per second per eV	> 2000 km (upstream m solar wind)	N/A	MSC, MSE	0-24 h	0-360°	N/A	90° S to 90° N	N/A	16 sec	0-360° Ls	N/A	N/A: same as physical parameter	N/A: same as physical parameter	N/A: same as physical parameter	N/A: same as physical parameter	N/A: same as physical parameter	0-360°	1 eV to 10 MeV	N/A	N/A	
SPA-5	Energetic ion detector	Ion/electron flux	Obj 1.D8	eV per square centimeter per second per steradian	1E1 to 1E6 eV/cm ² per second per eV	> 2000 km (upstream m solar wind)	N/A	MSC, MSE	0-24 h	0-360°	N/A	90° S to 90° N	N/A	20 min	0-360° Ls	N/A	N/A: same as physical parameter	N/A: same as physical parameter	N/A: same as physical parameter	N/A: same as physical parameter	N/A: same as physical parameter	40 x 40° centered on +ve Parker spiral dir	50 keV to 5 MeV	N/A	N/A	

Figure 32. (Continued.)

A.9. Instrument Requirements

Figure 33 provides detailed requirements for all of the scientific instruments necessary to make MOSAIC's required measurements.

Investigation	Description	Name	Platform	Measurements (Up to 4; please link to physical parameters)			Supplier	TRL	Time to TRL5	\$ to TRL5	Time to TRL 5 to 6	\$ TRL 5 to 6	FOV	Mass	Power	Volume	Accommodation/ Operational Requirement	Wavelength/ Frequency/ Field Range	Resolution/ Number of channels	Bits Per Sample	Sample Rate	Threshold Data Rate (bps)	Baseline Data Rate (orbit-average bps)	Phase A-D Cost (\$FY20)	Contributable?	Notes	
ICE	Radar (P-band SAR)	POPSAR (polarimetric orbital p-band SAR)	Mothership	Surface backscatter	Polarimetric backscatter	dielectric permittivity	N/A	JPL	8	N/A	N/A	N/A	35-39° (based on Eagle)	125 kg (based on ESA Biomass)	200 W operational; 500 W peak	1.94 m³ (Eagle)		400 MHz	30 m (HDR)/100 m (LDR)			800,000	1.50E+06	\$170M (estimate based on ESA Biomass)	Yes - Canada (already offered as part of COMPASS)		
ICE	UV-VIS-NIR Imager	Mars Atmosphere, Volatile, and Resource Investigation Camera (MAVRIC)	Mothership	Duration of (dust/water ice) aerosol clouds	Water ice column opacity	Carbon dioxide ice column opacity		JHU APL	7 except for detector array (TRL 5)	N/A	N/A	For detector array	For detector array	150°	0.97+2.42 kg electronics	2.1 W cameras, 8.2W electronics	10 cm x 7.5 x 14, 12 x 10 x 3.5 interface adapter	0.34-0.75 um, 1.1-1.6 um	6 channels between 0.34-0.75 um, 6 channels between 1.1-1.6 um			8.8 Gb/sol downlinked ~102 Kb/s collected orbit average	11 Gb/sol downlinked ~127 Kb/s collected orbit average	\$13M (without reserves)	Yes		
ATM	Lidar	MARLI	Mothership	Vertical profile of horizontal wind in its zonal and meridional components (U, V)	Vertical profile of dust opacity	Vertical profile of water ice opacity		GSFC	6 by 6/2020					38 kg	81 W	760 x 760 x 640 mm		1064 nm		50 kbits/s data rate threshold, 50 kbps baseline	25 kbps threshold, 50 kbps baseline	50000	~\$40M	No			
ATM	Lidar	OPAL	Mothership	0-50 km or greater temperature	Pressure, density (down to surface possible)	Aerosol Opacity	Wind velocity (u,v,w)	NASA Langley	3 (Developed under the IRAD program)	3 years	\$3M	2 years	\$5M	~0.1 mrad	40 kg	45-55 W	0.15 m² (MOLA)	N/A	25 MHz over 1 GHz wide spectral interval	5188-15564	3 s	5000	1730-5190; raw data of 1 sample per orbit would require: 139000	~\$70M	No		
ATM	Sub-mm sounder	Sub-mm sounder	Mothership	0-100 km temperature (incl. surface)	Horizontal wind velocity	Water vapor concentration		JPL	5 (Developed under the IRAD program); There is only one item needing testing; could be done with \$50K	N/A	N/A	3-6 months	\$50K	2-antenna: 35 kg; 1-fixed-antenna: 11.5 kg	2-antenna: 50 W (+20 for USO, if needed); 1-fixed-antenna: 15.6 W	2-antenna: 20x20x10 cm 2, 30 cm diam antennas; 1-fixed-antenna: 20x10x10 cm, 1 30 cm diam antenna		~450 GHz	3 GHz spectrometers; zoom to 300 MHz channels; tunable	10 kbps compressed (40 kbps raw)	Variable		2-antenna: ~\$35M (Discovery mission proposal); 1-antenna: ~\$25M (Delta from Discovery mission proposal)	No			
ATM	Thermal IR radiometer	Limb-nadir radiometer	Mothership	Vertical profile of temperature	Vertical profile of dust opacity	Vertical profile of water ice opacity		JPL	9 (Equivalent to MRO/MCS)	N/A	N/A	N/A	N/A	FOV 70 mrad, IFOV 1.8 mrad	9 kg	18 W	Swept volume: 420 mm (cylindrical diameter) x 400 mm (height)	12-42 micron 0.3-3 microns	9 channels	8 kbits/sample	2 s	4000	~\$25M				
ATM/DIU	Thermal IR radiometer	Mini-MCS (limb-nadir)	SmallSats	Vertical profile of temperature	Vertical profile of dust opacity	Vertical profile of water ice opacity		JPL	6 (Heritage from MCS subsystems, PREFIRE)	N/A	N/A	N/A	N/A	FOV 70 mrad, IFOV 1.8 mrad	3.5 kg	8 W	2U	12-42 micron, 0.3-3 micron	9 channels	8 kbits/sample	2 s	4000	~\$10M for first unit, ~\$5M for follow-on units				

Figure 33. Details of Measurement, Accommodation, and Development Requirements for the MOSAIC Instruments. Each row corresponds to a single instrument

[illegible]

Figure 33. (Continued.)

Investigation	Description (VIS-NIR)	Name	Platform	Measurements (Up to 4; please link to physical parameters)	Supplier	TRL	Time to TRL5	\$ to TRL5	Time TRL5 to 6	\$ TRL5 to 6	FOV	Mass	Power	Volume	Accommodation/Operational Requirement	Wavelength/Frequency/Field Range	Resolution/Number of channels	Bits Per Sample	Sample Rate	Threshold Data Rate (bps)	Baseline Data Rate (average bps)	Phase A-D Cost (\$FY20)	Contributable?	Notes
DIU	RGB or multispectral imager	Gecko Imager	SmallSats	Weather context (PAN+MS)	SCS & Space Advisory Earth Satellite	9 (Flew on Earth satellite)	N/A	N/A	N/A	N/A	9.2° FOV; IFOV=0.08 mrad	500 g	<3.5 W	58 mm x 97 mm x 96 mm (1U)	If at geostationary, it requires some scanning to cover full Martian disk	Visible		450 kb-3 MB	5 frames/s (5x450 kb images) (frames/1 per hour)	5000	30 kbps	\$100K		
	Radio occultation with directional antenna	TX/RX radio	Mothership and SmallSats	Vertical profile of temperature pressure (geostrophic winds)	JPL	> 6 (based on the IRIS radio with modification for SmallSats and UST for large orbiter)	N/A	N/A	N/A	N/A	Antenna bore sight in velocity and anti-velocity direction: $\pm 4-60^\circ$ in azimuth, $\pm 4-10^\circ$ in elevation	1.45 kg (IRIS)	<33 W (IRIS)	10 cm x 10 cm x 5 cm (IRIS)	Objective: SIX dual-bands; Preset: X-band			16 (I and Q, 8 bits each)	1 kHz					
DIU	UV-Vis-NIR imager	Mars Atmosphere and Resource Investigation Camera (MAVRIC)	Mothership, SmallSats	Duration of dust/water column aerosol opacity clouds	JHU APL	7 except for detector array (TRL 5)	N/A	N/A	TBD	TBD	150°	0.97x2.42x2.1 W kg electronics	2.1 W electronics	10 cm x 7.5 x 14, 1.2 x 10 x 3.5 interface adapter	0.34-0.75 μ m, 1.1-1.6 μ m	6 channels between 0.34-0.75 μ m, 6 channels between 1.1-1.6 μ m				8.8 Gb/sol downlink collected orbit average	11 Gb/sol (without reserves)	\$13M		
	FUV/MUV spectrograph	UVS	Mothership	Altitude profiles of O ₂ thermospheric density	LASP/SWRI	9	N/A	N/A	N/A	N/A	Limb (needs accurate limb tracking)	27 kg	28 W	Limb viewing 250 km tangent altitude	FUV: 15-134 nm, MUV: 190-300 nm		FUV: 1.5 nm, MUV: 2 nm	FUV: 10 Kb, MUV: 20 Kb	40 integrations for MUV, 3 minutes	5 kbps	8 kbps	\$30M ROM		
Ther	EUV/FUV spectrograph	EMM EMUS	Mothership or Atmosphere	Altitude profiles of O ₂ thermospheric density	LASP/SWRI	9	N/A	N/A	N/A	N/A	Limb (needs accurate tracking)	15 kg	15 W											
Ther	Interferometer	ICON MIGHT	Mothership	Horizontal Wind	NRL	9	N/A	N/A	9 months	\$3M	Limb (needs accurate limb tracking)	40 kg	13 W	Limb view 135° to ram, baffle to exclude planet, pointing and 50° FOV away from lower atmosphere, sun etc.	2 channels, 57.7 nm and 1.27 μ m each with 2 wave lengths and 50 elements		\$1.26M	2 exposures per channel, 3 minutes	10 kbps	14 kbps orbit av	\$40M (without reserves)			

Figure 33. (Continued.)

Investigation	Description	Name	Platform	Measurements (Up to 4; please link to physical parameters)	Supplier	TRL	Time to TRLs	\$ to TRLs	Time to TRL 5 to 6	\$ TRL 5 to 6	FOV	Mass (IRIS)	Power (IRIS)	Volume (cm x cm x cm) (IRIS)	Accommodation/Operational Requirement	Wavelength/Frequency/Field Range	Resolution/Number of channels	Bits Per Sample	Sample Rate (plus on data at 1 Hz)	Threshold Data Rate (bps)	Baseline Data Rate (orbital-average bps)	Phase A-D Cost (\$FY20)	Contributable?	Notes
IONO	Spacecraft radio occultation	Spacecraft radio occultation	All	Electron density	JPL	5	N/A	N/A	3 years	\$3M	Antenna in bore sight	1.45 kg	<33 W (IRIS)	10 cm x 10 cm x 3 cm (IRIS)	TBD	UHF/L-S band (dual-frequency desirable)	N/A	16 (I and Q, 8 bits each)	1 kHz (plus on data at 1 Hz)	11000	\$2M	No	16 bits per sample, 1 kHz rate, 10 min duration = 167 bits of observation, 100 observations per sol = 16700 bits per sol = 11000 bits per second. Some kind of onboard data processing and compression would reduce this greatly, if feasible	
		Multi-Needle Langmuir probe (only one of this or Planar ion probe is required)	Langmuir probe	Elliptical	Electron density	Embry-Riddle	6	N/A	N/A	N/A	N/A	N/A	0.25 kg	<1 W	Needles are tiny, electronic is a single small board	Must be on a boom more than 20 cm from spacecraft body.	N/A	N/A	112, uncompressed	1 sample per second	10	\$0.5M	No	Assume data collected for 20 minutes in every 4 hour orbit
IONO	Planar ion probe which measures N-total, N-parallel, N-perpendicular to equal Ne (only one of this or multi-Needle Langmuir probe is required)	Pseudo-Langmuir probe	Elliptical	Electron density	Embry-Riddle	6	N/A	N/A	N/A	N/A	N/A	0.20 kg	<0.5 W	PIP is a flat gold panel on the side of the spacecraft. Electronic is a single small board	Needs 20 cm x 20 cm surface area to put as patch the side of sensor	N/A	N/A	32, uncompressed	1 sample per second	10	\$0.5M	No	Assume data collected for 20 minutes in every 4 hour orbit	
EXO	EUUV/FUV spectrograph	Mothership		Coronal brightness profiles of O profiles of H	LASPS/SLSWRI	9	N/A	N/A	N/A	N/A	Along Mars-Sun line up to 5 Mars radii	20 kg	20 W	60 x 25 x 15 cm		100-140 nm	~1 nm	Depends, highly instrument dependent. Is highly instrument configurable	Highly instrument dependent estimate of total data rate based on EMME MUS	~4kpbs	\$20M	No	Assume data collected for 20 minutes in every 4 hour orbit	
MAGN	Small fluxgate mag	Fluxgate mag	Elliptical, L1 High elliptical	Magnetic field vectors	GSFC, UCLA	9	N/A	N/A	N/A	N/A	N/A	<1 kg	<1 W	Sensor: ~1 cm x 1 cm x 1 cm Electronic: ~8 cm x 8 cm x 1 cm	Mag cleanliness	N/A	N/A	48	~6 kbps, 200 samples/sec	800	~\$4M	Japan, Germany		
MAGN	Ion electrostatic analyzer with mass discrimination	Ion ESA-TOF	Elliptical	Ion moments (density, temperature, velocity), separated by mass	SSL	9	N/A	N/A	N/A	N/A	360 x 90° (3-axis but could be adapted to spinner)	2.8 kg	3.7 W	26 x 14 x 14 cm	Electrostatic cleanliness, clear FOV	N/A	N/A	2 kb	16 seconds	2000	~\$4M	Sweden, France		
MAGN	Electron electrostatic analyzer	Electron ESA	Elliptical	Electron moments (density, temperature, velocity), separated by mass	SSL, SwRI	9	N/A	N/A	N/A	N/A	360 x 120° (3-axis but could be adapted to spinner)	1.6 kg	1 W	20 x 16 x 16 cm	Electrostatic cleanliness, onboard pitch angle sorting, clear FOV	N/A	N/A	160	1 sample per 4 seconds	1000	~\$3M	France		

Figure 33. (Continued.)

Investigation	Description	Name	Platform	Measurements (Up to 4; please link to physical parameters)			Supplier	TRL	Time to TRL5	\$ to TRL5	Time to TRL 5 to 6	\$ TRL 5 to 6	FOV	Mass	Power	Volume	Accommodation/Operational Requirement	Wavelength/Frequency/Field Range	Resolution/Number of channels	Bits Per Sample	Sample Rate	Threshold Data Rate (bps)	Baseline Data Rate (orbit-average bps)	Phase A-D Cost (\$FY20)	Contributable?	Notes
MAGN	Electric field and waves	Electric field antennas	Elliptical	Vector electric field	Electric field wave power		SSL	9	N/A	N/A	N/A	N/A	N/A (must be booms spinner)	12 kg (6 booms)	0.24 W	8-cm-diameter spheres	Spinning, electrostatically clean spacecraft	DC to 300 kHz	up to 8192	16	4 samples per second	500	1000	~\$2M		Reflight of THEMIS EFI
MAGN	Magnetic waves	Search coil magnetometer	Elliptical	Magnetic field wave power			CETP, France Univ. Iowa	9	N/A	N/A	N/A	N/A	omnidirectional	1.8 kg (1 boom)	0.08 W	3 orthogonal 18-cm-long rods on a 1-m boom	Magnetic cleanliness (dynamic)	0.1 Hz to 4 kHz	up to 8192	16	4 samples per second	200	800	~\$3M (incl. boom)		Reflight of THEMIS SCM
SPA	Extreme ultraviolet monitor	EUVM	Long	Solar EUV flux in three band passes			LASP	9	N/A	N/A	N/A	N/A	Sun pointed to within 3°	1.4 kg	0.09 W (operational) 2.3 W (including heater).	16 x 13 x 9 cm	Sun pointing	10-20 nm, 17-22 nm, 121.6 nm	3 bands	48	1 sample per second	20	200	\$1.39M		Reflight of MAVEN EUVM requires external A/D signal processing electronics.
SPA	Extreme ultraviolet monitor	EUVM v2	Long	Solar EUV flux in three band passes			LASP	4	1 month	\$10K	3 months	\$40K	Sun pointed to within 3°	0.75 kg	0.73 W (operational) 2.6 W (including heater).	10 x 10 x 7 cm	Sun pointing	10-20 nm, 17-22 nm, 121.6 nm	3 bands	48	1 sample per second	20	200	\$1.66M		Updated MAVEN EUVM design with internal A/D signal processing electronics.
SPA	Extreme ultraviolet monitor	EUVM v3	Long	Solar EUV flux in three band passes			LASP	4	3 months	\$60K	3 months	\$40K	Sun pointed to within 3°	1.1 kg	0.73 W (operational) 2.6 W (including heater).	15 x 10 x 7 cm	Sun pointing	10-20 nm, 17-22 nm, 121.6 nm	3 bands	48	1 sample per second	20	200	\$1.85M		Updated MAVEN EUVM design that mitigates soft x-ray contamination to signal resulting in a factor of two improvement in accuracy.
SPA	Ion electrostatic analyzer	Solar Wind Ion Analyzer	L1, high elliptical	Ion moments (density, temperature, velocity) of solar wind and magnetosheath H ₊ , with some discrimination of He using energy	Ion velocity distribution functions		SSL, SwRI	9	N/A	N/A	N/A	N/A	360 x 90° (3-axis stabilized)	1.8 kg	1 W	20 x 16 x 16 cm		N/A				500	1000	~\$3M		
SPA	Solid state telescope	Solid state telescope	L1, high elliptical	Energetic ion flux in 4 directions	Energetic electron flux in 4 directions		SSL	9	N/A	N/A	N/A	N/A		1.1 kg	3.2 W							20	100	~\$0.8M		

Figure 33. (Continued.)

A.10. MOSAIC Concept Study Report Cover Art

Figure 34 shows the original cover and cover art from the MOSAIC Final Report submitted to NASA and the National Academies of Science, Engineering, and Medicine in 2020 August.

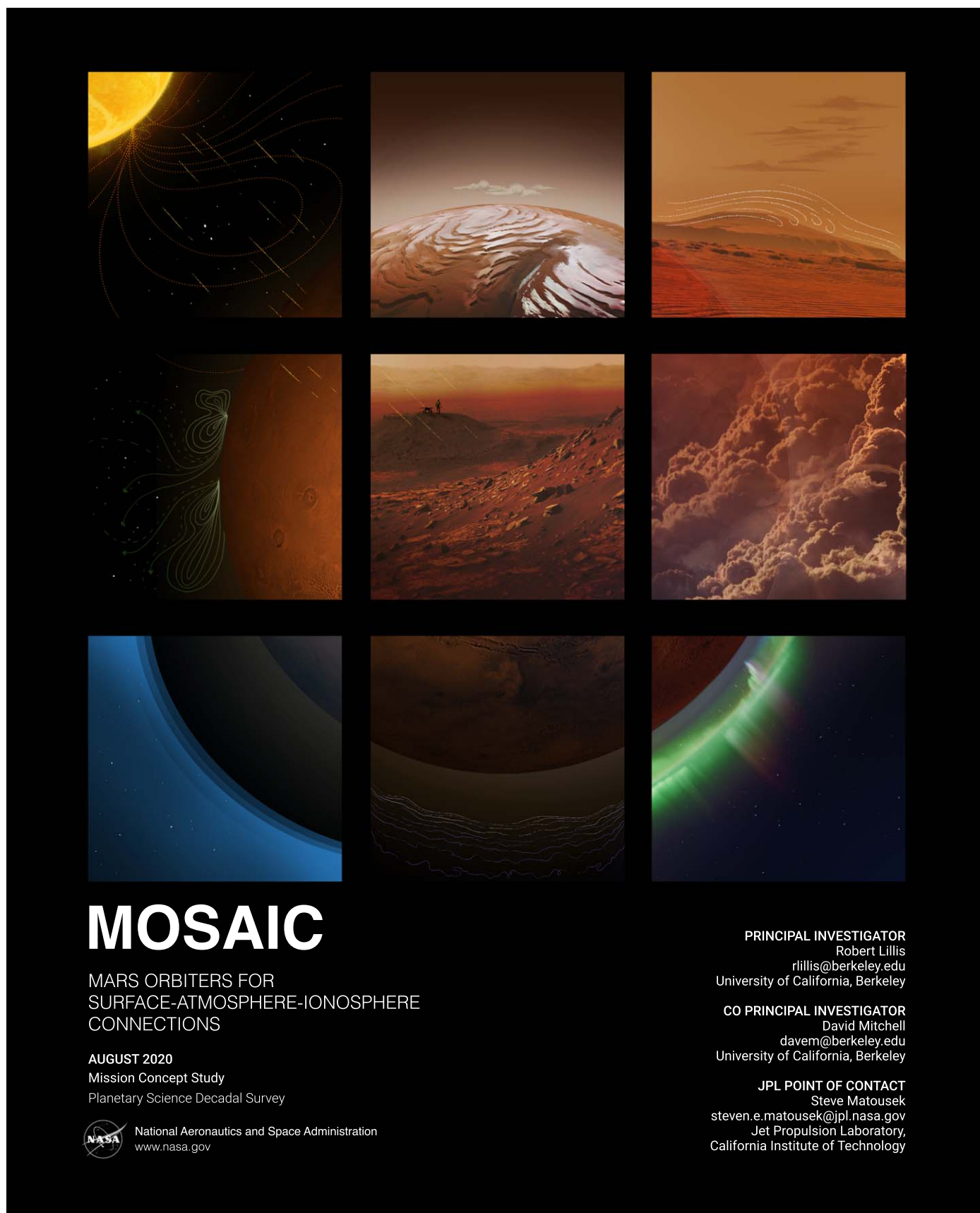


Figure 34. Cover page from the MOSAIC Planetary Mission Concept Study Report (437 pages) submitted to NASA and the National Academy of Sciences, Engineering, and Medicine on 2020 August 7.

ORCID iDs

Robert J. Lillis  <https://orcid.org/0000-0003-0578-517X>
 David Mitchell  <https://orcid.org/0000-0001-9154-7236>
 Luca Montabone  <https://orcid.org/0000-0003-4998-914X>
 Nicholas Heavens  <https://orcid.org/0000-0001-7654-503X>
 Scott Guzewish  <https://orcid.org/0000-0003-1149-7385>
 Scott England  <https://orcid.org/0000-0001-5336-0040>
 Paul Withers  <https://orcid.org/0000-0003-3084-4581>
 Mike Chaffin  <https://orcid.org/0000-0002-1939-4797>
 Shannon Curry  <https://orcid.org/0000-0002-7463-9419>
 Chi Ao  <https://orcid.org/0000-0001-6171-0872>
 Steven Matousek  <https://orcid.org/0000-0001-9712-0380>
 Ryan Woolley  <https://orcid.org/0000-0002-5179-5953>
 Isaac Smith  <https://orcid.org/0000-0002-4331-913X>
 Gordon R. Osinski  <https://orcid.org/0000-0002-1832-5925>
 Leslie Tamppari  <https://orcid.org/0000-0001-5124-6375>
 Michael Mischna  <https://orcid.org/0000-0002-8022-5319>
 David Kass  <https://orcid.org/0000-0002-7154-2566>
 Michael Wolff  <https://orcid.org/0000-0002-1127-8329>
 Aymeric Spiga  <https://orcid.org/0000-0002-6776-6268>
 François Forget  <https://orcid.org/0000-0002-3262-4366>
 Justin Deighan  <https://orcid.org/0000-0003-3667-902X>
 Amanda Brecht  <https://orcid.org/0000-0002-9018-6528>
 Stephen Bougher  <https://orcid.org/0000-0002-4178-2729>
 Christopher M. Fowler  <https://orcid.org/0000-0003-3431-0739>
 David Andrews  <https://orcid.org/0000-0002-7933-0322>
 Kerstin Peter  <https://orcid.org/0000-0002-1353-0110>
 Mark Lester  <https://orcid.org/0000-0001-7353-559>
 Beatriz Sánchez-Cano  <https://orcid.org/0000-0003-0277-3253>
 Janet Luhmann  <https://orcid.org/0000-0003-0626-9353>
 François Leblanc  <https://orcid.org/0000-0002-5548-3519>
 Jasper Halekas  <https://orcid.org/0000-0001-5258-6128>
 David Brain  <https://orcid.org/0000-0001-8932-368X>
 Xiaohua Fang  <https://orcid.org/0000-0002-6584-2837>
 Jared Espley  <https://orcid.org/0000-0002-6371-9683>
 Hermann Opgenoorth  <https://orcid.org/0000-0001-7573-5165>
 Oleg Vaisberg  <https://orcid.org/0000-0002-6590-644X>
 David Hinson  <https://orcid.org/0000-0002-1620-4011>
 Sami Asmar  <https://orcid.org/0000-0002-9912-645X>
 Joshua Vander Hook  <https://orcid.org/0000-0002-0493-237X>
 Ozgur Karatekin  <https://orcid.org/0000-0003-0153-7291>
 Aroh Barjatya  <https://orcid.org/0000-0002-1939-6143>

References

- Acuña, M. H., Connerney, J. E. P., Wasilewski, P., et al. 1992, *JGRA*, **97**, 7799
 Acuña, M. H., Connerney, J. E. P., Wasilewski, P., et al. 2001, *JGR*, **106**, 23403
 Adams, D., Xu, S., Mitchell, D. L., et al. 2018, *GeoRL*, **45**, 12190
 Akbari, H., Andersson, L., Peterson, W. K., et al. 2019, *JGRA*, **124**, 4518
 Amiri, S., Brain, D., Sharaf, O., et al. 2021, *SSRv*
 Anderson, D. E., & Hord, C. W. 1971, *JGR*, **76**, 6666
 Andrews, D. J., Andersson, L., Delory, G. T., et al. 2015, *GeoRL*, **42**, 8862
 Angelopoulos, V., Sibeck, D., Carlson, C. W., et al. 2008, *SSRv*, **141**, 453
 Ao, C. O., Edwards, C. D., Kahan, D. S., et al. 2015, *RaSc*, **50**, 997
 Barabash, S., Fedorov, A., Sauvaud, J. J., et al. 2007, *Natur*, **450**, 650
 Barjatya, A., & Merritt, W. 2018, *RSci*, **89**, 043507
 Bass, D. S., Herkenhoff, K. E., & Paige, D. A. 2000, *Icar*, **144**, 382
 Battalio, M., & Wang, H. 2021, *Icar*, **354**, 114059
 Beatty, D., Carr, M. H., Abell, P., et al. 2012, Analysis of Strategic Knowledge Gaps Associated with Potential Human Missions to the Martian System: Final Report of the Precursor Strategy Analysis Group (P-SAG), https://www.lpi.usra.edu/sbag/meetings/jul2012/presentations/TUES_1030_Abell_PSAG.pdf
 Bell, J. F., Wolff, M. J., Malin, M. C., et al. 2009, *JGRE*, **114**, E08S92
 Benna, M., Bougher, S. W., Lee, Y., et al. 2019, *Sci*, **366**, 1363
 Benna, M., Mahaffy, P. R., Grebowsky, J. M., et al. 2015, *GeoRL*, **42**, 8958
 Benson, J. L., & James, P. B. 2005, *Icar*, **174**, 513
 Bertaux, J.-L., Leblanc, F., Perrier, S., et al. 2005, *Sci*, **307**, 566
 Bertrand, T., Wilson, R. J., Kahre, M. A., Urata, R., & Kling, A. 2020, *JGRE*, **125**, e2019J006122
 Bhattacharyya, D., Clarke, J. T., Bertaux, J. L., Chaufray, J. Y., & Mayyasi, M. 2015, *GeoRL*, **42**, 8678
 Bhattacharyya, D., Chaufray, J. Y., Mayyasi, M., et al. 2020, *Icar*, **339**, 113573
 Birkenheuer, D. L. 1987, *AdSpR*, **7**, 363
 Bonnell, J. W., Mozer, F. S., Delory, G. T., et al. 2008, *SSRv*, **141**, 303
 Bougher, S. W., Brain, D. A., Fox, J. L., et al. 2014, in *The Atmosphere and Climate of Mars*, ed. R. M. Haberle et al. (Cambridge: Cambridge Univ. Press), 405
 Bougher, S. W., Pawlowski, D., Bell, J. M., et al. 2015, *JGRE*, **120**, 311
 Bougher, S. W., Roeten, K. J., Olsen, K., et al. 2017, *JGRA*, **122**, 1296
 Boynton, W. V., Feldman, W. C., Squyres, S. W., et al. 2002, *Sci*, **297**, 81
 Bramson, A. M., Byrne, S., & Bapst, J. 2017, *JGRE*, **122**, 2250
 Bramson, A. M., Byrne, S., Putzig, N. E., et al. 2015, *GeoRL*, **42**, 6566
 Brothers, T. C., Holt, J. W., & Spiga, A. 2015, *JGRE*, **120**, 1357
 Byrne, S., Hayne, P. O., Calvin, W. M., et al. 2020, *LPICo*, **2099**, 6013
 Byrne, S., Dundas, C. M., Kennedy, M. R., et al. 2009, *Sci*, **325**, 1674
 Calvin, W. M., James, P. B., Cantor, B. A., & Dixon, E. M. 2015, *Icar*, **251**, 181
 Cantor, B. A. 2007, *Icar*, **186**, 60
 Cantor, B. A., James, P. B., Caplinger, M., & Wolff, M. J. 2001, *JGR*, **106**, 23653
 Carter, L. M., Campbell, B. A., Watters, T. R., et al. 2009, *Icar*, **199**, 295
 Chaffin, M. S., Chaufray, J.-Y., Stewart, I., et al. 2014, *GeoRL*, **41**, 314
 Chaffin, M. S., Deighan, J., Schneider, N. M., & Stewart, A. I. F. 2017, *NatGe*, **10**, 174
 Chaffin, M. S., Chaufray, J.-Y., Deighan, J., et al. 2015, *GeoRL*, **42**, 9001
 Chaffin, M. S., Chaufray, J.-Y., Deighan, J., et al. 2018, *JGRE*, **123**, 2192
 Chaffin, M. S., Kass, D. M., Aoki, S., et al. 2019, *LPICo*, **2089**, 6312
 Chaufray, J. Y., Gonzalez-Galindo, F., Forget, F., et al. 2015, *Icar*, **245**, 282
 CIRA 2011, Cooperative Institute for Research in the Atmosphere Annual Report FY 2010/2011, https://www.cira.colostate.edu/wp-content/uploads/sites/4/2019/05/cira_annual_report_fy10-11.pdf
 Clancy, R. T., Montmessin, F., Benson, J., et al. 2017, in *The Atmosphere and Climate of Mars*, ed. R. M. Haberle (Cambridge: Cambridge Univ. Press), 76, doi:10.1017/9781139060172.005
 Clancy, R. T., Wolff, M. J., Whitney, B. A., et al. 2010, *Icar*, **207**, 98
 Clarke, J. T., Bertaux, J. L., Chaufray, J. Y., et al. 2014, *GeoRL*, **41**, 8013
 Clifford, S. M. 1993, *JGR*, **98**, 10973
 Colaprete, A., Haberle, R. M., & Toon, O. B. 2003, *JGRE*, **108**, 5081
 Colaprete, A., & Toon, O. B. 2002, *JGRE*, **107**, 5051
 Collinson, G., Wilson, L. B., Omid, N., et al. 2018, *JGRA*, **123**, 7241
 Connerney, J. E. P., Espley, J., Lawton, P., et al. 2015, *SSRv*, **195**, 257
 Conrath, B. J., Pearl, J. C., Smith, M. D., et al. 2000, *JGR*, **105**, 9509
 Cravens, T., Rahmati, A., Lillis, R. J., et al. 2016, *AGUFM*, P12A-07
 Cremons, D. R., Abshire, J. B., Sun, X., et al. 2020, *CEAS*, **12**, 149
 Curry, S., Luhmann, J., Jakosky, B. M., et al. 2016, *AAS Meeting*, **228**, 213.01
 Deighan, J., Chaffin, M. S., Chaufray, J.-Y., et al. 2015, *GeoRL*, **42**, 9009
 Deighan, J., Jain, S. K., Chaffin, M. S., et al. 2018, *NatAs*, **2**, 802
 Dong, Y., Fang, X., Brain, D. A., et al. 2015, *GeoRL*, **42**, 8942
 Dreier, C. 2019, The Cost of the MAVEN Mission to Mars (Pasadena, CA: The Planetary Society), <https://www.planetary.org/space-policy/maven-cost>
 Drouin, B., & L'Ecuyer, T. S. 2018, in 73rd International Symp. on Molecular Spectroscopy (Urbana-Champaign, IL: Univ. Illinois Urbana-Champaign), **R101**
 Dubinin, E., Fraenz, M., Pätzold, M., et al. 2017, *JGRA*, **122**, 11285
 Dubinin, E., Fraenz, M., Pätzold, M., et al. 2018, *P&SS*, **160**, 56
 Dundas, C. M., & Byrne, S. 2010, *Icar*, **206**, 716
 Edberg, N. J. T., Nilsson, H., Williams, A. O., et al. 2010, *GeoRL*, **37**, L03107
 Elrod, M. K., Bougher, S., Roeten, K., & Murphy, J. 2020, *GeoRL*, **47**, e84378
 England, S. L., Liu, G., Withers, P., et al. 2016, *JGRE*, **121**, 594
 Englert, C. R., Harlander, J. M., Brown, C. M., et al. 2017, *SSRv*, **212**, 553
 Eparvier, F., Chamberlin, P. C., & Woods, T. N. 2015, *SSRv*, **195**, 293
 Evans, J. S., Stevens, M. H., Lumpe, J. D., et al. 2015, *GeoRL*, **42**, 9040
 Fabry, F., Turner, B. J., & Cohn, S. A. 1995, *BAMS*, **76**, 1806
 Fang, X., Liemohn, M. W., Nagy, A. F., et al. 2008, *JGRA*, **113**, A02210
 Fedorova, A., Bertaux, J. L., Betsis, D., et al. 2018, *Icar*, **300**, 440

- Feldman, W. C., Mellon, M. T., Gasnault, O., et al. 2007, *GeoRL*, **34**, L05201
- Fischer, E., Martínez, G. M., Rennó, N. O., Tamppari, L. K., & Zent, A. P. 2019, *JGRE*, **124**, 2780
- Flynn, C. L., Vogt, M. F., Withers, P., et al. 2017, *GeoRL*, **44**, 10812
- Forget, F., Hourdin, F., Fournier, R., et al. 1999, *JGR*, **104**, 24155
- Fowler, C. M., Andersson, L., Ergun, R. E., et al. 2018a, *JGRA*, **123**, 4129
- Fowler, C. M., Andersson, L., Halekas, J., et al. 2017, *JGRA*, **122**, 8536
- Fowler, C. M., Andersson, L., Peterson, W. K., et al. 2018b, *GeoRL*, **45**, 493
- Fuselier, S. A., Lewis, W. S., Schiff, C., et al. 2016, *SSRv*, **199**, 77
- Girazian, Z., Mahaffy, P., Lillis, R. J., et al. 2017a, *GeoRL*, **44**, 11248
- Girazian, Z., Mahaffy, P. R., Lillis, R. J., et al. 2017b, *JGRA*, **122**, 4712
- Gonzalez-Galindo, F., Chaufray, J.-Y., López-Valverde, M. A., et al. 2013, *JGRE*, **118**, 2105
- Gustafsson, G., André, M., Carozzi, T., et al. 2001, *AnGeo*, **19**, 1219
- Guzewich, S. D., Toigo, A. D., & Waugh, D. W. 2016, *Icar*, **278**, 100
- Guzewich, S. D., Wilson, R. J., McConnochie, T. H., et al. 2014, *JGRE*, **119**, 506
- Haberle, R. M., Pollack, J. B., Barnes, J. R., et al. 1993, *JGR*, **98**, 3093
- Halekas, J. S. 2017, *JGRE*, **122**, 901
- Halekas, J. S., Taylor, E. R., Dalton, G., et al. 2015, *SSRv*, **195**, 125
- Harlander, J. M., Englert, C. R., Brown, C. M., et al. 2017, *SSRv*, **212**, 601
- Harvey, P., Taylor, E., Sterling, R., & Cully, M. 2008, *SSRv*, **141**, 117
- Hayne, P. O., Paige, D. A., Heavens, N. G., & Team, M. C. S. S. 2014, *Icar*, **231**, 122
- Hayne, P. O., Paige, D. A., Schofield, J. T., et al. 2012, *JGRE*, **117**, E08014
- Heavens, N. G. 2017, *JATIS*, **74**, 1011
- Heavens, N. G., Kass, D. M., Kleinböhl, A., & Schofield, J. T. 2020, *Icar*, **341**, 113630
- Heavens, N. G., Kass, D. M., & Shirley, J. H. 2019, *JGRE*, **124**, 2863
- Heavens, N. G., Cantor, B. A., Hayne, P. O., et al. 2015, *GeoRL*, **42**, 3730
- Heavens, N. G., Kleinböhl, A., Chaffin, M. S., et al. 2018, *NatAs*, **2**, 126
- Hinson, D. P., Simpson, R. A., Twicken, J. D., Tyler, G. L., & Flasar, F. M. 1999, *JGR*, **104**, 26997
- Ho, S.-p., Anthes, R. A., Ao, C. O., et al. 2020, *BAMS*, **101**, E1107
- Hollingsworth, J. L., & Kahre, M. A. 2010, *GeoRL*, **37**, L22202
- Hughes, A., Chaffin, M., Mierkiewicz, E., et al. 2019, *JGRA*, **124**, 10533
- Immel, T. J., England, S. L., Mende, S. B., et al. 2017, *SSRv*, **214**, 13
- Jain, S. K., Stewart, A. I. F., Schneider, N. M., et al. 2015, *GeoRL*, **42**, 9023
- Jakosky, B. M., Brain, D., Chaffin, M., et al. 2018, *Icar*, **315**, 146
- Jakosky, B. M., & Haberle, R. M. 1990, *JGR*, **95**, 1359
- James, P. B., & Cantor, B. A. 2001, *Icar*, **154**, 131
- Holsclaw, G., Deighan, J., Al Matroushi, H. R., et al. 2021, *AdSpR*, in press
- Kahn, R. 1984, *JGR*, **89**, 6671
- Kahre, M. A., Hollingsworth, J. L., Haberle, R. M., & Wilson, R. J. 2015, *Icar*, **260**, 477
- Kleinböhl, A., Schofield, J. T., Kass, D. M., & McCleese, D. J. 2016, *LPICo*, **1980**, 4066
- Kleinböhl, A., Schofield, J. T., Kass, D. M., et al. 2018, Mars Weather and Climate: An Orbital Constellation for Atmospheric Profiling and Surface Thermophysics, https://mepag.jpl.nasa.gov/meeting/2018-04/EPosters/15_Kleinbohl_mars_weather_climate_mepag_180419.pdf
- Kleinböhl, A., Schofield, J. T., Kass, D. M., et al. 2009, *JGRE*, **114**, E10006
- Kleinböhl, A., Spiga, A., Kass, D. M., et al. 2020, *JGRE*, **125**, e06115
- Klesh, A., & Krajewski, J. 2015, in 29th Annual AIAA/USU Conf. on Small Satellites, MarCO: CubeSats to Mars in 2016, SSC15, <https://digitalcommons.usu.edu/cgi/viewcontent.cgi?article=3180&context=smallsat>
- Kulowski, L., Wang, H., & Toigo, A. D. 2017, *AdSpR*, **59**, 715
- Kuramoto, K., Kawakatsu, Y., & Fujimoto, M. 2018, *EPSC*, **12**, 1036
- Laizerotti, L. J. 2013, *SpWea*, **11**, 133
- Larson, D., Lillis, R. J., Lee, C. O., et al. 2015, *SSRv*, **195**, 153
- Lee, C., Lawson, W. G., Richardson, M. I., et al. 2011, *JGRE*, **116**, E11011
- Lewis, S. R., & Barker, P. R. 2005, *AdSpR*, **36**, 2162
- Lillis, R. J., Curry, S., Curtis, D. W., et al. 2019, *AGUFM*, SM42B-09
- Lillis, R. J., Deighan, J., Fox, J. L., et al. 2017, *JGRA*, **122**, 3815
- Lillis, R. J., Mitchell, D. L., Steckiewicz, M., et al. 2018, *JGRA*, **123**, 4349
- Lillis, R. J., Mitchell, D. L., Montabone, L., et al. 2020, *LPSC*, **51**, 1733
- Lin, R. P., Curtis, D. W., Larson, D. E., et al. 2008, *SSRv*, **136**, 241
- Liu, G. P., England, S., Lillis, R. J., et al. 2017, *JGRA*, **122**, 1258
- Ma, Y. J., Fang, X., Nagy, A. F., Russell, C. T., & Toth, G. 2014, *JGRA*, **119**, 1272
- Maattanen, A., Fouchet, T., Forni, O., et al. 2009, *Icar*, **201**, 504
- Madeleine, J. B., Forget, F., Millour, E., Navarro, T., & Spiga, A. 2012, *GeoRL*, **39**
- Mahaffy, P. R., Benna, M., Elrod, M., et al. 2015, *GeoRL*, **42**, 8951
- Mahaffy, P. R., Benna, M., King, T., et al. 2014, *SSRv*, **195**, 49
- Malan, D., Wiid, K., Burger, H., & Visagie, L. 2017, in 31st Annual AIAA/USU Conf. on Small Satellites, The Development of “nSight-1”—Earth Observation Science in 2U, <https://digitalcommons.usu.edu/cgi/viewcontent.cgi?article=3675&context=smallsat>
- Malin, M. C., Caplinger, M. A., & Davis, S. D. 2001, *Sci*, **294**, 2146
- Malin, M. C., Calvin, W. M., Cantor, B. A., et al. 2008, *Icar*, **194**, 501
- Mayyasi, M., Bhattacharyya, D., Clarke, J., et al. 2018, *GeoRL*, **45**, 8844
- McCleese, D. J., Schofield, J. T., Taylor, F. W., et al. 2007, *JGRE*, **112**, E05S06
- McCleese, D. J., Heavens, N. G., Schofield, J. T., et al. 2010, *JGRE*, **115**, E12016
- McClintock, W., Schneider, N. M., Holsclaw, G. M., et al. 2015, *SSRv*, **195**, 75
- McFadden, J. P., Carlson, C. W., Larson, D., et al. 2008, *SSRv*, **141**, 277
- McFadden, J. P., Kortmann, O., Curtis, D., et al. 2015, *SSRv*, **195**, 199
- Mellon, M. T., Feldman, W. C., & Prettyman, T. H. 2004, *Icar*, **169**, 324
- Mellon, M. T., & Jakosky, B. M. 1993, *JGR*, **98**, 3345
- Mendillo, M., Pi, X. Q., Smith, S., et al. 2004, *RaSc*, **39**, RS2028
- Mhangara, P., Mapurisa, W., & Mudau, N. 2020, *Aerospace*, **7**, 19
- Mitchell, D. L., Mazelle, C., Sauvaud, J.-A., et al. 2016, *SSRv*, **200**, 265
- Montabone, L., Lewis, S. R., & Read, P. L. 2005, *AdSpR*, **36**, 2146
- Montabone, L., Spiga, A., Kass, D. M., et al. 2020, *JGRE*, **125**, e06111
- Montabone, L., Forget, F., Millour, E., et al. 2015, *Icar*, **251**, 65
- Moyers, M. F., Saganti, P. B., & Nelson, G. A. 2006, *RadM*, **41**, 1216
- Mulholland, D. P., Lewis, S. R., Read, P. L., Madeleine, J. B., & Forget, F. 2016, *Icar*, **264**, 465
- NASA 2018, NASA Strategic Plan (Washington, DC: NASA), https://www.nasa.gov/sites/default/files/atoms/files/nasa_2018_strategic_plan.pdf
- Navarro, T., Forget, F., Millour, E., et al. 2017, *E&SS*, **4**, 690
- Navarro, T., Madeleine, J. B., Forget, F., et al. 2014, *JGRE*, **119**, 1479
- Neary, L., Daerden, F., Aoki, S., et al. 2020, *GeoRL*, **47**, e84354
- Neumann, G. A., Smith, D. E., & Zuber, M. T. 2003, *JGRE*, **108**, 5023
- Newman, C. E., Lewis, S. R., Read, P. L., & Forget, F. 2002, *JGRE*, **107**, 5123
- Newman, C. E., & Richardson, M. I. 2015, *Icar*, **257**, 47
- Newman, C. E., Gómez-Elvira, J., Marin, M., et al. 2017, *Icar*, **291**, 203
- Paschmann, G., & Daly, P. W. 1998, Analysis Methods for Multi-Spacecraft Data (Bern: International Space Science Institute), http://www.issibern.ch/PDF-Files/analysis_methods_1_1a.pdf
- Petersen, E. I., Holt, J. W., & Levy, J. S. 2018, *GeoRL*, **45**, 11,595
- Phillips, R. J., Zuber, M. T., Smrekar, S. E., et al. 2008, *Sci*, **320**, 1182
- Picardi, G., Plaut, J. J., Biccari, D., et al. 2005, *Sci*, **310**, 925
- Piqueux, S., Buz, J., Edwards, C. S., et al. 2019, *GeoRL*, **46**, 14290
- Piqueux, S., Kleinböhl, A., Hayne, P. O., et al. 2015, *Icar*, **251**, 164
- Piqueux, S., Kleinböhl, A., Hayne, P. O., et al. 2016, *JGRE*, **121**, 1174
- Plaut, J. J., Picardi, G., Safaeinili, A., et al. 2007, *Sci*, **316**, 92
- Rafkin, S. C. R. 2012, *P&SS*, **60**, 147
- Rafkin, S. C. R., Maria, M. R. V. S., & Michaels, T. I. 2002, *Natur*, **419**, 697
- Rajinder, K. J., Brendan, M. Q., Hugh, C., Sanjar, A., & Regina, L. 2010, *JARS*, **4**, 049501
- Ramongassie, S., Valle, P., Arpesi, P. G., & Heliere, F. 2014, in 10th European Conference on Synthetic Aperture Radar (Berlin) 1, <https://ieeexplore.ieee.org/document/6857006>
- Read, P. L., Lewis, S. R., & Mulholland, D. P. 2015, *RPPH*, **78**, 125901
- Rennó, N. O., Bos, B. J., Catling, D., et al. 2009, *JGRE*, **114**, E00E03
- Ritter, B., Gérard, J. C., Hubert, B., Rodriguez, L., & Montmessin, F. 2018, *GeoRL*, **45**, 612
- Roeten, K. J., Bougher, S. W., Benna, M., et al. 2019, *JGRE*, **124**, 3283
- Roux, A., Le Contel, O., Coillot, C., et al. 2008, *SSRv*, **141**, 265
- Sánchez-Cano, B., Lester, M., Andrews, D. J., et al. 2019, *ExA*, in press (arXiv:1908.05497)
- Sánchez-Cano, B., Blély, P.-L., Lester, M., et al. 2019, *JGRA*, **124**, 4556
- Scheeres, D., McMahon, J., Bierhaus, E., et al. 2020, *BAAS*, **52**, 2020n4i401p04
- Seu, R., Phillips, R. J., Biccari, D., et al. 2007, *JGRE*, **112**, E05S05
- Shaposhnikov, D. S., Medvedev, A. S., Rodin, A. V., & Hartogh, P. 2019, *GeoRL*, **46**, 4161
- SMD, N. 2018
- Solomon, S. C., & Head, J. W. 1990, *JGR*, **95**, 11073
- Spiga, A., Faure, J., Madeleine, J. B., Maattanen, A., & Forget, F. 2013, *JGRE*, **118**, 746
- Spiga, A., Hinson, D. P., Madeleine, J.-B., et al. 2017, *NatGe*, **10**, 652
- Steele, L. J., Lewis, S. R., Patel, M. R., et al. 2014, *Icar*, **237**, 97
- Steenburgh, R. A., Biesecker, D. A., & Millward, G. H. 2014, *SoPh*, **289**, 675
- Stern, S. A., Slater, D. C., Scherrer, J., et al. 2007, *SSRv*, **128**, 507
- Stiepen, A., Jain, S. K., Schneider, N. M., et al. 2017, *JGRA*, **122**, 5782
- Stillman, D. E., & Grimm, R. E. 2011, *JGRE*, **116**, E03001

- Strausberg, M. J., Wang, H., Richardson, M. I., Ewald, S. P., & Toigo, A. D. 2005, *JGRE*, **110**, E02006
- Stuurman, C. M., Osinski, G. R., Holt, J. W., et al. 2016, *GeoRL*, **43**, 9484
- Tellmann, S., Pätzold, M., Häusler, B., Hinson, D. P., & Tyler, G. L. 2013, *JGRE*, **118**, 306
- Thieman, E. M. B., Chamberlin, P. C., Eparvier, F. G., et al. 2017, *JGRA*, **122**, 2748
- Toigo, A. D., Smith, M. D., Seelos, F. P., & Murchie, S. L. 2013, *JGRE*, **118**, 89
- Toigo, A. D., Waugh, D. W., & Guzewich, S. D. 2017, *GeoRL*, **44**, 71
- Vandaele, A. C., Korabiev, O., Daerden, F., et al. 2019, *Natur*, **568**, 521
- Vertesi, J. 2020, *Shaping Science: Organizations, Decisions, and Culture on NASA's Teams* (Chicago, IL: Univ. Chicago Press)
- Vogt, M. F., Withers, P., Fallows, K., et al. 2017, *JGRA*, **122**, 891
- Wang, C., Forget, F., Bertrand, T., et al. 2018, *JGRE*, **123**, 982
- Wang, H., & Fisher, J. A. 2009, *Icar*, **204**, 103
- Watzin, J., & Haltigin, T. 2020, Mars Exploration Program Analysis Group, Mars Exploration Ice Mapper, (Virtual) MEPAG Spring Meeting, https://mepag.jpl.nasa.gov/meeting/2020-04/Day1/16_WATZIN-HALTIGIN-Ice%20Mapper_MEPAG_%20April%20152020_Final%20v2_post.pdf
- Weiss, D. K., & Head, J. W. 2017, *Icar*, **288**, 120
- Wilson, R. J., & Guzewich, S. D. 2014, *GeoRL*, **41**, 3375
- Wilson, R. J., Haberle, R., Noble, J., et al. 2008a, *LPICo*, **1447**, 9023
- Wilson, R. J., Lewis, S. R., Montabone, L., & Smith, M. D. 2008b, *GeoRL*, **35**, L07202
- Wilson, R. J., Neumann, G. A., & Smith, M. D. 2007, *GeoRL*, **34**, L15404
- Wu, Z., Li, T., Zhang, X., Li, J., & Cui, J. 2020, *Nat Commun*, **11**, 614
- Xu, S. S., Mitchell, D. L., McFadden, J. P., et al. 2018, *GeoRL*, **45**, 10119
- Yigit, E., England, S. L., Liu, G., et al. 2015, *GeoRL*, **42**, 8993
- Young, S. A., Vaughan, M. A., Garnier, A., et al. 2018, *ATM*, **11**, 5701
- Zeitlin, C., Cleghorn, T., Cucinotta, F., et al. 2004, *AdSpR*, **33**, 2204
- Zhao, Y., Greybush, S. J., Wilson, R. J., Hoffman, R. N., & Kalnay, E. 2015, *TellA*, **67**, 26042
- Zou, Y., Zhu, Y., Bai, Y., et al. 2021, *AdSpR*, **67**, 812